KU LEUVEN

ARENBERG DOCTORAL SCHOOL
Faculty of Engineering Science

Learning from structured EEG and fMRI data supporting the diagnosis of epilepsy

Borbála Hunyadi

Dissertation presented in partial fulfillment of the requirements for the degree of Doctor in Engineering

June 2014

Learning from structured EEG and fMRI data supporting the diagnosis of epilepsy

Borbála HUNYADI

Examination committee:
Prof. dr. ir. Y. Willems, chair
Prof. dr. ir. S. Van Huffel, supervisor
Prof. dr. W. Van Paesschen, co-supervisor
Prof. dr. ir. M. De Vos, co-supervisor
Prof. dr. ir. L. De Lathauwer
Prof. dr. P. Dupont
Prof. dr. ir. D. Vandermeulen
Prof. dr. ir. E. Acar
(University of Copenhagen)
Prof. dr. ir. S. Vandenberghe
(Ghent University)

Dissertation presented in partial fulfillment of the requirements for the degree of Doctor in Engineering

June 2014

Uitgegeven in eigen beheer, Borbála Hunyadi, Kasteelpark Arenberg 10 box 2446, B-3001 Heverlee (Belgium)

ISBN 978-94-6018-842-8

D/2014/7515/66

Acknowledgements

We must find time to stop and thank the people who make a difference in our lives.

– John F. Kennedy

First of all, I would like to thank my supervisor, prof. Sabine Van Huffel. Sabine, thank you for giving me the possibility to work in your group, for your trust and support during these years. The positive and safe environment you created for me and for all of us in Biomed is invaluable. You built not just a research group but a friendly community, I am really grateful for that!

Many thanks to Prof. Maarten De Vos. Maarten, you guided me so closely, first as a fellow PhD student and then postdoc, that you deserved to become my co-supervisor. Your constructive comments never failed to reach me even if you were already far away, being a professor in Oldenburg. Thanks for all the time you invested in me and I wish you all the best for your career!

I would like to express my gratitude for my co-supervisor Prof. Wim Van Paesschen. Wim, thank you for the frequent meetings, discussions, for teaching me so much about the clinical aspects of epilepsy research. It was a factor which gave the most important motivation for my work! Here I also would like to thank Prof. Patrick Dupont, who also participated in our Tuesday meetings. Patrick, your attention to details, your critical thinking served as an excellent example for me!

I really appreciate the guidance of Prof. Lieven De Lathauwer. Lieven, thank you for your guiding me through the challenging world of tensors! The journey has not ended yet, but I am confident that I can always reach you for advice on how to take the next step.

I would also like to thank the chairman and the members of my examination committee, Prof. Yves Willems, Prof. Evrim Acar, and Prof. Stefaan

Vandenberghe, Prof. Dirk Vandermeulen for their feedback on my thesis and the discussion during the preliminary defence.

There are many people who were not part of my PhD committee, but contributed a lot to my work. I would like to thank Prof. Johan Suykens for our collaboration on my first paper and his very prompt availability any time I had questions. In the same context, many thanks also to Marco Signoretto. Marco, I hope we will keep on working together in the future as well!

Many thanks for all the past and present members of the Biomed group for all the nice activities we had together! Thanks to Katrien, who was the very first mentor within Biomed during my Erasmus period, who later became my officemate and a true friend! Thanks to Bogdan, who I haven't seen much, but he was a really fun company when he was there and helped me a lot with starting off the fMRI work. After Katrien and Bogdan left, Rob, and later Wout came to fill the office with young and crazy energy, thank you, guys! Thanks to Alex for the culinary experiences (the war is not over, though!), for Caro and her Steven for all the games we played, for both of them as well as to Anca and Steven for the brainstorming about how to broaden our horizons further than the academic world! Thanks to Ninah and Hans for the Kinderuniversiteit workshop; and for Hans, Piet and Jeroen for the T-Eye project, which followed. Thanks to Devy, Kirsten and Ninah for helping out during the demo's! And thanks indeed to all of you, Vladimir, Yipeng, Ivan, Joachim, Amir, Wouter, Wang, Diana, Maria, Mariya, Rosy, Aileen, Kris, Ann-Sofie, Dzemila, Adrian, Nicolas, Tim, Milica, Laure, Griet, Thomas, Vanya, Jan and Ben! And thanks also to the Biotensors people, Nico, Otto, Laurent, Paul, Mikael, Ignat, Bharath, I am looking forward to working together! I need to thank as well Ida, Mimi, John, Wim, Maarten and Liesbeth, the system group and CDE for taking all the administration, financial and IT burdens from my shoulders!

Many thanks to my colleagues from the Gasthuisberg as well, Laura Seynaeve and Simon Tousseyn for the nice atmosphere. Thanks, Simon, for sharing your knowledge and data with me, and for the nice company during the AES meetings! And thanks for Guido Van Driel for his welcoming and friendly attitude every time we met!

Thanks to all my friends who helped me relax, forget about work and kept me sane during these years! Thanks to Misi, who is my oldest friend here in Leuven, who never hesitated to give a helping hand and who represents continuity between my life in Budapest and here in Leuven! Thanks to Lucie and Drita for the Saturday coffees and the spa experiences in Sportoase! Thanks for Teresa and Riccardo for their friendship which did not fade even after they left Leuven. Thanks for Ksenia and Kees for all the fun weekends we spent together! Thanks

to Katleen, Johanna, Dominique and Johan for the Quindi! And many thanks of course to my old friends, Flóra and Ági. Nagyon hiányoztok, sajnálom, hogy nem tudunk gyakrabban találkozni, de nagyon boldoggá tesz, hogy mégis minden alkalommal ugyanott tudjuk folytatni a beszélgetest, ahol hónapokkal korábban abbahagytuk!

Although I left them for the end, the love of Adi and my family was the most important support for me during this period. Adi, thank you for your eternal patience, strength and optimism and for the tremendous help during the last difficult weeks! And most of all, thank you for the warm home we built together here in Leuven! And I thank my family for the memory of the warm home... Köszönöm az egész családnak a lelkesedést, amivel a meghívásomat fogadtátok! Nagyon sokat jelentett! És köszönöm a sok szeretetet és támogatást a szűk családomnak, nektek, Mama, Papa és Kriszti! A kezdetektől fogva azon voltatok, hogy a legjobbat hozzátok ki belőlem. Az, hogy ma ezeket a sorokat írom, elsősorban a ti érdemetek!

> *Piglet noticed that even though he had a Very Small Heart, it could hold a rather large amount of Gratitude.*
>
> – A.A. Milne, *Winnie-the-Pooh*

Abstract

Epilepsy is a neurological condition that manifests in epileptic seizures as a result of an abnormal, synchronous activity of a large group of neurons. Depending on the affected brain regions, seizures produce various severe clinical symptoms. Epilepsy cannot be cured and in many cases is not controlled by medication either. Surgical resection of the region responsible for generating the epileptic seizures might offer remedy for these patients.

Electroencephalography (EEG) and functional magnetic resonance imaging (fMRI) measure the changes of brain activity in time over different locations of the brain. As such, they provide valuable information on the nature, the timing and the spatial origin of the epileptic activity. Unfortunately, both techniques record activity of different brain and artefact sources as well. Hence, EEG and fMRI signals are characterised by low signal to noise ratio. Data quality and the vast amount of recordings make the visual interpretation of these signals impractical.

Therefore, this thesis aims at developing automated analysis techniques which can support the accurate diagnosis of the epilepsy syndrome. The fundamental principle behind the proposed approaches is to exploit the characteristic spatiotemporal structure underlying epileptic brain signals. With this mindset, we identify problems and offer solutions for three crucial aspects of presurgical evaluation.

First, an automated seizure detection algorithm is developed. While traditional detectors analyse each EEG channel separately, our solution incorporates spatial information from the multichannel EEG data. To this end, we apply a regularisation scheme using nuclear norm, a penalty term inducing low-rank structure. It is shown that the proposed approach improves detection performance compared to traditional solutions, even if less seizure information is available for training.

Once a seizure occurrence is identified, the next step in the diagnostic procedure

is to determine the seizure onset zone (SOZ) based on the EEG. Blind source separation (BSS) techniques can help visual interpretation by removing artefacts contaminating the seizure pattern, or can extract the clean seizure source itself. As each method uses different model assumptions, their use is appropriate in certain situations and are limited in others. In this thesis a novel tensor based technique, namely Block Term Decomposition (BTD) is applied to extract sources from the EEG data. Depending on the chosen tensor representation, this formulation allows to model seizures as a sum of exponentially damped sinusoids or as oscillatory phenomena which evolve in frequency or spread to remote brain regions over time.

Although seizure activity patterns provide important localising information, due to the rare occurrence of seizures this is a time consuming procedure. Alternatively, localising the epileptic network based on interictal fMRI recordings can offer a surrogate. EEG-correlated fMRI analysis has already proven useful for this purpose, however, a purely fMRI based approach would be invaluable in case no reliable EEG information is available. To this end, independent component analysis (ICA) is applied to extract spatially independent components from the fMRI time series. It is demonstrated that ICA can extract epileptic sources which substantially overlap with the SOZ. Finally, a method is developed which selects the epileptic source blinded to all other clinical information. As a result, the spatial map corresponding to the selected epileptic component can localise the SOZ.

Presurgical evaluation relies on multidisciplinary consensus. A surgery is planned in case concordant data are obtained from all clinical examinations and imaging modalities. The techniques proposed in this thesis can contribute to the current procedure by extending the applicability of existing techniques and providing precise information in a time effective way.

Samenvatting

Epilepsie is een neurologische aandoening die gekarakteriseerd wordt door de aanwezigheid van epileptische aanvallen als gevolg van abnormale, synchrone activiteit van een grote groep neuronen. Afhankelijk van welke hersengebieden aangetast zijn, geven aanvallen verschillende klinische ziektebeelden. Epilepsie kan niet genezen worden en in vele gevallen ook niet gecontroleerd met medicatie. Voor deze groep patiënten kan het operatief verwijderen van de epileptogene zone, het gebied verantwoordelijk voor het genereren van epileptische aanvallen, een oplossing bieden.

Elektro-encefalografie (EEG) en functionele magnetische resonantie beeldvorming (fMRI) meten veranderingen in hersenactiviteit over de tijd op van verschillende gebieden in de hersenen. Daarmee kunnen ze belangrijke informatie leveren over de oorzaak, de timing en de spatiale bron van de epileptische activiteit. Beide technieken meten echter een combinatie van hersenactiviteit en ruisbronnen. EEG en fMRI signalen worden dus gekenmerkt door een lage signaal-tot-ruis verhouding. Data kwaliteit en de grote hoeveelheid data maken visuele interpretatie van deze signalen onpraktisch.

Daarom is het doel van deze thesis automatische analyse technieken te ontwikkelen die de diagnose van epilepsie kunnen ondersteunen. Het fundamentele principe achter de voorgestelde technieken is om de spatiotemporele structuur die in de signalen aanwezig is, te benutten. Dit in gedachten houdend, identificeren we problemen en bieden we oplossingen aan voor drie belangrijke aspecten van de pre-chirurgische evaluatie.

Eerst is een automatische aanvalsdetector ontwikkeld. Terwijl traditionele detectoren verschillende EEG kanalen afzonderlijk analyseren, gebruikt onze oplossing spatiale informatie aanwezig in het meerkanaals EEG. Daarvoor passen we een regularisatie schema gebaseerd op de nucleaire norm toe, die lage-rank structuren oplegt. We tonen aan dat de voorgestelde methode aanvalsdetectie verbeterd ten opzichte van traditionele methoden, zelfs wanneer

zeer weinig aanvalsinformatie beschikbaar is om de methode te trainen.

Eenmaal een aanval gedetecteerd is, is de volgende stap in het diagnostische probleem om de epileptogene zone op basis van het EEG te bepalen. Blinde bron scheidingstechnieken (BSS) kunnen visuele interpretatie helpen door artefacten te scheiden van de aanvalspatronen, of kunnen zuivere epileptische activiteit schatten. Vermits zulke blinde methoden op verschillende assumpties berusten, is hun gebruik geschikt in bepaalde situaties en gelimiteerd in andere. In deze thesis hebben we een nieuwe methode, de blok term ontbinding (BTD) toegepast die rang (L,L,1) componenten uit het EEG haalt. Afhankelijk van de gekozen tensor voorstelling, laat de formulering toe om aanvallen te modeleren als een som van exponentieel gedempte sinussen of als oscillerende fenomenen die variëren in frequentie of zich uitspreiden over verschillende gebieden in de tijd.

Hoewel de patronen van aanvalsactiviteit belangrijke informatie verschaffen, blijft het een tijdsintensieve procedure. Een alternatief kan zijn om het epileptische netwerk te lokaliseren op basis van interictale fMRI metingen. Voor dit doel is onafhankelijke bron ontbinding (ICA) toegepast om spatieel onafhankelijke bronnen uit de fMRI tijdsserie te halen. Het is aangetoond dat ICA epileptische componenten kan schatten die substantieel overlappen met de epileptogene zone. Tot slot is ook een methode ontwikkeld die de epileptische component bepaald zonder toevoeging van andere klinische informatie. Het resultaat van de methode is dat de epileptogene zone kan bepaald worden aan de hand van deze component.

Pre-chirurgische evaluatie bouwt op multidisciplinaire consensus. De operatie wordt gepland op basis van alle klinische onderzoekingen en multimodale beeldvorming. De technieken ontwikkeld in deze thesis kunnen bijdragen tot de huidige procedure door nauwkeurige informatie op een efficiënte manier te leveren.

Nomenclature

Symbols

$a, b, \ldots$	scalars
$\mathbf{a}, \mathbf{b}, \ldots$	vectors
$\mathbf{A}, \mathbf{B}, \ldots$	matrices
$\mathcal{A}, \mathcal{B}, \ldots$	tensors
a_{ijk}, $(\mathcal{A})_{ijk}$	element of three-way tensor $\mathcal{A}$ at position (i, j, k)
$\begin{bmatrix} a & b \\ c & d \end{bmatrix}$	matrix with entries a, b, c and d
$\begin{bmatrix} \mathbf{a} & \mathbf{b} \end{bmatrix}$	matrix with columns $\mathbf{a}$ and $\mathbf{b}$
$\mathbf{I}$	identity matrix

Basic operations

$\sum$	sum
$\|\mathbf{A}\|$	Frobenius norm of a matrix $\mathbf{A}$
$\mathbf{A}^T$	transpose of a matrix $\mathbf{A}$
$\mathbf{A}^{-1}$	inverse of a matrix $\mathbf{A}$
$\operatorname{rank}(\cdot)$	rank
$\operatorname{rank}_n(\mathcal{A})$	mode-n rank of a tensor $\mathcal{A}$
$\langle \cdot, \cdot \rangle$	inner/scalar product
$\circ$	outer product
$\otimes$	Kronecker product
$\odot$	Khatri-Rao product
$\mathcal{A} \times_n \mathbf{U}$	mode-n product of a tensor $\mathcal{A}$ and a matrix $\mathbf{U}$
$\mathbf{A}_{(n)}$	mode-n unfolding or matricisation of a tensor $\mathcal{A}$

Metrics

Hz	Hertz
ms	milliseconds
mV	millivolt
μV	microvolt
s	seconds

Abbreviations

BCG	BallistoCardioGram
BCI	Brain Computer Interface
BOLD	Blood Oxygen Level Dependent
BSS	Blind Source Separation
BTD	Block Term Decomposition
CCA	Canonical Correlation Analysis
CNS	Central Nervous System
CPD	Canonical Polyadic Decomposition
CSF	CerebroSpinal Fluid
CWT	Continuous Wavelet Transform
ECG	ElectroCardioGram
EEG	ElectroEncephaloGram
EMG	ElectroMyoGram
EMU	Epilepsy Monitoring Unit
ERP	Event-Related Potential
EOG	ElectroOculoGram
fMRI	Functional Magnetic Resonance Imaging
GLM	General Linear Model
HRF	Hemodynamic Response Function
ICA	Independent Component Analysis
IED	Interictal Epileptiform Discharge
JADE	Joint Approximate Diagonalization of Eigenmatrices
LDA	Linear Discrimimant Analysis
LS-SVM	Least Squares Support Vector Machine
MEG	Magnetoencephalogram
MNI	Montreal Neurological Institute
MR	Magnetic Resonance
MRI	Magnetic Resonance Imaging
NNL	Nuclear Norm Learning
PCA	Principal Component Analysis
PET	Positron Emission Tomography
PSD	Power Spectral Density
PSP	PostSynaptic Potential
SISCOM	Subtraction Ictal SPECT co-registered to MRI

SNR	Signal to Noise Ratio
SOBI	Second Order Blind Identification
SOZ	Seizure Onset Zone
SPECT	Single Photon Emission Computerised Tomography
SPM	Statistical Parametric Mapping
SVD	Singular Value Decomposition
SVM	Support Vector Machine
TMS	Transcranial Magnetic Stimulation
TR	Repetition Time

Contents

List of Figures

List of Tables

Chapter 1

Introduction

1.1 Problem statement

Intel co-founder Gordon E. Moore predicted in 1965 that the number of transistors on a unit surface semiconductor would double every two years [147]. Indeed, computing power and storage capacity have seen an exponential improvement ever since. This rate of technological advancement has its implications in many aspects of life and in any scientific field, in healthcare and biomedical technology as well. Nowadays it is possible to record, store, retrieve and efficiently process large amounts of medical data.

Besides opportunity, there appeared also need. The ageing society contributes importantly to the increasing demand and expenses of medical care. It has been demonstrated that health information technology can play a crucial role in improving the quality, efficiency and cost-effectiveness of healthcare [230]. Although Moore's law does not apply directly, we can expect an accelerating progress in the utility of biomedical technology in healthcare[228], including automated analysis techniques and decision support systems.

This thesis investigates the utility of advanced signal processing and machine learning techniques in a particular field of medicine, namely in epilepsy monitoring and presurgical evaluation. This is a truly multidisciplinary field, where the epileptologist, neurologist, radiologist, psychiatrist and the surgeon have to collaborate, share and integrate information from several different diagnostic techniques and imaging modalities. We focus on two of these techniques: electroencephalography (EEG) and functional magnetic resonance imaging (fMRI). These techniques involve lengthy measurement sessions and

require specially trained personnel for recording and above all interpreting the overwhelming amount of data. Therefore, automated methods supporting the interpretation would be highly beneficial.

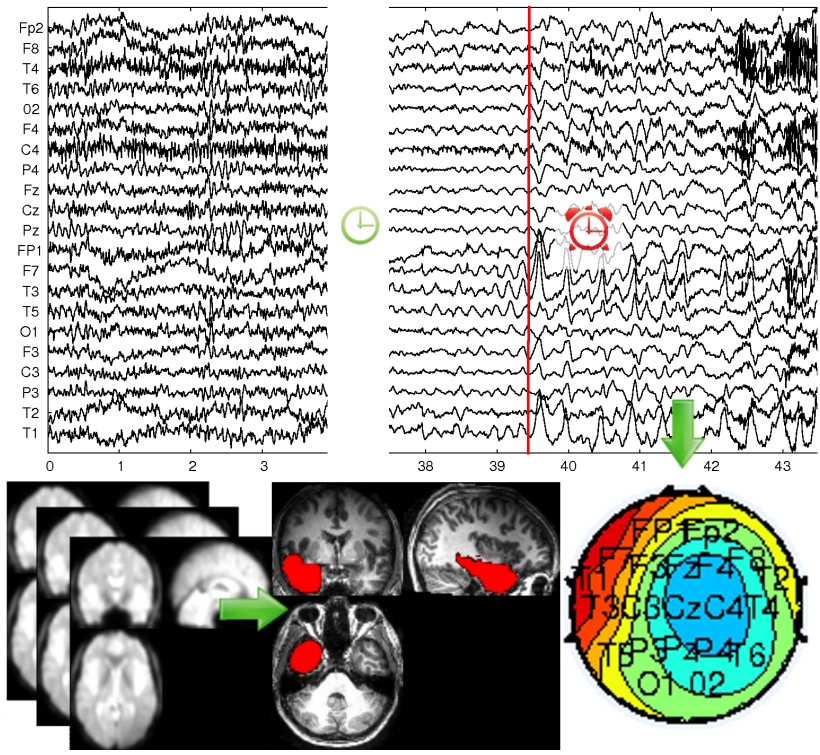

Figure 1.1: EEG and fMRI recordings involve lengthy measurement sessions and require specially trained personnel for recording and above all interpreting the overwhelming amount of data. Therefore, the goal of the thesis is to develop automated methods supporting current procedures.

Both EEG and fMRI measure ongoing neural activity during a certain period of time at specific locations at the surface of or inside the brain. As such, they record a multivariate time series representation of the brain activity, where both the temporal and spatial relationships among the individual time series carry crucial information. The key concept behind the methodologies presented in this thesis is to exploit this inherent structural information on different levels.

On one hand, structural information can be exploited on the level of data representation. One can extract features which explicitly quantify the temporal

or spatial structure of the signals. These features then can be used to distinguish between normal or pathological data. On the other hand, structural information can be utilized implicitly on an algorithmic level, as done in unsupervised learning techniques, including blind source separation. As a result, the multichannel data is decomposed to its underlying source signals, revealing or enhancing interesting patterns which were hidden in the noisy measurements. Furthermore, we will see that a-priori information on the data structure can be incorporated into a supervised learning algorithm as well. In turn, the machine can learn a robust distinction between normal and pathological data by combining previous observations with the provided a-priori information.

The specific applications within the field of presurgical evaluation and detailed motivation for the chosen methodology are given in a chapter-by-chapter basis below. The outline of the thesis is depicted in Figure 1.2

1.2 Chapter-by-chapter overview

Chapter 2 presents the medical aspects of this thesis. It introduces some essential background knowledge on brain anatomy and function. Further, some brain monitoring and imaging techniques are treated, with special attention to EEG and fMRI recordings. Finally, the neurological disorder epilepsy is discussed. We explain how the diagnosis and treatment of epilepsy benefits from neuroimaging and in which ways technology could improve the current clinical practice. The objective of the thesis is to pursue these improvements.

Chapter 3 presents the methodological aspects of this thesis. We introduce the various machine learning methods applied in the following chapters. On one hand, unsupervised learning techniques - blind source separation techniques in particular - are crucial in biomedical signal processing. As neural signals are an inherent mixture of several underlying activity patterns and noise, such techniques are useful to decompose the data into their constituent sources including the activity of interest. On the other hand, supervised learning techniques are capable of learning specific patterns in the data based on a set of examples, and automatically draw conclusions about new observations. These techniques are useful in automated event detection during monitoring or in decision support systems.

Chapter 4 introduces two novel EEG-based seizure detection techniques. The first seizure detector aims at mimicking the visual interpretation process of the human expert viewer. We reformulate the visually appearing characteristics as mathematical measures and use a simple rule-based system to make inference

about the EEG segment under study. These decision rules are universally applicable to all focal epilepsy patients. In contrast, the second detector is a patient-specific system. For the purpose of this method we use features which are well-established in the literature. The novelty of this second approach lies within the applied learning algorithm — a regularisation scheme using nuclear norm penalty — which can exploit spatial information from the multichannel EEG, which is characteristic to the seizures of a focal epilepsy patient.

Chapter 5 investigates the applicability of a new blind source separation technique, namely block term decomposition (BTD) for modelling seizure patterns in EEG. Several blind source separation techniques, including canonical polyadic decomposition (CPD) have been successfully used to extract clean seizure activity, separating it from artefacts and neural activity of different origin. Moreover, these techniques can also infer to the localisation of the seizure based on the topographical map corresponding to the ictal source. BTD generalises CPD in the sense that it extracts sources of low multilinear rank as opposed to rank−1 tensors in CPD. Therefore, we hypothesise that it will allow to model complex, nonstationary sources, such as ictal patterns which evolve in morphology or topography.

Chapter 6 further elaborates on the localisation of epileptic activity. Although inspection of the ictal EEG pattern provides valuable information on the seizure onset zone, as seizures occur rarely, obtaining such information may take several days in practice. Alternatively, a lot of research have investigated the possibility of using interictal fMRI recordings for localising epileptic activity. A widely used approach consists in simultaneously recording EEG and fMRI, and identifying brain regions where the fMRI signals covary with the timing of epileptic events observed in the EEG. However, we will see that for various reasons EEG often does not provide useful information to this end. Therefore, we develop a technique which can localise the epileptic brain regions based purely on the fMRI. In a first step we decompose the fMRI data using independent component analysis (ICA). We show that epileptic sources are found even in patients where no interictal spikes were seen in the EEG. Subsequently, we characterise the epileptic independent components and based on this knowledge we train a support vector machine (SVM) which can automatically select the epileptic component in successive patients. Finally, the epileptic brain regions are localised based on the spatial map corresponding to the epileptic component.

Chapter 7 summarises the findings of the thesis and suggests directions for future research.

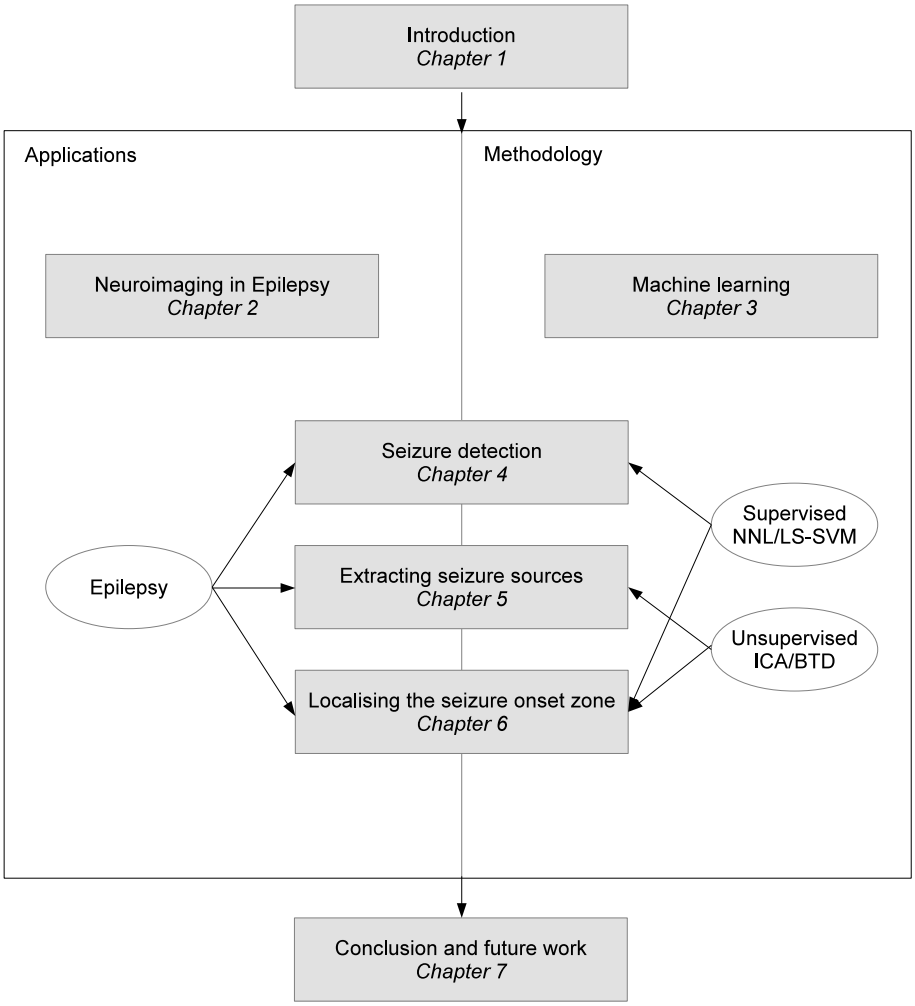

Figure 1.2: Outline of the thesis. Abbreviations used in figure: Independent component analysis (ICA), Block term decomposition (BTD), Nuclear norm learning (NNL), Least squares support vector machines (LS-SVM).

1.3 Collaborations

My PhD research was conducted within the Biomed group, STADIUS, Department on Electrical Engineering (ESAT), KU Leuven, under the supervision of Prof. Sabine Van Huffel. My work has also been closely supervised by Prof. Maarten De Vos; first as a postdoctoral researcher within Biomed and later as my co-supervisor and professor at the University of Oldenburg.

The work presented in this thesis was carried out in close collaboration with the Laboratory for Epilepsy Research, UZ Leuven, headed by Prof. Wim Van Paesschen. Long-term EEG has been recorded in the Epilepsy Monitoring Unit. The assistance of Guido Van Driel in collecting the EEG dataset and his explanation on how to interpret various EEG patterns was very valuable. Interictal EEG-fMRI data was collected within the context of the IWT TBM 080658-MRI (EEG-fMRI) project. The data acquisition procedure was optimised and the actual data were recorded by Simon Tousseyn. Prof. Wim Van Paesschen and Simon Tousseyn offered essential insight into the medical aspects of this thesis. Together with Prof. Patrick Dupont they gave me invaluable feedback on the study design, the methodology and the interpretation of the results.

Furthermore, recent contributions from my departmental colleagues Prof. Johan Suykens and Marco Signoretto on multilinear spectral regularisation have inspired important methodological choices in this thesis. I acknowledge their helpful contribution in the development of the nuclear norm regularisation approach for seizure detection, presented in Chapter 4 .

Finally, the application of block term decomposition for extracting epileptic sources from EEG data, presented in chapter 5, was a joint work with Prof. Lieven De Lathauwer from the Group Science, Engineering and Technology of Kulak. The presented study originated from the successful master thesis project of Daan Camps which I supervised together with Laurent Sorber.

Chapter 2

Neuroimaging in epilepsy

Neuroimaging techniques, in general, aim at gaining insight into the anatomy and the function of the brain. Detecting abnormalities either on anatomical or functional level can lead to the diagnosis of various neurological diseases, such as epilepsy. The current chapter aims at giving an overview about the main principles behind brain imaging and monitoring techniques applied in epilepsy research and diagnosis. In particular, section 2.1 describes the anatomy and the functioning of the brain. Subsequently, section 2.2 presents various imaging and monitoring techniques, with special attention to EEG and fMRI, which are of particular interest in this thesis. Further, section 2.3 describes the neurological disorder epilepsy in detail. This thesis focuses on severe cases, where the treatment of this disorder requires surgery. Hence, the process of presurgical evaluation is introduced in the final section 2.4.

2.1 The human brain

Based on [20, 226, 69, 157] an overview about the structure and the function of the human brain is given.

2.1.1 Anatomy of the brain

The brain is part of the central nervous system (CNS) and is responsible for selecting, sorting and interpreting the information received from the body and

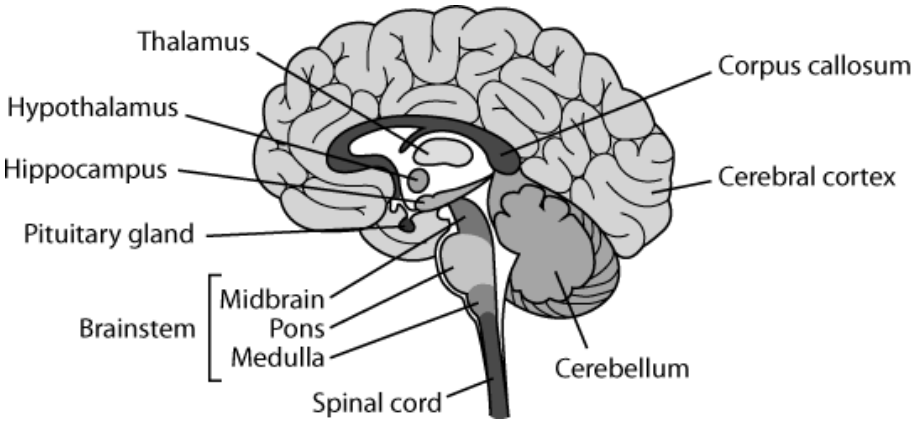

Figure 2.1: Schematic representation of a sagittal section of the brain, allowing to visualise the major anatomical structures. From [95].

the environment in order to control behaviour according to its interpretation of reality.

Figure 2.1 and 2.2 depicts a schematic representation of a sagittal and an axial section of the brain, respectively. The brain, the spinal cord and the optic nerve together with the retina (not shown) constitute the CNS. The brain is covered by three layers of tissue membranes, the meninges. Cerebral spinal fluid (CSF), providing support and protection, occupies its surroundings as well as the ventricular cavities. The brain consists of the cerebellum, the brainstem (midbrain, pons, and medulla) and the cerebrum. The latter includes the two hemispheres and the diencephalon. The two hemispheres are connected by the corpus callosum. The cerebral cortex, the 2-3 cm thick outer layer of the brain, is subdivided into the frontal, parietal, occipital and temporal lobes (Figure 2.3) in both hemispheres. The diencephalon is comprised of the thalamus, the hypothalamus, the epithalamus and the subthalamus. The thalamus has a central role in the brain as it connects the sensory systems with the cortex.

The nervous system is built up of more than 10^{10} nerve cells or neurons (see Figure 2.4). They are composed of a cell body called soma, short dendrites and a single long axon. The dendrites extend the receiving surface of the neuron and form synapses with axons of other neurons, which provide them input in the form of electrical impulses. Many axons are covered by a myelin sheath to increase the speed of the impulse propagation. The nervous tissue contains two visually distinguishable areas, namely the grey matter and the white matter. The distinction in colour is due to the fact that the grey somas and dendrites are accumulated in the outermost surface and in some deep structures of the brain,

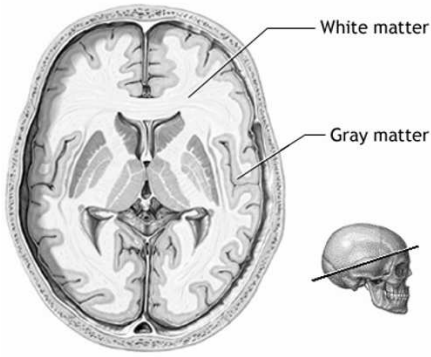

Figure 2.2: Axial section of the brain, allowing to visualise both hemispheres, the ventricles, as well as the grey and white matter. Adapted from [96].

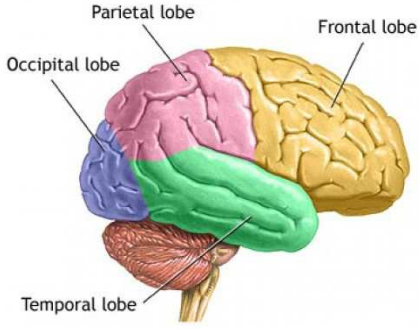

Figure 2.3: Schematic representation of the brain indicating the four lobes. From [97].

while the interconnections between them, the axons covered by the whitish myelin, reside in the areas within.

2.1.2 Physiology of the brain

Although it is rather well known how the individual neurons work, their complex interconnections and interactions, i.e. the functioning of brain networks is less clear. In this section we attempt to give an overview about the current understanding of the brain function, both on a microscopic and

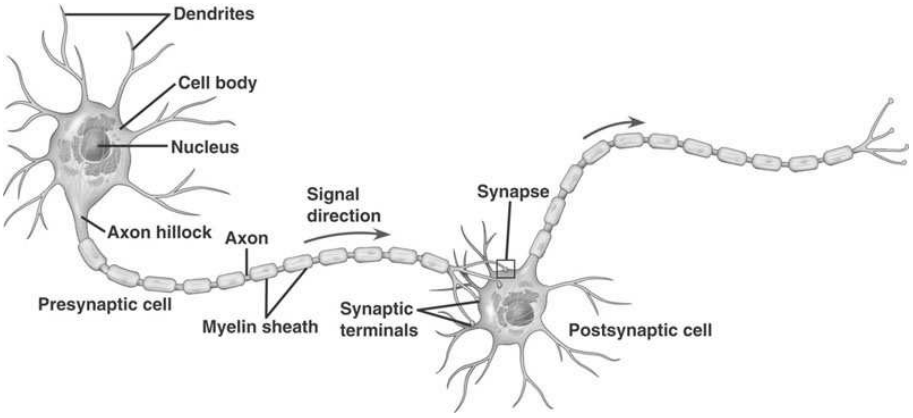

Figure 2.4: Schematic representation of a neuron. From [98].

macroscopic level. Note that we do not aim for an exhaustive review but we discuss the aspects most relevant for this thesis.

Neuronal communication

The neurons communicate with each other through electrochemical currents. They have a resting membrane potential of −60 – −70 mV compared to extracellular space, due to the unequal distribution of anions and cations. This membrane potential is subject to various fluctuations, which are driven by synaptic activity. If an action potential is fired in a presynaptic cell, it travels along the axon and neurotransmitters are released at the axon terminal. The neurotransmitters are received by their corresponding receptors, which in turn open certain ion channels. In case of an excitatory postsynaptic potential (EPSP) a net inflow of cations occurs across the postsynaptic membrane, causing the depolarisation of the postsynaptic neuron. In contrast, with the generation of an inhibitory postsynaptic potential (IPSP) there is a net outflow of cations from the postsynaptic neuron, causing a hyperpolarisation of the postsynaptic membrane. If two or more action potentials travel to the same synapse within a short interval, the postsynaptic potentials sum up. In case the integrated EPSP and hence the depolarisation reaches a certain threshold, an action potential is fired at the postsynaptic cell.

Neural networks

In the cerebral cortex 90% of neurons are either pyramidal cells forming exclusively excitatory synapses, or inter-neurons forming exclusively inhibitory synapses with other cells. Each cell receives and transmits information to thousands of other neurons. A compartment within which all neurons are interconnected with each other but relatively few connections project outside of it is called a cortical column. Connections between cortical columns are called cortico-cortical projections. To a lesser extent connections are also made to subcortical networks, most importantly to the thalamus. These are called thalamo-cortical projections.

This type of structure facilitates a highly efficient information processing mechanism. The relatively autonomous nature of cortical columns allows parallel and therefore fast execution. Furthermore, the role of the thalamus is to synchronise the activity of multiple cortical columns so that they can work together or independently on a certain task. For the controlled activity of these neural networks a close balance between excitation and inhibition is essential.

Metabolism and hemodynamics

Neurons require oxygen and glucose for their proper function. As they do not have internal reserves, blood circulation has to supply them these nutrients in case of demand. Increased neural activity requires more oxygen and glucose to be delivered. Interestingly, oxygen consumption and supply is mismatched: the cerebral blood flow overcompensates for the increase in demand resulting in an excess of oxygenated blood in active brain areas [136].

2.2 Brain imaging and monitoring techniques

Various measurement techniques exist which capture different aspects of brain structure and function. Anatomical structures, lesions can be observed using MRI or CT; metabolic and functional activity of the brain is captured by PET, SPECT or fMRI, while EEG and MEG records the electromagnetic field generated by the brain. Figure 2.5 compares several of these techniques based on their temporal and spatial resolution. In the following sections a detailed description of EEG and fMRI is given.

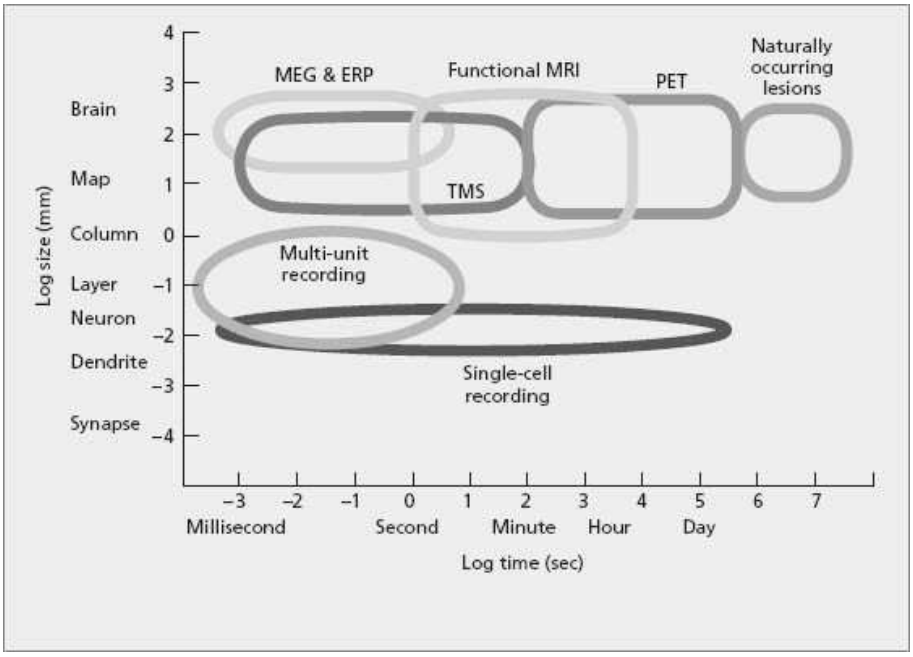

Figure 2.5: The spatial and temporal resolution of various imaging techniques. From [99].

2.2.1 EEG

The following overview on EEG is based on [226, 157, 197].

Acquisition

The electroencephalogram (EEG) provides a measurement of the electrical activity in the brain as a function of time by the means of electrodes placed on the scalp. It has a good temporal resolution and can characterise fast changes in current flow. However, its spatial resolution is limited by the number of electrodes used and due to the volume conduction properties of the head. More specifically, the electrical signals have to propagate through several layers of tissue, including CSF, the meninges, the skull and the scalp, which attenuate and filter the signals. Therefore, the synchronised behaviour of large $(10^4 - 10^7)$ neuron populations is required to generate potentials which are strong enough to be captured by scalp electrodes. In fact, EEG is believed to be generated by vertically oriented large pyramidal cells in the cortex, as the alignment of

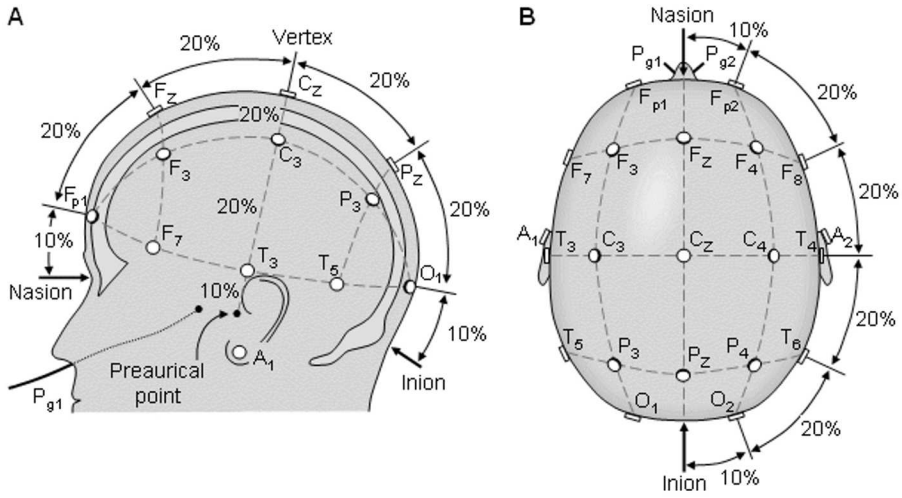

Figure 2.6: Electrode placement according to the International 10-20 system. From [100].

these cells allows the amplification of their extracellular fields. Note that it is the EPSPs and IPSPs - and not action potentials - which have slow enough temporal dynamics to overlap with each other in time and sum up to large current flows which give rise to the EEG signals. Typical EEG wave amplitudes measured on the scalp lie between 10 and 100μV.

Standard electrode positioning systems exist to make different EEG measurements comparable. According to the International 10-20 system the positions of the electrodes are computed as percentages of distances between specific landmarks on the head, as shown in Figure 2.6. The names of the electrodes are a combination of a letter and a number, where the letter indicates the corresponding brain region (F,P,O,T and C for frontal, parietal, occipital or temporal lobe and central line, respectively), while the number indicates whether the electrode is placed over the midline, the left or the right hemisphere (z for zero, odd and even numbers, respectively).

Each EEG channel measures the potential difference between two electrode sites. As such, EEG can be recorded using several different montages which can be divided in two main categories. In case of a reference montage all electrodes are referred to the same single electrode or to a signal combined from two or more electrodes. In a bipolar montage each electrode is referred to their adjacent electrode in left-to-right or front-to-back sequences. The particular advantages and disadvantages of these solutions depend on the type of EEG

pattern under investigation.

EEG patterns

In this section we focus on normal EEG patterns occurring in healthy individuals. Epileptiform EEG activity will be discussed in section 2.3.

Spontaneous EEG. The EEG reflects a continuous noise or roar of the brain [157], hence it has a fairly wide frequency spectrum. Typical EEG patterns depend on the maturity of the brain as well as on the vigilance state and the behaviour of the subject. In general, rhythmicity and reactivity are key features which can guide interpretation.

The frequency spectrum of EEG are conventionally broken down into the following subbands, each corresponding to different physiological or mental processes:

- Delta activity: 0.1-3.5 Hz
- Theta activity: 4-7.5 Hz
- Alpha activity: 8-13 Hz
- Beta activity: 14-30 Hz

Slower waves normally occur in different stages of wakefulness and sleep: while delta waves are prominently present in deep sleep, theta rhythms occur during drowsiness and light sleep. Alpha activity corresponds to an awake relaxed state with relative mental inactivity. It is most pronounced over the occipital region and with eyes closed. Beta activity is rather heterogeneous. It might occur over several regions, each of which correspond to different physiological phenomena, such as normal wakeful state, motor function, sometimes anxiety or onset of drowsiness and sleep. Recent research has been investigating brain activity in higher frequency bands than the ones in this traditional subdivision, both in normal subjects [214, 35] and in epileptic cases [182, 111].

Induced EEG patterns. The aim of many investigations is to study the reactivity of the brain to certain external or internal events. Some of these events induce peculiar waveforms on the EEG. However, these waveforms are usually of very small amplitude and are covered in ongoing background activity. As event related potentials (ERPs) are both time-locked and phase-locked to the stimulus or event eliciting them, they can be detected by simple time averaging. ERPs are composed of several positive and negative peaks

with well-defined latencies compared to the stimulus onset, each of which correspond to different stages of information processing in response to a sensory stimulus. Other types of EEG responses are only time-locked but not phase-locked to the event, such as event related desynchronisation and synchronisation (ERD/ERS), which occur during motor planning and imagery, sensory processing, perceptual, judgement and memory tasks. ERD/ERS can be assessed by envelope detection or bandpass filtering and power averaging the signal.

Although averaging might be an effective way to study global response mechanisms, recently there has been a lot of interest in single-trial analysis of these potentials. Brain computer interfaces (BCI) can benefit from accurate classification of single-trial responses. Moreover, in cognitive studies the fluctuation in response characteristics of various ERP components can provide insight in learning and adaptation processes.

EEG artefacts.

A potential limitation of EEG is the presence of artefacts which are superimposed on patterns of interest and may hinder interpretation. Artefacts may be of physiological or non-physiological origin.

Non-physiological artefacts include electrode and external device artefacts. Physiological artefacts originate from tissue outside the brain which generate electrical currents during their function or indirectly, inducing the movement of the electrodes or the body itself.

Cardiac activity related artefacts occur in the form of superimposed repetitive waves due to electrocardiographic (ECG) rhythms, pulsation causing the movement of vessels under the recording electrodes or ballistocardiographic (BCG) artefacts inducing the movement of the head and the whole body. The vertical and horizontal movements of the eye, as well as blinking causes large deflections on the frontal electrodes, also known as electrooculographic (EOG) artefacts. Muscle contraction or electromyographic (EMG) activity seriously obscures the EEG due to its high frequency and amplitude. Some examples are shown in Figure 2.7.

Physiological artefacts are in general more difficult to handle than non-physiological ones. The frequency content of physiological artefacts often overlap with the one of the EEG signal under investigation. Therefore, advanced signal processing techniques are needed to remove them without suppressing the underlying activity patterns.

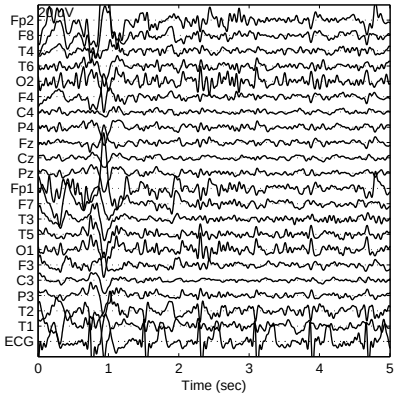

(a) Cardiac artefact

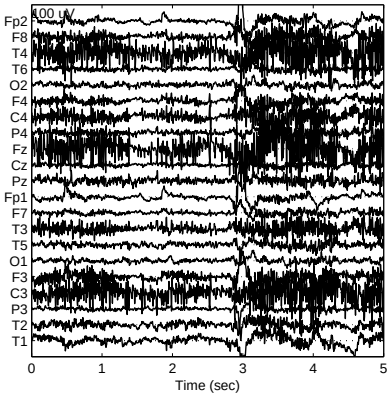

(b) Muscle artefact

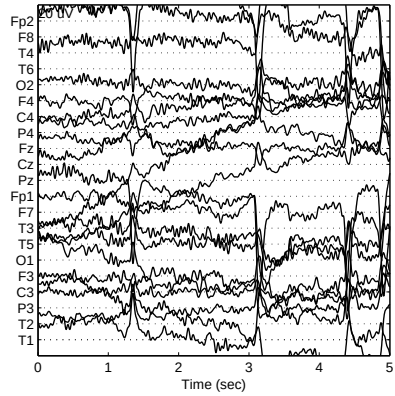

(c) Ocular artefact

Figure 2.7: Artefacts in the EEG

2.2.2 fMRI

The following overview on magnetic resonance imaging is based on [136].

Physical principles of magnetic resonance imaging

Magnetic resonance imaging measures the effect of radio frequency (rf) electromagnetic waves on dipoles in a magnetic field. In the neuroimaging context, the hydrogen atoms play the most important role due to their abundance in the human body. The nuclei of the hydrogen atom consist of a positively charged proton, and as such, are characterised by an angular momentum or spin. As moving electrical charges produce a magnetic momentum, the hydrogen nuclei will interact with the an external magnetic field. First, the hydrogen nuclei align with the magnetic field of the MR scanner. Subsequently, due to an excitation by a rf pulse, some nuclei leave their resting state and move into a higher energy state, aligning antiparallel to the magnetic field. Finally, after the excitation ends the nuclei return to their initial state. The rate of this relaxation depends on the properties of the nearby tissue. Moreover, the relaxation properties also depend on the specific timing and amplitude parameters of the rf excitation. The experimenter may apply various different excitation parameters and read out timing, generating contrast between different tissue types. Appropriate choice of these experimental parameters will reveal structural properties (anatomical imaging), flow (perfusion imaging) or neural activity (functional imaging).

The rate of relaxation is expressed by the time constants T1 and T2 of two exponential processes: the relaxation of the nuclei in the direction of the magnetic field (longitudinal re-growth), and in the direction perpendicular to it (transversal relaxation), respectively. The transversal relaxation plays an important role in functional MRI. As the energy transitions of a nucleus changes the local field of nearby nuclei, it introduces inhomogenities in the field. The transversal relaxation in such an inhomogeneous field is more rapid and is characterised by a decay constant called T2*. The physiological state of the brain, more specifically, the composition of the local blood supply determines the size of these inhomogeneities. Therefore, as the local blood supply varies on demand of neural activity, the T2* parameter provides indirect information on the ongoing neural activity.

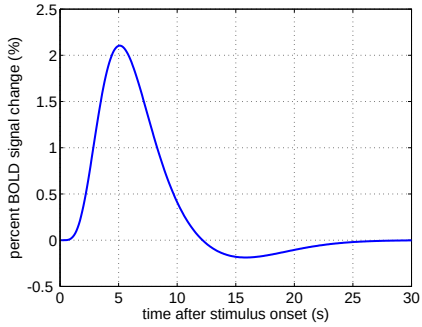

Figure 2.8: The canonical hemodynamic response function in the SPM toolbox

The BOLD signal

The mechanisms connecting the neural activity to the measured T2* signal are very complex and are not yet fully understood. Below we explain the basic underlying phenomena.

The changes of the T2* parameter is also referred to as the blood oxygen level dependent (BOLD) signal. As the name suggests, the signal is influenced by the relative concentration of the oxygenated and deoxygenated blood. In fact, deoxyhemoglobin is paramagnetic unlike oxygenated hemoglobyn. In consequence, it was observed that T2* decreases much faster in presence of deoxyhemoglobin.

As explained in section 2.1, the increased oxygen consumption during activation is overcompensated by excess cerebral blood flow. Therefore, in active brain regions the relative concentration of oxygenated hemoglobyn increases, resulting in larger T2* values, i.e. a positive BOLD response.

The time course of the BOLD signal corresponding to a transient neural activity is called the hemodynamic response function (HRF). The first BOLD signal change occurs roughly 2s after the onset of the neural activity and reaches a peak after 6-9s, and finally returns to baseline. An illustration of the HRF is shown in Figure 2.8. The exact characteristics of the HRF vary across the cortex, across different types of neural events and across patients or healthy individuals. Note that the HRF is a rather slow signal, considering that the neural activity in response to the same brief stimulus ends in a few hundred milliseconds.

2.3 Epilepsy

Epilepsy, the second most common neurological disorder after stroke, occurs in over 0.5% of the world population [37]. Epilepsy is a chronic neurological disorder characterised by recurrent epileptic seizures [18]. A seizure is defined as the transient occurrence of signs and/or symptoms due to abnormal excessive or synchronous neuronal activity in the brain [68]. Seizures originate and are sustained in a large neuronal population due to a certain loss of control over the crucial balance between inhibition and excitation. As inhibitory mechanisms fail, neurons become hyper-active and fire simultaneously with nearby neurons at a rate much higher than normal. The abnormal activity might spread to other regions in the brain through pathways which otherwise exist to facilitate normal function. There are different explanations on how a seizure terminates, including the depletion of oxygen supply to the neurons involved in the seizure, and chemical changes which restore the initial imbalance or lack of inhibition [226].

Depending on the brain regions involved in the seizure, the patient may have diverse clinical symptoms, including sensory dysfunction, loss of consciousness, motor automatisms, etc. The International League Against Epilepsy (ILAE) differentiates two main types of seizures, namely focal and generalised seizures. Focal epileptic seizures are conceptualized as originating within networks limited to one hemisphere, while generalised seizures are conceptualized as originating at some point within, and rapidly engaging, bilaterally distributed networks [14]. Prolonged seizures may develop into a continuous seizure or status epilepticus, a life-threatening condition in which there is no observable recovery between seizures. Throughout this thesis we will focus on focal epilepsies.

2.3.1 EEG monitoring in epilepsy

EEG is a very useful and well-established technique in epilepsy monitoring and diagnosis, as it can quantitatively show the changes in brain activity over time. Two types of epileptic events can be observed on the EEG, namely epileptic seizures in the form of ictal patterns, and short, transient events in between seizures also known as interictal discharges. Note that there is a grey zone between interictal and ictal activities and sometimes it is difficult to distinguish between them [157]. This is especially the case for generalised discharges.

Ictal epileptiform patterns of focal seizures are often stereotyped for the patient and can be very diverse. However, some features are commonly present, such as evolving, repetitive sharp waves. The evolution might be observed in

frequency, amplitude, topography and morphology. Frequency evolution can start from any normal EEG frequency band and may manifest as a decrease or an increase. Amplitude evolution means simply an increase in signal amplitude, typically following an attenuation at the beginning of the seizure. The seizure is spreading towards new brain regions from the source during its course, resulting in the appearance of the seizure pattern on more and more EEG channels, changing the topography of the activity. Finally, the morphology of the signal is influenced by the gradual replacement of the background activity by the ictal pattern and it corresponds to a gradual decrease of complexity of the overall EEG pattern. Infrequently no evolution occurs but the ictal pattern consists of regular repetitive spikes, desynchronisation, or regular rhythmic slowing [197].

The ictal pattern of generalised seizures are mostly characterised by either generalised spike and slow wave complexes, generalised paroxysmal fast activity or electrodecrement [197].

Focal interictal epileptiform discharges (IEDs) are mostly described by the following four features: a field that extends beyond one electrode, a sharply contoured component, electronegativity on the cerebral surface and disruption of the surrounding background activity. The sharply contoured component can be a spike or a sharp wave, and is asymmetric. It might form a complex or a polyspike if followed by a slow wave or successive spikes, respectively. Such complexes or polyspikes are common in generalised IEDs. The field of generalised IEDs is larger than of focal IEDs, usually extending to the frontal and parietal regions [197].

IEDs are present in 90% of epilepsy patients. As they occur much more frequently than seizures, they are powerful indicators of the disease. However, the assessment of seizures during long-term EEG monitoring or Video-EEG monitoring is necessary for [169, 13]:

- diagnosis of epilepsy versus nonepileptic events
- diagnosis of seizure type and epilepsy syndrome
- localising the area of onset in case of focal epilepsies
- taking precautions to avoid danger and to comfort the patient during seizures

2.3.2 Functional MRI in epilepsy

As we have seen in the previous section, EEG monitoring can be used to observe epileptiform events, moreover, to localise the onset region of the

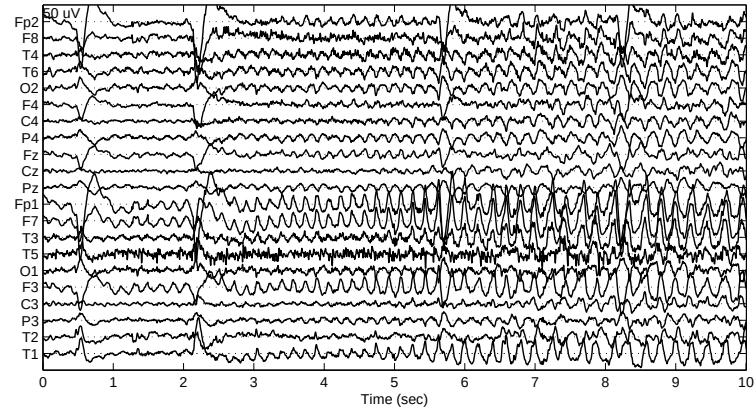

(a) Seizure from a temporal lobe epilepsy patient. The seizure onset is characterised by rhythmic 5Hz theta activity on the left fronto- antero- and mid-temporal electrodes.

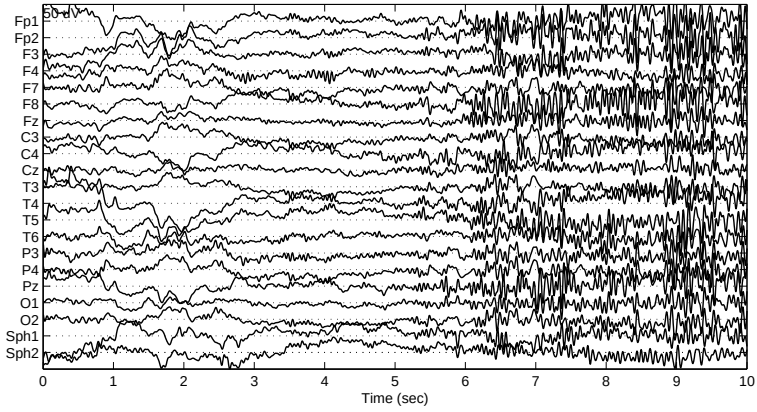

(b) Seizure from a frontal lobe epilepsy patient. The seizure onset is characterised by a general attenuation, followed by a fast beta band activity.

Figure 2.9: Ictal patterns in the EEG

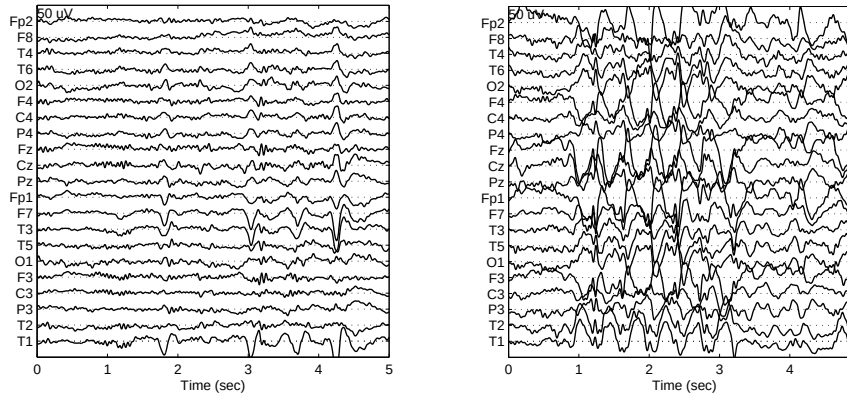

(a) Focal IEDs most pronounced over the left frontotemporal region.

(b) Generalised spike-wave discharges.

Figure 2.10: Interictal patterns in the EEG

seizures. Note, however, that due to the poor spatial resolution of EEG the accuracy of the localisation is limited to determining the affected lobe and the laterality. However, the combination of EEG and fMRI, due to the higher spatial resolution of the latter, might allow more precise delineation of the epileptic source.

In order to localise epileptic brain regions, one has to look for voxels in which the BOLD fluctuations correlate with the timing of epileptic patterns on the EEG. On one hand, investigating hemodynamic correlates of seizures yielded promising results in various studies. On the other hand, such an approach is impractical as seizures are rare events and might not occur during the limited time of the fMRI recordings, moreover, vigorous movement inside the scanner during seizures may pose risk to the patient and causes severe artefacts in the fMRI signals. Therefore, most studies target BOLD signal changes in response to interictal epileptic discharges [29].

In practice, mapping hemodynamic correlates of interictal epileptic discharges involves statistical analysis within the framework of the general linear model (GLM), based on the work of [73]. In this approach each fMRI voxel time course is compared to a model representing the expected signal fluctuations. As we have seen in the previous chapters, there is a mismatch between the dynamics of the EEG and the BOLD signal arising from the same neural activity. To account for this mismatch in the model, the timing of the IEDs

are convolved with the hemodynamic response function. Finally, an activation map is created where each voxel value reflects the statistical similarity between the voxel time course and the model, i.e. the plausibility that the given brain region contributes to the generation of the IEDs or is affected by them.

2.4 Presurgical evaluation in epilepsy

Approximately 30% of epilepsy patients are non-responsive to anti-epileptic drugs [63], a condition called refractory epilepsy. As their quality of life is seriously compromised, surgical resection has to be considered.

The final goal of the presurgical evaluation is to delineate the epileptogenic zone. The definition states that the total resection or disconnection of the epileptogenic zone is necessary and sufficient for seizure freedom [175]. However, the epileptogenic zone is a hypothetical region, i.e. there is no diagnostic modality which can directly indicate it. One has to infer to its location indirectly by defining several other relevant zones, which are involved in generating the epileptic disorder or its electrographical and clinical symptoms. Therefore, the presurgical evaluation is a multidisciplinary procedure collecting information from several imaging modalities and other diagnostic tools. An overview of these regions, their definitions and the corresponding diagnostic tools are summarised in Table 2.1.

If all diagnostic data are concordant, the epileptogenic zone is resected or disconnected unless it is in eloquent cortex, i.e. in a region which is indispensable for any cortical function, such as the execution of motor, sensory, cognitive or memory tasks. Systematic reviews showed that 66-70% and 41-79% of patients are rendered seizure free after short term and long term follow up (</> 5 years), respectively [193].

2.4.1 Current practice

In the epilepsy monitoring unit (EMU) in UZ Leuven the procedure below is followed for presurgical evaluation. Physical, neuropsychological and neurological examinations are conducted, and seizure history is obtained.

In order to identify structural abnormalities, high-resolution MRI is applied. MRI is the most sensitive technique for the diagnosis of mesial temporal sclerosis (MTS), tumors, and malformations of cortical development. While small tumors are frequent causes of epilepsy in adults, MTS is the most common association with temporal lobe epilepsy. Moreover, developmental

Table 2.1: Overview and definition of key zones and lesions in epilepsy, based on [175]

Zone	Definition: Area of the cortex...	Diagnostic tool
Epileptogenic zone	generating the seizures; total resection or disconnection is necessary and sufficient for seizure freedom	theoretical concept
Ictal symptomatogenic zone	producing the initial seizure symptoms	History, visual video analysis
Irritative zone	generating interictal epileptiform discharges	EEG, MEG, EEG-fMRI
Seizure onset zone	where the clinical seizures are generated	EEG, SPECT
Epileptogenic lesion	structural lesion which causes the seizures	MRI, CT
Functional deficit zone	functionally abnormal in the interictal period	neuro(psycho)logical examination, PET, SPECT, non-epileptiform EEG and MEG activity
Eloquent cortex	indispensable for certain cortical (motor, sensory, cognitive, memory) function	Cortical stimulation, fMRI, TMS, MEG, EP, PET, Wada test

malformations constitute the most prevalent underlying pathology in infants and young children with epilepsy [124]. Therefore, MRI has a crucial role in the presurgical planning in case of these pathologies.

Further, the patients undergo long-term video-EEG monitoring, normally lasting 5 days. During this period the anti-epileptic medication is reduced to allow seizures to occur for observation. Interictal scalp recordings are analysed in order to define the irritative zone based on the field of the IEDs. During seizures ictal semiology is assessed on video images and the ictal EEG patterns are inspected for the seizure onset zone (SOZ).

Note, however, that epileptic discharges of small amplitude or of deep origin are not detected by scalp recordings. Intracranial electrodes, on the other hand,

provide very sensitive recordings of such activity. Although intracranial EEG recordings are available for some patients in the EMU, it is not part of the standard procedure. Its disadvantages include its invasive nature and the fact that only a small area of the entire brain can be covered, posing the risk of missing part of the SOZ.

At seizure onset a brain perfusion tracer is injected in order to perform an ictal single-photon emission computed tomography (SPECT). Injection has to happen as early as possible to limit the presence of propagation patterns on the image. As a result, the area of most intense hyperperfusion can localise the SOZ. Methodologically speaking, both ictal and interictal scans are performed and subtracted to obtain difference images. Subtraction ictal SPECT co-registered to MRI (SISCOM) can improve the localisation and visualisation of the region of hyperperfusion [218].

Finally, patients are scanned with positron emission tomography (^{18}F-FDG PET), in order to map cerebral metabolism. It is assumed that the region of predominant hypometabolism contains the epileptogenic zone [219]. In comparison with SPECT, PET has greater spatial resolution and versatility considering that multiple tracers can image various aspects of cerebral function [194]. Note that the latter is also true for SPECT, however, only a few tracers are used in practice.

2.4.2 Possible improvements

Automatic seizure detection

As explained above, EEG monitoring is a crucial tool in epilepsy diagnosis and presurgical evaluation. The benefits of the automatic analysis of EEG recordings are twofold. First, consider that the objective is to discover all seizure occurrences. As the monitoring of one patient takes several days, the amount of data to be analysed is huge. Therefore, an automatic seizure detection technique supporting visual EEG analysis would drastically decrease the workload of clinicians. Besides, as the seizure spreads quickly through the brain, the early detection of the epileptic seizure is crucial. Due to its fine temporal resolution, EEG can provide accurate information about the seizure onset. To be on alert for clinical symptoms is insufficient as they may arise later on in the course of a seizure. Moreover, subclinical seizures are completely omitted that way. Continuous inspection of EEG is, however, impractical. Therefore, an automatic seizure alarm system can be useful to facilitate early intervention, including ensuring patient safety, comforting the patient and injecting a radio tracer to prepare ictal SPECT.

In chapter 4 we present two novel solutions, a universal and a patient-specific seizure detection system.

Ictal source localisation

Since the 1950's ictal EEG recordings are routinely used and still remain the gold standard for defining the seizure onset zone [175, 162]. Ictal EEG can provide correct localisation in about 70% of cases, however, it is often obscured with muscle and other types of artefacts [195]. Recent studies applying various mathematical decomposition or blind source separation (BSS) techniques significantly improved the interpretabily of this technique by removing the contaminating artefacts, e.g. [15, 112, 216, 56, 227].

In addition, BSS techniques were also proven useful in extracting the ictal source from the mixture of background activity and artefacts. The topographic maps corresponding to the ictal component can indicate the lateralisation [153] and even the localisation of the seizure, corresponding to the clinically determined seizure onset region [1, 52].

BSS methods, nevertheless, are not used in clinical practice at present. Most of these methods work semi-automatically and still need visual assessment of the sources. Moreover, each decomposition method implies particular assumptions on the underlying sources, which may or may not hold for the actual signals. Therefore, different BSS techniques may prove to be optimal in different situations.

Chapter 5 explores the applicability of a recently introduced BSS method, namely block term decomposition. We expect that thanks to its flexibility, this technique is capable of modelling nonstationary ictal sources, which evolve in morphology or topography during their course.

Interictal source localisation

Simultaneous EEG-fMRI has proven to be useful in localizing interictal epileptic activity [80, 177] and defining the irritative zone as part of presurgical evaluation [234].

As explained in section 2.3.2, standard analysis uses the timing of interictal discharges based on EEG to find regions with correlated blood oxygen level dependent (BOLD) signal changes recorded by fMRI within the standard general linear model (GLM) approach. However, marking interictal discharges on the EEG is time-consuming; furthermore, EEG does not always provide

reliable information on the epileptic events. Neural activity of deep structures is not visible on EEG [32, 140, 203], moreover, the severe gradient and ballistocardiogram (BCG) artefacts due to the magnetic field in the scanner often make the interpretation of the EEG ambiguous [12, 85]. Several approaches exist to reduce such artefacts (for a comparison study, see [222]), however, residual artefacts still hinder interpretation. Most importantly, some patients might not show interictal activity during the limited time of the fMRI sessions. In a recent study only 37% of consecutively scanned patients showed clinically concordant epileptic spikes [213], thus, in the vast majority of cases, GLM-based analysis could not be carried out. It has been reported previously, that EEG-fMRI studies fail in 40-70% of cases [84], due to the reasons mentioned above or due to the lack of significant BOLD changes correlated to interictal activity. Therefore, there is a strong demand for techniques capable of localizing the epileptic activity without any information on its timing.

In chapter 6 a data-driven tool, namely independent component analysis (ICA) is investigated for this purpose.

Chapter 3

Machine learning techniques

Machine learning is "the capability of the computer program to acquire or develop new knowledge or skills from existing or non existing examples for the sake of optimising performance criterion" [7]. More formally, given a task T, a performance criterion C and an experience E, learning means that the machine improves at solving task T as measured by C, based on information in E [145].

Traditionally, there are two fundamentally different tasks within machine learning [28]. In supervised learning a specific desired output is given corresponding to each training example or input. In this case the goal of the machine is to learn a mapping from the input to the output space [75], in order to produce a correct output given a new input. The output space may contain class labels in case of a classification task, or real numbers in case of a regression task. Conversely, in unsupervised learning no training examples or target outputs are given. Instead, the goal here is to find interesting structure underlying the input data [28]. In other words, unsupervised learning aims at building representations of the input data that can be used for decision making, predicting future inputs, or efficiently communicating inputs to other machines [75]. Accordingly, subdisciplines of unsupervised learning include clustering, dimensionality reduction, blind source separation, etc.

In the following sections we will give the mathematical formulation of various blind source separation and binary classification techniques that are applied in this thesis. In order to do so, we first establish some notations and definitions.

3.1 Notation and definitions

The field of real numbers are denoted by $\mathbb{R}$, while the filed of real or complex numbers are denoted by $\mathbb{K}$. Vectors are denoted by boldface lower case letter, e.g. $\mathbf{a}$. Matrices are denoted by boldface capital letters, e.g. $\mathbf{A}$, while tensors are denoted by calligraphic letters, e.g. $\mathcal{A}$. An entry of a vector $\mathbf{a}$, a matrix $\mathbf{A}$, or a tensor $\mathcal{A}$ is denoted by a_i, $a_{i,j}$ or $a_{i,j,k}$, etc., depending on the number of modes. Mode–n vectors are the generalisation of matrix rows and columns to tensors. A mode–n vector is a vector in which all but one of the indices are fixed.

Definition 1. The Kronecker product of two matrices $\mathbf{A}$ and $\mathbf{B}$ is denoted by $\mathbf{A} \bigotimes \mathbf{B}$ and is defined as

$$\mathbf{A} \bigotimes \mathbf{B} = \begin{bmatrix} a_{11}\mathbf{B} & a_{12}\mathbf{B} & \cdots \\ a_{21}\mathbf{B} & a_{22}\mathbf{B} & \cdots \\ \vdots & \vdots & \ddots \end{bmatrix}$$

Definition 2. The mode-n product of a tensor $\mathcal{A} \in \mathbb{K}^{I_1 \times I_2 \times \cdots \times I_N}$ with a matrix $\mathbf{U} \in \mathbb{K}^{J \times I_n}$ is denoted as $\mathcal{A} \times_n \mathbf{U}$ and is of size $I_1 \times \cdots \times I_{n-1} \times J \times I_{n+1} \times \cdots \times I_N$. The entries of the mode-n product are defined as:

$$(\mathcal{A} \cdot_n \mathbf{U})_{i_1 \cdots i_{n-1} j i_{n+1} \cdots i_N} = \sum_{i_n=1}^{I_n} a_{i_1 i_2 \cdots i_n \cdots i_N} u_{j i_n}.$$

Definition 3. The outer product $\mathcal{A} \circ \mathcal{B}$ of a tensor $\mathcal{A} \in \mathbb{K}^{I_1 \times \cdots \times I_M}$ and a tensor $\mathcal{B} \in \mathbb{K}^{J_1 \times \cdots \times J_N}$ is the tensor defined by:

$$(\mathcal{A} \circ \mathcal{B})_{i_1 \cdots i_M j_1 \cdots j_N} = a_{i_1 \cdots i_M} b_{j_1 \cdots j_M}, \tag{3.1}$$

for all different values of the indices.

Definition 4. The Khatri-Rao product of two matrices $\mathbf{A} \in \mathbb{K}^{I \times K}$ and $\mathbf{B} \in \mathbb{K}^{J \times K}$ is defined as $\mathbf{A} \odot \mathbf{B} = [a_1 \otimes b_1 \cdots a_K \otimes b_K]$

Definition 5. The k-rank of a matrix $\mathbf{A}$, denoted as k_A, is defined as the maximum value k such that any k columns of $\mathbf{A}$ are linearly independent.

Definition 6. The mode–n matricisation or unfolding $\mathbf{A}_{(n)}$ of an Nth-order tensor $\mathcal{A} \in \mathbb{K}^{I_1 \times I_2 \cdots I_N}$ maps the tensor element with indices $(i_1, \cdots, i_N)$ to a matrix element (i_n, j) such that

$$j = 1 + \sum_{k=1, k \neq n}^{N} (i_k - 1) J_k \text{ with } J_k = \begin{cases} 1 & \text{for } k = 1 \text{ or } (k = 2 \text{ and } n = 1) \\ \prod_{m=1, m \neq n}^{k-1} I_m & \text{otherwise.} \end{cases} \tag{3.2}$$

For a third order tensor, the unfolding takes the form:

$$(\mathbf{A}_{(1)})_{i_1,(i_2-1)I_3+i_3} = (\mathcal{A})_{i_1 i_2 i_3},$$

$$(\mathbf{A}_{(2)})_{i_2,(i_3-1)I_1+i_1} = (\mathcal{A})_{i_1 i_2 i_3},$$

$$(\mathbf{A}_{(3)})_{i_3,(i_1-1)I_2+i_2} = (\mathcal{A})_{i_1 i_2 i_3},$$

for all values of the indices.

3.2 Unsupervised learning: blind source separation

Blind source separation (BSS) considers the problem of processing multidimensional observations which arise as a noisy linear mixture of a number of underlying source signals. More formally, let $\mathbf{x}(t) = \begin{bmatrix} x_1(t) & \cdots & x_P(t) \end{bmatrix}^T \in \mathbb{R}^P$ be the observed signal at time instant t, and $\mathbf{s}(t) = \begin{bmatrix} s_1(t) & \cdots & s_N(t) \end{bmatrix}^T \in \mathbb{R}^N$ the underlying sources. Then $\mathbf{x}(t)$ can be written as [31]

$$\mathbf{x}(t) = \mathbf{A}\mathbf{s}(t) \tag{3.3}$$

where $\mathbf{A}$ is an unknown mapping from $\mathbb{R}^N$ in $\mathbb{R}^P$. The goal of blind source separation is to find the sources $\mathbf{s}(t)$ and the mapping or mixing matrix $\mathbf{A}$ which provides information about the relative contribution of the sources to each observed signal in $\mathbf{x}(t)$. However, this problem is ill-posed and one has to make some assumptions about the underlying sources in order to reach a unique solution [31]. Different assumptions lead to different decomposition techniques, which will be presented below. Note, however, that there are two inherent ambiguities to this problem, namely the order and the norm of the sources, as they can be compensated by the inverse scaling and permutation of the columns of the mixing matrix. We call a decomposition unique if it is only subject to these indeterminacies.

Below we discuss various mathematical decompositions solving the BSS problem, that are applied in this thesis.

3.2.1 Singular value decomposition and principal component analysis

Any matrix of real or complex values can be written as the following:

$$\mathbf{M} = \mathbf{U}\Sigma\mathbf{V}^*, \tag{3.4}$$

where $\mathbf{U}$ and $\mathbf{V}$ are unitary matrices, $\mathbf{V}^*$ is the conjugate transpose of $\mathbf{V}$, and $\mathbf{\Sigma}$ is a diagonal matrix. The diagonal elements of $\mathbf{\Sigma}$, denoted as σ_i, are positive by convention, appear in decreasing order, and are called the singular values of $\mathbf{M}$. In case the singular values are distinct the decomposition is unique up to the joint reflection of the columns of $\mathbf{U}$ and $\mathbf{V}$ The columns of $\mathbf{U}$ and $\mathbf{V}$ are called the left and right singular vector of $\mathbf{M}$, and denoted as U_i and V_i, respectively. Alternatively, $\mathbf{M}$ can be written as the weighted sum of their outer products:

$$\mathbf{M} = \sum_i \sigma_i U_i \circ V_i, \tag{3.5}$$

The number of non-zero singular values is the rank of the matrix. Truncating the summation at the first r elements gives the best rank-r approximation of $\mathbf{M}$ in least-squares sense.

Singular value decomposition (SVD) is closely related to the concept of principal component analysis (PCA). Consider the problem of projecting the observed data into a new, orthonormal basis, which will reveal hidden structure and filter out noise [185]. Note that there is no unique solution to this problem, as any rotation of the obtained basis is a valid solution as well. PCA offers a possible way to obtain a unique orthonormal basis, also called the principal components, by taking the columns of $\mathbf{V}$. The principal components are ordered based on the amount of variance they express. Therefore, omitting the last principal components leads to a dimensionality reduction which preserves most of the variability in the data. SVD — and PCA — found several other important applications in signal processing, including the solution of least squares problem, noise filtering or features extraction. In the context of BSS the sources of interest are expressed as the original signals projected onto the new principal component basis [185]. As such, this model assumes that the sources underlying the observed signal are mutually uncorrelated [45].

3.2.2 Independent component analysis

Independent component analysis (ICA) imposes a statistical diversity among the underlying sources. With such a constraint ICA overcomes the rotational invariance property of PCA. Several ICA algorithms exist which formulate statistical independence in different ways.

A commonly used assumption for ICA is that the sources are temporally independent and identically distributed (iid) and are non-Gaussian. In an initial prewhitening step, the observations are transformed to a new stochastic vector of unit covariance. During this procedure an estimation of the signal subspace is also obtained from the eigenvalue decomposition of the observed covariance. However, the mixing matrix remains unknown up to an orthogonal factor. In a second step higher order statistics are used to fix the rotational degrees of freedom of the mixing matrix. Considering that the higher order cumulants of mutually statistically independent processes are diagonal tensors, the mixing matrix can be estimated by diagonalising the cumulant [46]. *JADE* (joint approximate diagonalisation of eigenmatrices) is a popular, computationally efficient algorithm solving this problem.

Another class of ICA algorithms achieve separation by an iterative approach which aims at optimising a so-called contrast function measuring a certain property of the separated sources. One such contrast function is based on the *Infomax* (information maximisation) principle [10]. This method maximises the information content of the sources, measured by Shannon's entropy. It can be shown that under the assumption of independent sources this information maximisation criteria is equivalent to the minimisation of the mutual information between the sources [31]. The *FastICA* algorithm is a highly efficient algorithmic approach to solve the optimisation problem underlying certain ICA formulations. The contrast function of FastICA can be chosen either in the framework of maximum likelihood or higher order statistics. Thanks to using the Newton method for the iterative optimisation [109], the algorithm converges quadratically if the data truly follows the ICA model.

Finally, a different class of ICA approaches arises if one assumes that the sources are not iid in time — which is the case in many practical BSS problems [31]. Instead, they exhibit some structure in terms of temporal correlation or other statistical characteristics. In case these statistics exhibit sufficient diversity, separation can be achieved using second order statistics. In fact, it becomes possible to separate Gaussian sources as well, as opposed to the classical iid ICA model. The *SOBI* (Second order blind identification) algorithm [11] applies approximate joint diagonalisation on a set of matrices including the correlation matrices at different time lags $\tau = 0, 1, \cdots, M$.

3.2.3 Canonical correlation analysis

Canonical correlation analysis [94] was originally proposed to describe the relationship between two sets of variables. Given two matrices, each containing the realisations of two multivariate vectors, CCA generates a new pair of vectors from the linear combination of the columns of each original matrix in a way that the correlation between the new vectors are maximised. The new vectors and their correlation are called canonical variates and canonical correlation coefficient, respectively.

When applied as a BSS technique, CCA assumes sources which are mutually uncorrelated and maximally autocorrelated [72]. The separation is achieved by considering the observation matrix $\mathbf{X} = \begin{bmatrix}\mathbf{x}(1) & \cdots & \mathbf{x}(T-1)\end{bmatrix}$ and its temporally delayed version $\mathbf{Y} = \begin{bmatrix}\mathbf{x}(2) & \cdots & \mathbf{x}(T)\end{bmatrix}$ as inputs. Consequently, the extracted components — the canonical variates, which explain most of the cross variance between X and Y, — are maximally autocorrelated at lag 1. The sources are extracted in descending order based on their canonical correlation coefficient.

3.2.4 Canonical polyadic decomposition

As we have seen in the previous sections, the problem of matrix decomposition is ill-posed and additional constraints are needed in order to obtain a unique solution. Interestingly, tensors admit unique decompositions under mild conditions.

Canonical polyadic decompomposition (CPD) approximates a third order tensor $\mathcal{T} \in \mathbb{K}^{I_1 \times I_2 \times I_3}$ with a sum of R rank-1 tensors:

$$\mathcal{T} \approx \sum_{r=1}^{R} \mathbf{a}_r \circ \mathbf{b}_r \circ \mathbf{c}_r. \tag{3.6}$$

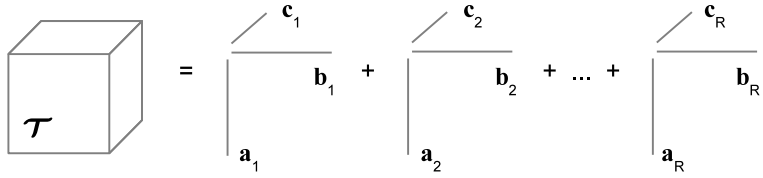

Figure 3.1: CPD of a tensor $\mathcal{T}$ in R rank-1 terms

.

CPD is visualised in Figure 3.1. Note that the definition is formulated for third-order tensors, however, the model can be extended to higher order tensors in a straightforward manner. The rank of the tensor is defined as the smallest R for which (3.6) is exact. Let $\mathbf{A} = [\mathbf{a}_1 \cdots \mathbf{a}_R]$, $\mathbf{B} = [\mathbf{b}_1 \cdots \mathbf{b}_R]$ and $\mathbf{C} = [\mathbf{c}_1 \cdots \mathbf{c}_R]$ be the factor matrices corresponding to each mode. Then, CPD can be alternatively written as

$$\mathbf{T}_{(\mathbf{1})} \approx \mathbf{A} \cdot (\mathbf{B} \bigodot \mathbf{C})^T. \tag{3.7}$$

The advantage of the CPD model is its uniqueness up to permutation and scaling under the following mild conditions [120]:

$$k_A + k_B + k_C \geq 2R + 2 \tag{3.8}$$

A more general framework for uniqueness has been recently presented in [59, 58].

3.2.5 Block term decomposition

Block term decomposition (BTD), introduced in [42, 41, 47] generalises CPD, as it allows components of low multilinear rank, as opposed to the rank–1 model of CPD. In this thesis we consider a particular case, decomposition into rank-$(L_r, L_r, 1)$ terms.

The rank-$(L_r, L_r, 1)$ block term decomposition of a third order tensor $\mathcal{T} \in \mathbb{K}^{I_1 \times I_2 \times I_3}$ into a sum of rank-$(L_r, L_r, 1)$ terms $(1 \leq r \leq R)$ is given as

$$\mathcal{T} \approx \sum_{r=1}^{R} \left(\mathbf{A}_r \cdot \mathbf{B}_r^T \right) \circ \mathbf{c}_r, \tag{3.9}$$

in which the matrix $\mathbf{D}_r = \mathbf{A}_r \cdot \mathbf{B}_r^T \in \mathbb{K}^{I_1 \times I_2}$ has rank L_r and the vector $\mathbf{c}_r$ is nonzero. In addition to permutation and scaling, inherited from the CPD, the factors $\mathbf{A}_r$ may be postmultiplied by any nonsingular matrix $\mathbf{F}_r \in K^{L_r \times L_r}$, provided that $\mathbf{B}_r^T$ is premultiplied by the inverse of $\mathbf{F}_r$. When the matrices $[\mathbf{A}_1 \cdots \mathbf{A}_R]$ and $[\mathbf{B}_1 \cdots \mathbf{B}_R]$ are full column rank and the matrix $[\mathbf{c}_1 \cdots \mathbf{c}_R]$ does not contain collinear columns, the decomposition is guaranteed to be unique up to the above indeterminacies.

Figure 3.2 visualises the decomposition of a tensor in rank-$(L_r, L_r, 1)$ terms.

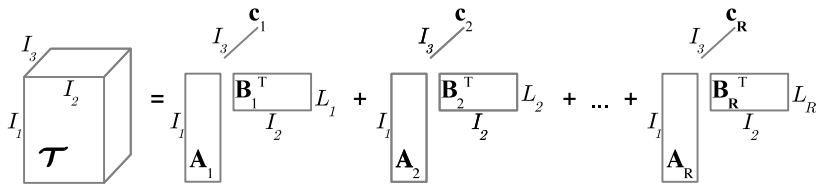

Figure 3.2: BTD of a tensor $\mathcal{T}$ in rank-$(L_r, L_r, 1)$ terms.

3.3 Supervised learning: binary classification

As explained in the beginning of this chapter, supervised learning aims at building data representations and inference techniques for making decisions about the input data. In this thesis we concentrate on techniques which can assign the input data to one of two predefined categories, or, in other words, make binary decisions. We will start with introducing an early intelligent system — rather than a learning machine — that can address this problem. Subsequently, we discuss some general theoretical considerations regarding supervised learning. Finally, three binary classification techniques, which are also applied in this thesis, are presented in detail.

3.3.1 From rule based expert systems to supervised learning

Rule based expert systems (RBS) are a fundamental tool in artificial intelligence which aim at "codifying the problem-solving know-how of human experts" [90]. The RBS works based on the following principle [155]. The domain knowledge in stored in the knowledge base in the form of a set of if-then rules. The database collects a set of facts or observations $\mathbf{x}_i$ about the data which is matched against the rules in the knowledge base. Then, the inference engine carries out the reasoning and reaches a solution y_i. The advantage of such expert system is its transparent nature, that is, the user has an insight into how a particular solution is reached. However, these systems possess a static knowledge base, hence, they lack the ability to learn.

Nowadays, developments in machine learning and Bayesian statistics allow the combination of domain knowledge with observed data in various generative modelling approaches. Interestingly, completely data-driven discriminative approaches provide superior performance despite their naive models [110]. The supervised learning techniques employed in this thesis fall into this second category.

3.3.2 Problem formulation

The supervised learning task can be formulated as inferring a model, a mapping or function $y = f(\mathbf{x})$, based on a set of training examples of input-output pairs $(\mathbf{x}_1, y_1), \cdots, (\mathbf{x}_n, y_n)$, where $\mathbf{x}_i = [x_{i,1}, \cdots, x_{i,d}]^T \in \mathbb{R}^d$ containing certain characteristics or features of the data. In the context of regression $y \in \mathbb{R}$ is a continuous variable, while in classification problems y is categorical, e.g. in case of a binary classification task $y = \{-1, 1\}$ [66]. Throughout this thesis we will consider binary classification problems.

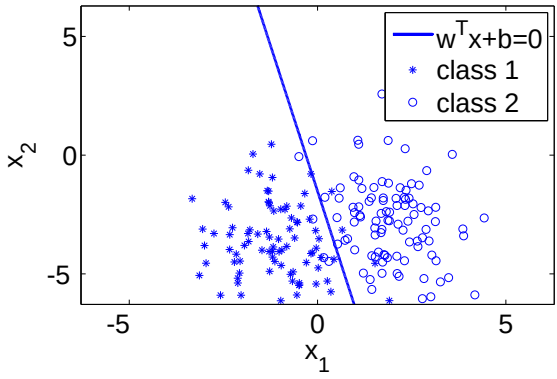

Figure 3.3: Illustration of a linear classification problem. The data are represented by two features, x_1 and x_2. The hyperplane separating the classes is characterised by its normal vector w and bias term b. Note that no perfect linear separation is possible in this case.

The set of possible functions for $f(\mathbf{x})$ is typically restricted to a specific class of functions, e.g. to linear functions [130]. Figure 3.3 visualises a binary classification task with a linear decision function, where the data are represented as $d = 2$ dimensional vectors, i.e. are described by 2 features. A linear decision function corresponds to a separating hyperplane and is characterised by its normal vector $\mathbf{w}$ and a bias term b. More complex — nonlinear — decision functions depend on a larger set of parameters α. In this context, the decision function is denoted as $f(\mathbf{x}, \alpha)$. Now, the goal of the learning task is to find the optimal parameters α based on the available training data. In order to do so, one has to specify a certain loss function $l(y_i, f(x_i, \alpha))$, which quantifies the goodness of the model. Then, the optimal decision function can be retrieved by minimising the following functional:

$$R_{emp}(\alpha) = \frac{1}{n} \sum_{i=1}^{n} l(y_i, f(x_i, \alpha)) \tag{3.10}$$

where $R_{emp}(\alpha)$ is called the empirical risk and (3.10) is the well-known empirical risk minimisation principle [225].

A very crucial property of a classifier is its generalisation capability, i.e. how well it approximates unseen data. In other words, it is not sufficient to choose a classifier which performs best on the training examples, but one has to evaluate its performance on an independent test set. Several alternatives exist to split the available data into training and test set, such as resubstitution, the hold-out method, bootstrapping, or cross-validation [121]. During a k-fold cross-validation the data is divided into k subsets of equal sizes. In each iteration one subset is set aside for testing and the combination of the remaining $k-1$ subsets is used to train the classifier. After repeating this procedure k times, an average performance estimate is taken. In case k equals the cardinality of the dataset, the method is called leave-one-out cross-validation.

The generalisation property of a classifier is closely related to its complexity, i.e. the number of parameters which controls its behaviour. On one hand, a model with few parameters does not offer enough flexibility and will give poor predictions. On the other hand, a model with too many parameters, which is able to capture very fine details of the data, is prone to modelling noise, thereby, carries the risk of poor generalisation. These phenomena are called underfitting and overfitting, respectively, and are closely related to the concept of the bias-variance trade-off [16]. More specifically, bias is associated with underfitting, i.e. the classifier does not match the data well enough, while variance corresponds to overfitting, that is, the classifiers fitted on various subsets of the same data are different from each other [121].

One way of controlling the model complexity is through regularisation [16]. This procedure involves, in addition to the error function, the introduction of a penalty term, which measures some aspect of the model complexity. The degree of regularisation can be adjusted by a multiplicative regularisation parameter. It is important to choose an appropriate regularisation parameter based on the available training data. This choice can be made, again, using cross-validation.

After this general theoretical introduction we give a description of the specific learning techniques used in this thesis.

3.3.3 Linear discriminant analysis

Linear discriminant analysis (LDA) aims at assigning each observation $\mathbf{x}_i$ to the class to which it belongs with the highest posterior probability, as expressed by Bayes's theorem [70]. Under the assumption that the data are sampled from a multivariate normal distribution with class means μ_1 and μ_2 and the class covariance matrices $\mathbf{S}_1 = \mathbf{S}_2 = \mathbf{S}$ are equal, the decision function takes the form [126]:

$$f(\mathbf{x}) = D(\mathbf{x}) = [x - \frac{1}{2}(\mu_1 + \mu_2)]^T S^{-1}(\mu_1 - \mu_2), \tag{3.11}$$

Alternatively, one can write [183]:

$$\begin{aligned} D(\mathbf{x}) &= \mathbf{w}^T x + b \\ \mathbf{w} &= (\mu_1 - \mu_2)S^{-1} \\ b &= -\frac{1}{2}(\mu_1 + \mu_2)\mathbf{w}^T \end{aligned} \tag{3.12}$$

Then $\mathbf{w}$ and b are the normal vector and the bias describing the hyperplane which separates the classes. Fisher's discriminant analysis (FDA) [67] derives $\mathbf{w}$ by maximising the Rayleigh coefficient, i.e. the ratio of between-class variance to within-class variance:

$$J(\mathbf{w}) = \frac{\mathbf{w}^T \mathbf{S}_B \mathbf{w}}{\mathbf{w}^T \mathbf{S}_W \mathbf{w}} \tag{3.13}$$

where $\mathbf{S}_W = \sum_{i=1}^{2} \mathbf{S}_i$ with $\mathbf{S}_i = \sum_{\mathbf{x} \epsilon C_i} (\mathbf{x} - \mu_i)(\mathbf{x} - \mu_i)^T$ is the within-class and $\mathbf{S}_B = \frac{1}{2} \sum_{i=1}^{2} (\mu - \mu_i)(\mu - \mu_i)^T$ with $\mu = \frac{1}{2} \sum_{i=1}^{2} \mu_i$ is the between-class variance. A solution to (3.13) can be found via generalised eigenvalue decomposition (GEVD). For details see [78] and references therein. Note that (3.13) and (3.12) lead to the same solution.

Although LDA is very popular approach due to its simplicity and low computational complexity, it has certain limitations. As the class means and covariance matrices are not known, they have to be estimated from the data. Therefore, this approach is very sensitive to outliers, which should preferably be removed before learning. Moreover, in case of small sample sizes, the empirical

covariance matrix is systematically biased towards larger eigenvalues. In order to overcome this issue, regularised or shrinkage LDA replaces the empirical covariance matrix as follows:

$$\tilde{\mathbf{S}}(\gamma) = (1-\gamma)\hat{\mathbf{S}} + \gamma\nu\mathbf{I} \tag{3.14}$$

where ν is the average of the eigenvalues of $\hat{\mathbf{S}}$, $\mathbf{I}$ is the identity matrix, and $\gamma \in [0,1]$ is a tuning parameter. The optimal tuning parameter used to be estimated via cross-validation, however, an analytical solution has been found recently. For more details on shrinkage LDA, see [130] and references therein.

3.3.4 Support vector machines

A support vector machine (SVM) is a widely used universal learning machine, which works based on the following principle: The classifier is defined by

$$y(x) = \text{sign}(\mathbf{w}^T\varphi(\mathbf{x}) + b), \tag{3.15}$$

where $\mathbf{w}$ is a weighting vector and φ is a possibly non-linear feature mapping. The use of the mapping φ, proposed by [225], extends the SVM to a non-linear technique in the following way. The input data is mapped to a higher-dimensional feature space, where a linear separating hyperplane is constructed. Note that this linear hyperplane is actually non-linear in the original space. The objective in the SVM formulation is to construct a separating hyperplane in the feature space with maximal margin. This can be translated to the following optimization problem:

$$\min_{\mathbf{w},e_i,b}\left(\frac{1}{2}\mathbf{w}^T\mathbf{w} + C\sum_{i=1}^{N} e_i\right), \tag{3.16}$$

subject to

$$y_i[\mathbf{w}^T\varphi(\mathbf{x}) + b] \geq 1 - e_i,\ e_i \geq 0,\ i = 1,...,N$$

where C is a regularization constant. By constructing the Lagrangian and taking the conditions for optimality, one obtains the dual problem, which is the following quadratic programming problem:

$$\max_{\alpha}(\sum_{i=1}^{N}\alpha_i - \frac{1}{2}\sum_{i=1}^{N}\sum_{j=1}^{N}\alpha_i\alpha_j y_i y_j K(\mathbf{x}_i,\mathbf{x}_j)), \tag{3.17}$$

subject to

$$\sum_{i=1}^{N}\alpha_i y_i = 0 \text{ and } 0 \le \alpha_i \le C \text{ for } i = 1,...,N,$$

where $\mathbf{x}_i \in \mathbb{R}^d$ and $K(\mathbf{x},\mathbf{x}_i)$ is a symmetric and positive definite kernel function satisfying the Mercer theorem, which is expressed as

$$K(\mathbf{x},\mathbf{x}_i) = \varphi(\mathbf{x})^T\varphi(\mathbf{x}_i) \tag{3.18}$$

Equation (3.18) is often called the kernel trick. It facilitates the use of high dimensional feature spaces without actually making explicit computations in this space. For detailed theoretical background behind the kernel trick we refer to [200].

The x_i input vectors corresponding to non-zero α_i values are called support vectors. The classifier in the dual space takes the form:

$$y(x) = \text{sign}[\sum_{i}\alpha_i y_i K(\mathbf{x},\mathbf{x}_i) + b] \tag{3.19}$$

Throughout this thesis we applied the least-squares support-vector machine introduced by [201]. In this formulation equality constraints are used instead of inequality constraints in (3.16):

$$\min_{\mathbf{w},e_i,b}(\frac{1}{2}\mathbf{w}^T\mathbf{w} + \gamma\sum_{i=1}^{N}e_i^2), \tag{3.20}$$

subject to

$$\hat{y}_i[\mathbf{w}^T\varphi(\mathbf{x}) + b] = 1 - e_i,$$

Taking the optimality conditions and eliminating $\mathbf{w}$ and $e = [e_1, ..., e_N]^T$ simplifies the computation to solving a set of linear equations instead of a quadratic programming problem:

$$\left[\begin{array}{c|c} 0 & y^T \\ \hline y & \Omega + \gamma^{-1} I \end{array}\right] \left[\begin{array}{c} b \\ \hline \alpha \end{array}\right] = \left[\begin{array}{c} 0 \\ \hline 1_N \end{array}\right] \tag{3.21}$$

with $y = [y_1, ..., y_N]^T$, $1_N = [1, ..., 1]^T$, $\alpha = [\alpha_1, ..., \alpha_N]^T$, $\Omega_{kl} = y_k y_l K(\mathbf{x}_k, \mathbf{x}_l)$.

3.3.5 Regularisation via nuclear norm penalty

So far we considered learning problems where the input data is represented as one-dimensional vectors consisting of d feature values. However, in a lot of practical problems the natural representation of the data extend along more dimensions. An image is inherently a matrix of pixel values. In neuroimaging, EEG and fMRI data contain multiple time series measured at different channels or voxels, respectively. Additional information might be conveyed by expanding the time series to frequency domain, thereby obtaining a $space \times time \times frequency$ tensor. Extra dimensions might be useful to organise the data collected from different patients/subjects or under different conditions. Traditional techniques handle such problems by vectorising the input data. However, recent studies [91, 202] show that matrix and tensor representation of signals reduce the small sample-size problem, facilitating a precise classification performance even for low number of training points and outperform traditional vector representation. Hence, for classification of an N^{th}-order tensor we consider the following model:

$$\begin{aligned} y(\mathcal{X}) &= sign(\hat{y}(\mathcal{A}, b)), \\ \hat{y}(\mathcal{A}, b) &= \langle \mathcal{A}, \mathcal{X} \rangle + b, \end{aligned} \tag{3.22}$$

where $\mathcal{X} \in \mathbb{R}^{I_1 \times I_2 \times \ldots I_N}$ is the input pattern, $\mathcal{A} \in \mathbb{R}^{I_1 \times I_2 \times \ldots I_N}$ is the classifier tensor of the same size, and b is a bias term or threshold. The classifier, namely the pair $(\mathcal{A}, b)$, is found by solving a non-smooth convex optimization problem using nuclear norm penalty:

$$\min_{\mathcal{A},b} F(\mathcal{A},b) = f(\mathcal{A},b) + \mu \sum_{n=1}^{N} \|\mathbf{A}_{(n)}\|_* \tag{3.23}$$

$$\tag{3.24}$$

where $\mu \geq 0$ is a tuning parameter and $f(\mathcal{A},b)$ is an appropriate loss function, e.g. quadratic error function. $\|\mathbf{A}_{(n)}\|_*$ is the nuclear norm of the n-mode matrix unfolding of the tensor $\mathcal{A}$ with singular values σ_i :

$$\|\mathbf{A}_{(n)}\|_* = \sum_i \sigma_i. \tag{3.25}$$

Nuclear norm regularisation has been used to devise convex relaxation for various rank-constrained matrix problems [25, 171] and for matrix classification [210]. Its extension for the case of higher order arrays in the above form was formulated by [187].

Regularization via nuclear norm favours a low rank solution; in our case this corresponds to a classifier matrix or tensor of low rank. In other words, the nuclear norm regularisation approach is beneficial if one can expect that the discriminative information lies in a low rank subspace. Such a situation arises, for example, when the EEG pattern of interest is simultaneously present on a number of channels. Then, the strength of the pattern on each channel, expressed along one mode and the EEG pattern itself, expressed along a second mode, define a rank-1 structure. This type of a-priori structural information is automatically conveyed by the nuclear norm penalty.

Chapter 4

Automated seizure detection

In section 2.4.2 we identified automated seizure detection as a key factor which can assist current clinical practice. First, a literature overview about existing automatic seizure detectors is given in section 4.1. Subsequently, we explore two alternative solutions. In section 4.2 the development and preliminary results of a universal, patient independent algorithm are presented. The conclusions of this study, published in [102], have motivated us to opt for a patient-specific seizure detection system. To this end, a novel approach exploiting spatial information from the multichannel EEG was proposed. The methodology and the results, published in [105], are discussed in 4.3. Finally, conclusions are drawn in section 4.4.

4.1 Literature overview

The first automatic seizure detection systems date back to the 1980s [79]. Since then, a large variety of seizure detection algorithms were developed. In general, these algorithms have two crucial design aspects: the identification and extraction of discriminative features from the EEG, and the training and application of a classifier. Note that these two steps are not independent from each other: different classification approaches may be optimal in case of different types of features. The most frequently used features include Fourier transform based or wavelet based measures to detect rhythmic patterns [4, 167, 160], autocorrelation [133], phase synchrony [220] or synchronisation likelihood [8] to capture the extensive, synchronous nature of seizure activity, furthermore, morphological or time-domain features such as amplitude, duration [79] or

Hjorth's parameters [92] extracted from the EEG waveforms. Recently, non-linear features, such as Lyapunov exponent [3] or information theoretic measures like entropy [113] have also been proposed. The extracted features can be classified using simple thresholding methods or rule based systems [55], linear classifiers [76], support vector machines [74, 199], Bayesian classifiers [176], k-nearest neighbour classifiers [169], mixture of expert models [198], adaptive neuro-fuzzy systems, [86], just to mention the best known solutions. For an extensive literature overview, we refer to [215].

Despite the abundance of published seizure detection algorithms in the last few decades, most centres do not apply these automatic techniques in clinical practice today [93, 114]. The variety of artefacts contaminating EEG recordings can obscure the seizure pattern degrading sensitivity, or, repetitive rhythmic artefact patterns can cause false detections. Recent advances in statistical blind source separation methods allow the removal of artefacts without deteriorating the EEG patterns of interest, thereby, improving seizure detection performance [51].

Below we explore the utility of a universal, patient independent seizure detection algorithm. Inspired by a successful neonatal seizure detection technique presented in [55], the proposed algorithm aims at mimicking the visual interpretation process of the expert EEG reader.

4.2 Mimicking the human observer

4.2.1 Introduction

The seizure detection algorithm presented here is a rule based expert system. It considers the visually appearing characteristics, on which neurologists also rely when reading EEG data. The main steps of the algorithm reformulate these characteristics as mathematical features. Further actions taken or decisions are made based on simple if-then rules. The results of detection can be compromised by artefacts contaminating the seizure pattern or causing false detections. It will be shown how to overcome the difficulties posed by different artefacts, with special attention to muscle artefact removal.

4.2.2 Materials and methods

EEG data

The seizure detection algorithm was developed based on an EEG dataset containing surface recordings from 22 different patients with refractory focal epilepsy, who underwent presurgical evaluation. In total 32 seizures were recorded. The average duration of the recordings was 4.9 hours, resulting in a total of 108 hours EEG data.

Seizure detection algorithm

There are well defined characteristics of the EEG, on which the neurologist relies when determining whether the segment of the EEG recording under investigation contains seizure activity or not. As described in section 2.3.1, a typical focal seizure contains evolving, repetitive sharp waves. The evolution might be observed in frequency, amplitude, topography and morphology. These visual characteristics can be reformulated as mathematical features and will serve as the consecutive steps of the seizure detection algorithm. The outline of the algorithm is depicted in Figure 4.1.

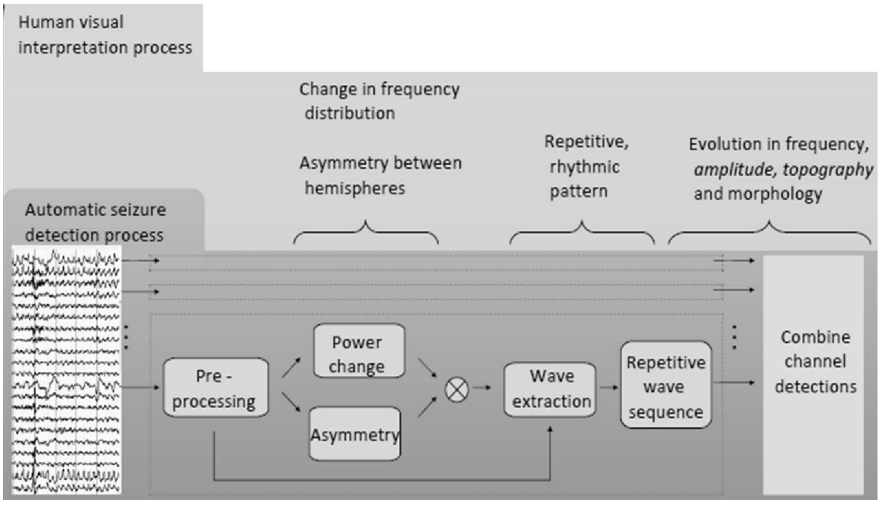

Figure 4.1: The human visual interpretation of EEG relies on various peculiar charactertistics of the ictal pattern. These characteristics are translated into mathematical features in the proposed algorithm.

Preprocessing. The EEG data are broken down into 5s long single channel epochs. Subsequently, muscle artefacts were removed using the BSS-CCA method (see below). Each epoch is band pass filtered between 2-25Hz. For further analysis, the average referenced preprocessed epochs of single channels are used.

Energy and asymmetry. In this work we are focusing on the detection of the seizure as early as possible. The foremost peculiarities of the seizure onset are the change in signal energy distribution on a certain group of channels, associated to the primarily affected brain regions. The energy and asymmetry characteristics of the signal are investigated for four distinct frequency bands denoted by $f^{(i)}$, with lower and upper frequency limits $f^{(i)}_{min}$ and $f^{(i)}_{max}$: delta (2-4Hz), theta (4-8Hz), alpha (8-13Hz) and beta (13-25Hz). The feature expressing the signal energy is computed as the ratio between the power spectral density (PSD) in the current channel epoch and frequency band ($PSD_{\phi,ch}$) and the PSD of the same band in the background EEG ($PSD^{bgr}_{\phi,ch}$). PSD is computed according to Welch's method; background is defined as the 30s long recording preceding the current epoch:

$$PowRate(ch, f^{(i)}) = \frac{\sum_{\phi=f^{(i)}_{min}}^{f^{(i)}_{max}} PSD_{\phi,ch}}{\sum_{\phi=f^{(i)}_{min}}^{f^{(i)}_{max}} PSD^{bgr}_{\phi,ch}} \tag{4.1}$$

To exploit topographic information of the EEG pattern, brain symmetry index (BSI) is a useful measure. BSI was introduced to quantify the asymmetry in spectral power between the two hemispheres [221]. Here we modified the pairwise BSI defined in [184] to measure channel symmetry index (CSI) - the power asymmetry in the predefined bands between contralateral channels pairs:

$$CSI(ch, f^{(i)}) = \sum_{\phi=f^{(i)}_{min}}^{f^{(i)}_{max}} \frac{PSD_{\phi,ch} - PSD_{\phi,opp}}{PSD_{\phi,ch} + PSD_{\phi,opp}} \tag{4.2}$$

where $PSD_{\phi,ch}$ and $PSD_{\phi,opp}$ are the power spectral density of the actual channel and the contralateral channel, respectively. This formula points out which member of the channel pair exerts higher power in the current frequency band. Its value can vary between -1 and 1, a positive value meaning that channel *ch* exerts more power, a negative value meaning that the contralateral channel does.

In case of a focal or hemispheric seizure, a significant asymmetry can be observed between channel pairs. However, the asymmetry between the hemispheres are less expressed in case of a generalized seizure. According to our observations the energy change of the signal is more significant in such a case. Consequently, the energy and asymmetry information of the actual epoch is combined into one parameter for threshold classification:

$$CSI(ch, f^{(i)}) \times (PowRate(ch, f^{(i)}) - 1) > T_1 \tag{4.3}$$

The value of the combined parameter becomes negative if either the channel is non-dominant with respect to its pair, or if it exerts lower power than the background. A positive threshold T_1 will certainly reject such segments, beside other segments with relatively low asymmetry (CSI) and energy change ($PowRate$). The threshold value is empirically set to 0.6. The frequency band $f^{(i)}$, for which the actual epoch is larger than the threshold, is kept in the memory for the following step, and will be referred to as the determinative band of the epoch.

Wave extraction. The epochs selected as seizure candidates in the previous step are now broken down into consecutive wave segments. A similar procedure was used in [79]. Waves are defined as signal segments limited by the minimum amplitude samples found between adjacent zero-crossings of the oscillatory signal. The waves obtained this way might have a large variability in duration for a noisy channel. Waves originating from irrelevant brain activity, artefacts or noise should be rejected. Only those waves are kept for further analysis, which correspond in duration to the determinative frequency band of the epoch, assigned according to (4.3).

Evolving repetitive wave sequence. As a first step each wave is compared to a spike template taken from a typical ictal activity pattern by visual inspection. If the summed mean square error of all the waves in the current epoch is sufficiently small, the algorithm proceeds and searches for a wave sequence evolving in amplitude. A new wave is added to the existing sequence if its amplitude is at least 90% of the amplitude of the preceding wave, and the mean amplitude of the total wave sequence does not decrease. The resulting sequence might not contain consecutive waves any more, as the algorithm skips segments of data affected by noise or containing background activity of adjacent epileptic spikes.

Topographic test. As a final step the information of different channels is integrated. A detection is approved if evolving repetitive waves were found on at least two neighbouring channels, or on a single channel with sufficiently

different signal pattern compared to all the other channels. Such patterns are combined into one seizure candidate segment. The latter property is computed with a global channel-wise symmetry index, a measure similar to CSI, but where the spectral power of the actual channel is compared to all the other channels of the EEG:

$$GCSI_{ch,f^{(i)}} = \sum_{CH \neq ch} \sum_{\phi=f_{min}^{(i)}}^{f_{max}^{(i)}} \frac{PSD_{\phi,ch} - PSD_{\phi,CH}}{PSD_{\phi,ch} + PSD_{\phi,CH}} \tag{4.4}$$

After combining channel information the duration of the pattern selected as seizure candidate should exceed a certain threshold length T_2 for final approval. In this work T_2 values between 5 and 10 s were tested.

Correction for artefacts

Observing the EEG datasets, four types of artefacts were identified which were contaminating the measurements: muscle artefacts, repetitive eye movements, alpha activity and chewing artefacts.

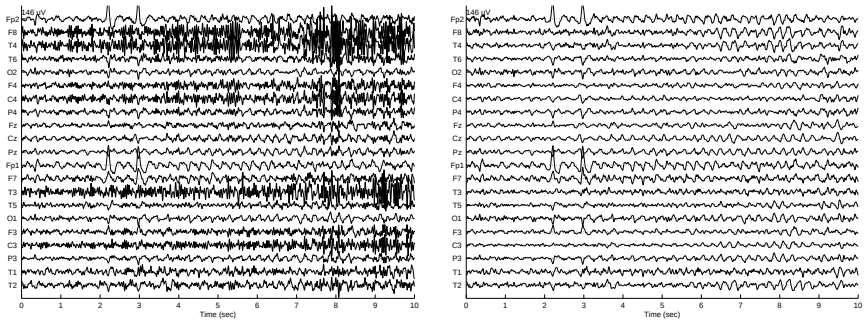

Figure 4.2: Ictal EEG of a patient with temporal lobe epilepsy. Muscle artefacts are contaminating temporal and fronto-central channels, making both visual and automatic detection difficult. BSS-CCA succeeds in removing muscle artefact and revealing the hidden rhythmic pattern

Muscle artefact removal. On one hand, muscle artefact can cause missed or late detections, when superimposed on ictal activity. On the other hand, low pass filtering of muscle activity can result in a regular pattern in beta band, which can be mistaken for an ictal pattern. Muscle artefacts were removed prior

to filtering by a technique based on canonical correlation analysis (BSS-CCA) as introduced in [40]. The multichannel EEG signal is decomposed to mutually uncorrelated sources with different autocorrelation structures, and ordered by their autocorrelation coefficients. Muscle activity, having broad frequency spectrum, is expected to appear on the sources with lower autocorrelation. Components containing muscle activity pattern are selected by comparing the energy exerted by 3-15 Hz frequency band, containing real brain activity and by 25-50Hz frequency band, affected mostly by muscle activity:

$$EnergyRate = \frac{E(3-15Hz)}{E(25-50Hz)} \tag{4.5}$$

The first component with an energy rate smaller than a certain threshold (set to 1.5 in this work) is excluded, together with all other components with lower autocorrelation. The clean signal is reconstructed by the remaining source signals. Fig. 4.2 illustrates how BSS-CCA succeeds in removing muscle artefacts from an EEG segment with ictal activity.

Eye artefacts. On average referenced montage the eye artefacts can be projected on multiple channels. Therefore, repetitive eye blinks can be mistaken for a seizure pattern. Correction for these artefacts was included in the wave extraction step. A spike was considered to be an eye artefact and was automatically rejected, if its amplitude was higher than 80 uV and appeared either on channel Fp1 or Fp2. Spikes were also rejected in case they appeared on a different channel but simultaneously with an already detected eye artefact, and their waveform showed a high correlation with it.

Alpha activity. Alpha activity is a rhythmic 8-13Hz pattern on the occipital channels, occurring when the patient is in a relaxed, awake state. It can be misleading because of its regular pattern. It is unlikely to occur simultaneously with a seizure, therefore, segments with strong alpha band activity centred occipitally can be simply discarded.

Chewing artefact. While eating, the movements of the tongue, the skin and the chewing muscles create semi-rhythmic artefacts on the EEG data. The pattern of this artefact is characterized by high voltage spikes occurring regularly after each other, superimposed by muscle artefacts. Due to the high voltage, the patterns occurring on different channels are closely correlated. Such segments with highly correlated signal pattern should be discarded.

Evaluation criteria

The performance of the seizure detection algorithm is evaluated in terms of sensitivity, false detection rate and alarm delay, defined as follows:

1. Sensitivity: percentage of the detected seizures compared to the total number of recorded seizures
2. False detection rate: number of false detections divided by the total time of the measurement
3. Alarm delay: time elapsed between the seizure onset according to the labeling and the moment the detection system is setting off the alarm

4.2.3 Results

There is a trade-off between sensitivity and false detection rate. The performance of the algorithm can be easily tuned in favour of one or the other by adjusting the threshold length. Increasing the threshold length T_2 will exclude false detections with short patterns resembling ictal periods, although, it will also cause missing true seizures which (a) are too short (b) are partially superimposed with artefacts or (c) which the algorithm fails to recognize in their entire course. In this work the threshold length varied between 5s and 10s.

Table 4.1 shows the performance of the algorithm with and without applying BSS-CCA for muscle artefact removal, yet, without the final step of topographic test. The sensitivity increases significantly after muscle artefact removal, by an average of 9.85%, depending on the threshold length.

On the other hand, the number of false detections increases as well. This can be explained by the fact that removing the least autocorrelated CCA sources, the autocorrelated, thus seizure-like oscillatory components become more pronounced on the data. These non-seizure segments are usually detected on non-consistent or single channels, therefore, the topographic test efficiently excludes them. The final results are shown in Table 4.2. Due to application of the final topographic test, one extra seizure was missed. However, decreasing the threshold length from 8s to 7s a higher sensitivity (84.4%) can be obtained, still preserving a comparable false detection rate (0.24/h). The remaining false detections are mainly due to interictal epileptiform activity, or rhythmic, low-frequency activity of sleeping and drowsiness. Our method has an inherent lag between seizure onset and alarm set-off because of the 5s long epoch segments analysed at once, and because of the applied threshold T_2 on the minimum

Table 4.1: Removal of muscle artefacts improves detection performance

BEFORE

threshold length (s)	5	6	7	8	9	10
sensitivity (%)	81.3	78.1	71.9	71.9	71.9	68.8
false detection rate (/h)	2.13	0.90	0.48	0.30	0.24	0.17

AFTER

threshold length (s)	5	6	7	8	9	10
sensitivity (%)	90.6	90.6	87.5	78.1	78.1	78.1
false detection rate (/h)	1.77	0.90	0.53	0.36	0.26	0.23

Table 4.2: The topographic test successfully reduces the amount of false detections

threshold length (s)	5	6	7	8	9	10
sensitivity (%)	87.5	87.5	84.4	75.0	75.0	75.0
false detection rate (/h)	0.62	0.40	0.24	0.20	0.18	0.15
alarm delay (s)	14	15	16	18	19	19

seizure length. Thus, a lower threshold length is also beneficial for a shorter alarm delay.

4.2.4 Discussion

The seizure detection algorithm presented here successfully detected epileptic seizures. However, the algorithm uses a few parameters (e.g. the combined threshold T_1 in step 2 or the spike template in step 4), which are not yet derived in a patient independent way but are optimised based on the currently available EEG data. Therefore, the algorithm should be evaluated using an independent EEG dataset in order to obtain realistic performance estimates.

In fact, the large inter-patient variability regarding seizure characteristics poses a great challenge in developing a patient independent seizure detector. The advantage of such universal systems is that they are immediately ready to be used for any new patient. However, the seizure onset pattern of a specific patient can very much resemble the background activity pattern of another [166]. Therefore, universal seizure detectors often give false alarms. Note that a low false alarm rate is a crucial requirement when used as a warning device. Although the final topographic test of the presented algorithm successfully

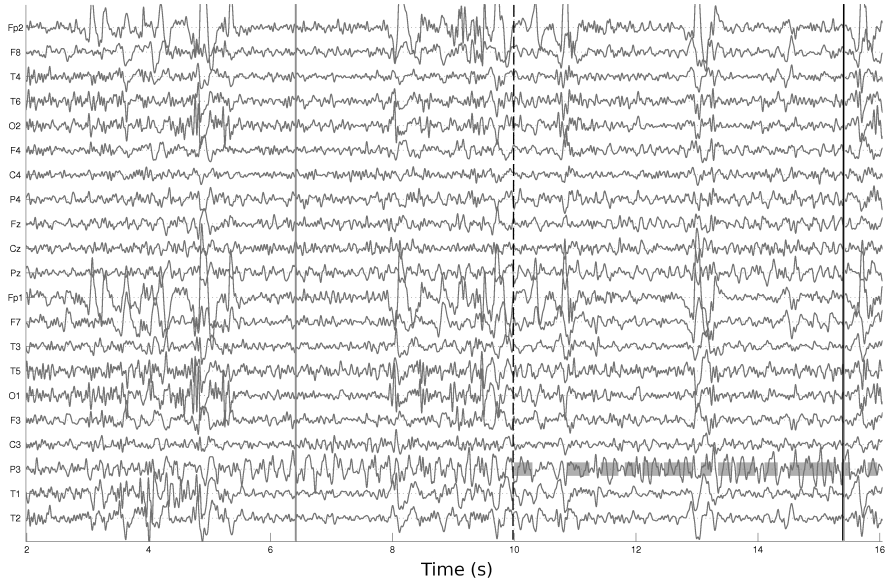

Figure 4.3: Example of a successfully detected seizure. The gray line depicts the seizure onset time according to the labelling, the black dashed line indicates the onset time found by the algorithm and the full black line corresponds to the alarm time. The highlighted signal segments correspond to the wave sequence identified by the algorithm as seizure activity.

eliminated many false detections, the false alarm rate remains too high for use in clinical practice.

Alternatively, patient-specific seizure detectors can yield improved performance, both regarding specificity and sensitivity. A patient-specific approach is most appropriate in case of unifocal epilepsy patients, due to the rather consistent intra-patient seizures regarding both temporal pattern and localisation. Motivated by the success of the topographic test and the asymmetry measure, our goal is to develop a method which automatically incorporates multichannel EEG information.

The disadvantage of a patient-specific system is that it needs to be trained every time before applying it to a new patient. A crucial design challenge in this case is to reduce the number of seizures needed to train the classifier. The proposed methodology, presented below, addresses this issue as well.

4.3 Incorporating structural information via nuclear norm learning

In this section a patient-specific seizure detection algorithm is presented. As the spatial distribution of the ictal pattern is characteristic for a patient's seizures, this work aims at incorporating such information into the data representation and applies a learning algorithm capable of exploiting it. More specifically, the nuclear norm regularization is used to convey structural information of the channel-feature matrices extracted from the EEG. This method is compared to two existing approaches utilizing the same feature set, but integrating the multichannel information in a different manner.

4.3.1 Introduction

Several existing seizure detection algorithms act on single channel data [168, 233]. Methods attempting to integrate multichannel information include two-step systems, where, in the first step a decision is made for each channel by a separate classifier, and in the second step the outputs of these classifiers serve as the input of a combined, final decision procedure, e.g. [169]. Such a late integration method was compared to an early integration method, where the features extracted from each channel are sorted and stacked into a long feature vector, which is then used to train a single classifier. The early integration method was shown to be superior in performance, by preserving the synchronously recorded nature of the EEG and exploiting the inherent inter-relationship of the channels [83]. A patient-specific seizure detector was developed by [186], which relies on features describing the temporal evolution, the spectral and the spatial structure of the EEG. In order to capture spatial information, the features of each channel are concatenated to form one feature vector. As opposed to the former study, where the sorting operation was intended to remove spatial information, the goal of the stacking in this case is to drive the attention to the locations corresponding to the channels consistently showing seizure activity.

Here we investigate a novel solution based on the following considerations. The features extracted from the multichannel EEG are represented in the form of a matrix which serves as an input to a classifier. A similar arrangement has been successfully applied in [2]. The matrix representation of the data helps preserving and exploiting the inherent spatial structure of the multichannel EEG data. Moreover, as explained in Chapter 3 exploiting structural information from the matrix representation of signals can reduce

the small sample-size problem. Therefore, we expect a good seizure detection performance even for low number of training seizures.

4.3.2 Materials and Methods

Fig. 4.4 depicts the consecutive steps of the entire procedure involved in training and testing the seizure detectors. The following sections describe each step in detail.

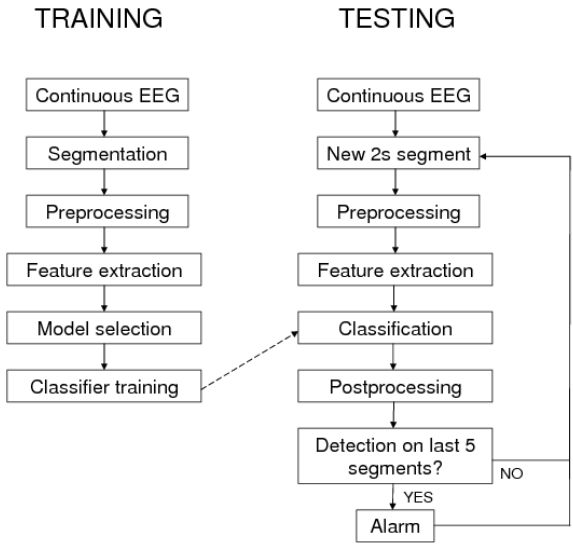

Figure 4.4: Operational structure of the classifier training and the testing of the seizure detector.

Training and testing EEG data

The seizure detectors were evaluated using the CHB-MIT database, which includes the scalp EEG recordings of 23 pediatric patients, and is available online at PhysioNet (`http://physionet.org/physiobank/database/chbmit`, [77]). All patients of the dataset were included in our study except for one, in case of which the entire electrode montage was altered during the recordings.

Some channels within the montage were changed during the recordings in case of a few other patients as well. In these cases 18 channels were considered, which remained unchanged throughout the whole duration of the recording. In the rest of the patients, all 23 channels of the electrode montage was used. Our dataset, therefore, consists of the scalp recordings of 22 patients. A second dataset was recorded 1.5 years after the first recording of patient 1. This recording was handled separately, resulting in 23 distinct datasets. A total of 131 seizures were recorded during 892 hours of monitoring. The data were sampled at 256Hz and a bipolar electrode montage was used. Detailed description of the dataset can be found online (see the link above).

In order to assess the capabilities of the seizure detectors trained with different amount of seizure information, several experiments were performed. Mutually non-overlapping training and testing datasets were created in each experiment for each patient in the following way. The seizures of each patient were ordered according to the times of their onset. In each experiment, seizures which occurred earlier in time were included in the training set, and the rest of the seizures were added to the test set. For instance, if four seizures were recorded from a patient, three experiments were performed. In the first experiment one seizure was included in the training, and three in the test; in the second experiment two seizures were included in the training and two in the test; finally, in the third experiment three seizures were included in the training and one in the test. Maximum five experiments were performed per patient, even if the number of recorded seizures would have allowed larger training sets.

Non-seizure examples for the training set were selected from the EEG recorded over a twenty-four hour period, as this period covers the different brain functioning states connected to sleep and other activity levels affecting EEG [169]. In order to limit the computational costs, but at the same time cover as many different EEG patterns as possible, one minute long segments recorded every fifteen minutes were included for the training.

The seizure detectors were tested on continuous EEG data recorded after the twenty-four hour period used for constructing the training set. All available seizure data, which were not included in the training were added to the test dataset, resulting in a total of 474 hours of test data, on average 21.56 hours per patient, ranging from 1.13 to 125.94 hours.

Preprocessing and feature extraction

Seizures often involve involuntary movements and muscle contractions, which contaminate EEG data seriously and hinder interpretation. Muscle artefacts were automatically removed applying BSS-CCA as done in the previous seizure

detection approach. Afterwards, each EEG channel was band-pass filtered between 1-30 Hz. The signals were segmented into 2s long non-overlapping epochs and a total of sixteen features were extracted from each channel of each epoch. The extracted features, listed in Table 4.3, are well established and widely used in the literature, not only for adult scalp EEG [142, 144, 169], but also for intracranial recordings [209] or neonatal seizure detection [204]. The definition and computation of the features are described in Appendix A.3. The feature set corresponding to one epoch (a total of 16 times 23 or 18 features) will be referred to as a "datapoint" throughout this chapter.

Integration of multichannel information

A distinct feature set is extracted from each EEG channel, however, the multichannel information has to be integrated in one global decision in each epoch. We compared three different integration approaches. The first two are described and studied in detail in [83], the third one is a novel approach we propose and evaluate in this study. The different integration approaches result in different data representations, and require different learning and classification schemes. The various stages of the three algorithms are depicted in Figure 4.5, and are explained in detail below.

Table 4.3: Extracted Features

Time domain features	1-3. number of zero crossings (#0), maxima (#max) and minima (#min); 4. skewness (skew); 5. kurtosis (kurt); 6. root mean square amplitude (rmsa)
Frequency domain features	7. total power (TP); 8. peak frequency (PF); 9-16. mean and normalized power in frequency bands: delta: 1-3 Hz (D, nD) theta: 4-8 Hz (T, nT) alpha: 9-13 Hz (A, nA) beta: 14-20 Hz (B, nB)

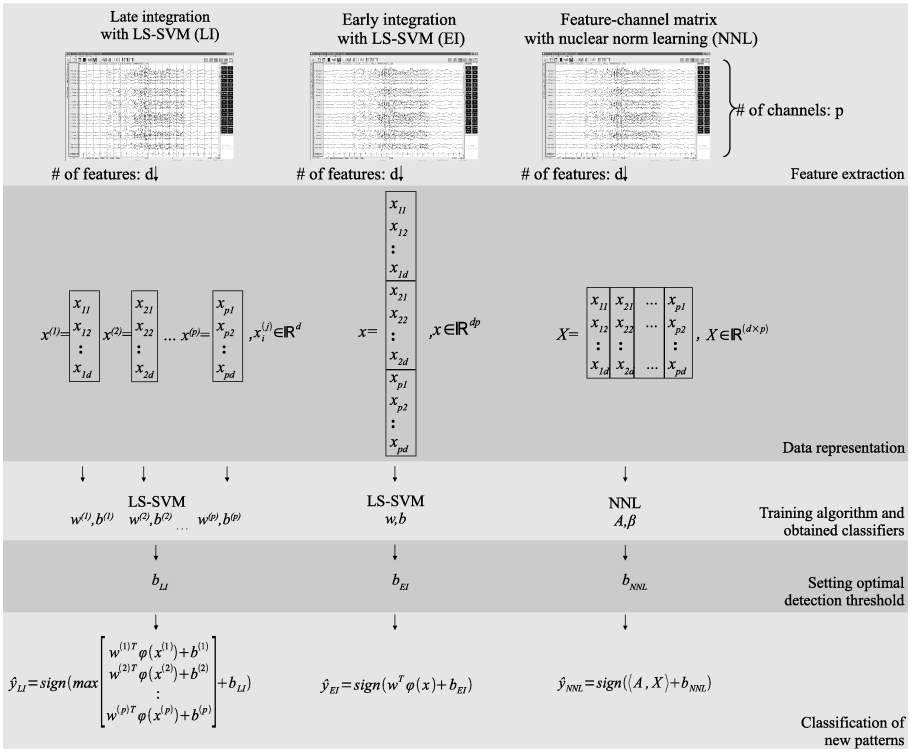

Figure 4.5: Diagram depicting the various steps of the different seizure detection approaches

Early and late integration with least-squares support vector machines (LS-SVM)

Late integration (LI). Traditional seizure detection systems classify the feature set of each channel separately, and then combine the channel outcomes in an independent step. There are several different strategies that can be followed. The outputs of the channel classifiers can be binary or probabilistic. Post-processing can be performed applying a moving average filter on the outputs from the consecutive epochs [205]. A channel detection might automatically induce an alarm [55]; or the channel outputs can be integrated via mean, max, min score, or majority vote [83]. The number of channels contributing to the global score might as well be limited [176], or weighted, this way including prior spatial information. The final classifier output may be converted to posterior probabilities using a sigmoid function [204]. In the

current study p number of LS-SVM classifiers are trained, where p corresponds to the number of EEG channels. During monitoring the feature sets of each channel are classified independently. The continuous outputs of the single channel classifiers are integrated by taking their maximum. The final decision is made by comparing the integrated output to the detection threshold b_{LI}. The choice of the detection threshold is explained below in 4.3.2.

Early integration (EI). In this approach the feature vectors extracted from each EEG channel are stacked into one long feature vector of length $p \cdot d$, where p is the number of channels and d is the number of extracted features. As explained above, stacking the channel vectors ensures that the synchronously recorded and inter-dependent nature of multichannel EEG is preserved in the input patterns, and therefore exploited in the learning procedure. Furthermore, the channels are concatenated in the same order for all epochs (as opposed to the sorting approach in [83]), aiming at including spatial information characteristic of the patient's seizures. The stacked feature vectors are used to train one global LS-SVM classifier. During monitoring the feature set of each new epoch is processed by the global classifier and the continuous outputs are compared to the detection threshold b_{EI} in order to obtain the final decision.

Model selection for LS-SVM In the LS-SVM case, all the support vectors are non-zero, consequently, the model is based on the whole input dataset - which can be beneficial in the current application due to the small training set size. For the same reason, and due to the relatively high dimensionality of the input data, a linear kernel was applied. However, as RBF kernel is often used for seizure detection, e.g. [204, 186], it has also been tested.The LS-SVMlab v1.8 toolbox implementation (www.esat.kuleuven.be/sista/lssvmlab, [38]) was used in this study, which performs automatic model selection, namely determining the tuning parameters by coupled simulated annealing [232]. As an optimization criterion five-fold crossvalidated misclassification error was used.

Feature-channel matrix with nuclear norm learning (NNL)

Feature-channel matrix. This study presents a novel approach, where the features extracted from each epoch are preserved in their original arrangement, in the form of a matrix of size $d \times p$, where d is the number of features and p is the number of channels. Each row of the matrix contains the feature set extracted from the corresponding channel. There is a large variability between the seizure patterns of different patients. However, synchronization between EEG channels is a generally occurring characteristic [226]. Synchronization may be observed on a few channels in case of a partial seizure, or on a larger scale given a generalized seizure. Similar EEG pattern, therefore, similar feature values will

be present on those channels and in the rows of the matrix corresponding those channels, which are involved in the seizure. Representing the data in matrix form allows to exploit the common information among the channels. Channels not involved in the seizure might show various patterns of background activity, not distinguishable from patterns of normal brain state. Thus, one can assume that the channels involved in the seizure and the features most descriptive about the seizure pattern will have the best discriminative power.

Convex optimization with nuclear norm penalty. For classification of the feature-channel matrix extracted from an EEG epoch X, we apply the nuclear norm regularisation approach presented in section 3.3.5:

$$\hat{y}(\mathbf{A}, \beta) = \langle \mathbf{A}, \mathbf{X} \rangle + \beta, \tag{4.6}$$

$$\langle \mathbf{A}, \mathbf{X} \rangle = \sum_{i,j} a_{i,j} x_{i,j}$$

where $\mathbf{X} \in \mathbb{R}^{d \times p}$ is the input pattern, $\mathbf{A} \in \mathbb{R}^{d \times p}$ is the classifier matrix of the same size, and b is a bias term or threshold. Decisions are made according to $\text{sign}(\hat{y}) \in \{-1, 1\}$, where 1 and -1 correspond to seizure and non-seizure epoch, respectively. Here, as the input patterns are matrices and not tensors, the optimization problem in (3.23) is slightly simplified:

$$\min_{\mathbf{A}, \beta} F(\mathbf{A}, \beta) = f(\mathbf{A}, \beta) + \mu \|\mathbf{A}\|_*, \tag{4.7}$$

$$f(\mathbf{A}, \beta) = \sum_{k=1}^{N} (\hat{y_k}(\mathbf{A}, \beta) - y_k)^2, \tag{4.8}$$

where $f(A, \beta)$ is the quadratic error function accounting for the misclassification. The choice of a quadratic error function was made specifically because the same loss function is used in LS-SVM classification. Model selection, namely the selection of the μ was done according to the five-fold cross-validation of the misclassification error, similarly to the model selection of LS-SVM. The consecutive steps of the nuclear norm learning approach are summarised in Appendix A.2. The algorithm solving (4.7) can be implemented in `CVX` [82], as given in Appendix A.1.

Optimal detection threshold

Seizures are rare events, consequently, there is a large amount of non-seizure data available for training compared to seizure data. Classification problems with skewed class sizes are called unbalanced problems and need special attention. The Bayesian formulation used by [176] inherently incorporates seizure and non-seizure class probabilities. This issue is bypassed in [74] by reformulating the classification problem as a novelty detection problem, applying a one-class support vector machine (SVM). Alternatively, [154] applied support vector data description (SVDD), which can make use of ictal data as well, yielding better detection performance. Traditional SVM approaches addressing the same problem also exist. In the work of [204] the classifier outputs are converted to posterior probabilities using a sigmoid function. This technique is proven to perform significantly better than applying a threshold on the original outputs [166].

Alternatively, in this work a bias term correction [200] is used, by adjusting the model thresholds b_{LI}, b_{EI} and b_{NNL} in order to achieve optimal classification performance. Due to the small amount of available seizure data, the detection threshold was set using the training dataset, similarly to [139]. In this work we used misclassification error as optimality criterion. First, the classification outputs obtained for the training samples were collected. From this discrete set, the value minimizing the number of falsely classified training datapoints was selected and assigned as detection threshold.

Evaluation measures

The receiver operating characteristic (ROC) curve reflects the discriminative power of a classifier by depicting its sensitivity versus its specificity for every possible threshold value. A good classifier has high sensitivity along with high specificity, resulting in a large area under the ROC curve (AUC).

In order to characterize the performance of the classifiers applied in a seizure alarm system, the outputs obtained for the individual epochs have to be postprocessed and converted to alarms. The outputs were first converted to $\{0,1\}$ values with a signum function. A detection was made, if a value 1 was obtained this way for at least five consecutive epochs. Detections occurring less than 30 seconds after each other were grouped together and one single alarm was set off.

The following event-based measures are used to evaluate the performances of the detectors:

1. Detection sensitivity

$$dS = \frac{\text{number of detected seizures}}{\text{total number of seizures}}$$

2. False alarm rate

$$R_{fa} = \frac{\text{number of false alarms}}{\text{duration of the EEG}}$$

3. Alarm delay

$$D = \text{time of alarm setoff} - \text{time of seizure onset}$$

4. Quality value

$$QV = \frac{1}{(R_{fa} + 0.2) \times (dS \times D + (1 - dS) \times 60)}$$

The quality value was introduced by [169] in order to compare different seizure detectors based on one measure reflecting all the three above enumerated aspects of the performance. Sensitivity and alarm delay are taken into account by creating a weighted average alarm delay. When the weighted average alarm delay or the false detection rate decreases, the quality value increases. Thus, the detector with the highest quality value is the best one. Note that in the above formula R_{fa} is measured in units of $1/h$, while dS is measured in seconds.

4.3.3 Results

Figure 4.7a, depicting the classifier obtained for Patient 1, illustrates the nature of the structural information conveyed by nuclear norm regularization and its physiological meaning. The 16 columns correspond to the different features extracted from the 23 channels, which constitute the rows of the matrix. The classifier is well approximated by a matrix of rank 1, the first singular value carries 97.6% of the total energy (see Figure 4.7b). The values of the left and right singular vectors represent the relative discriminative power of the channels and features, respectively. Note that the highest channel entries (electrodes over the right temporal and parietal area), and highest feature entry (normalized power in the theta band) characterize well the seizure pattern and localization as observed on Figure 4.6. Nuclear norm regularization induced a solution where the feature entries follow a similar pattern in each channel involved in the seizure, in agreement with the considerations in 4.3.2.

In comparison, the classifier matrix obtained by EI (Figure 4.7c) is less structured. Its singular values decay slower, the first singular value carrying 47.6% of the total energy. There are more channel and feature entries present with high values, and the feature patterns observed on the channels are diverse. This intuitively means that more EEG pattern details are considered in the classifier. Subtle characteristics of the training seizures might not be present in other seizures. This leads to overfitting and decreased predictive performance. While it separates better the training data than NNL does(EI: AUC=0.9991 and NNL: AUC=0.9966), EI performs worse on the testing data (EI: AUC=0.9616 and NNL: AUC=0.9718).

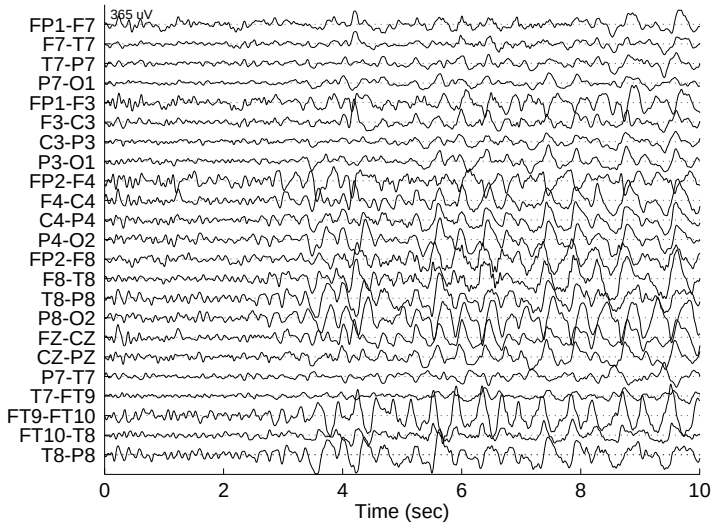

Figure 4.6: First training seizure of Patient 1.

The degree of structure in the classifier is controlled by the regularization parameter μ. This parameter is optimized for predictive performance in the crossvalidation. Hence, if a low-rank solution is not favourable, a low μ value would be set and the quadratic error function would dominate the expression in (4.7). In such cases the classifier would not be enforced to be approximately low rank. Nevertheless, in the majority (20 out of 23) of the cases the NNL approach results in more structured classifiers than the EI approach (Figure 4.8).

The overall performance of NNL, EI and LI detection approaches are compared in Table 4.4. Median and mean (in brackets) values of sensitivity, false detection rate and alarm delay were computed for the test data of the whole patient population. The false detection rate of NNL approach is three times lower

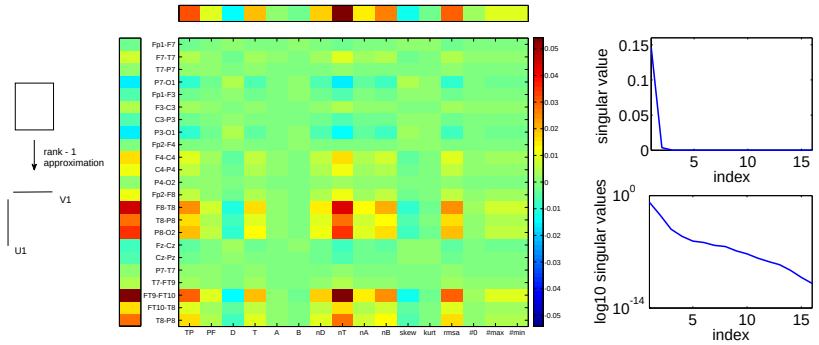

(a) NNL (b) NNL

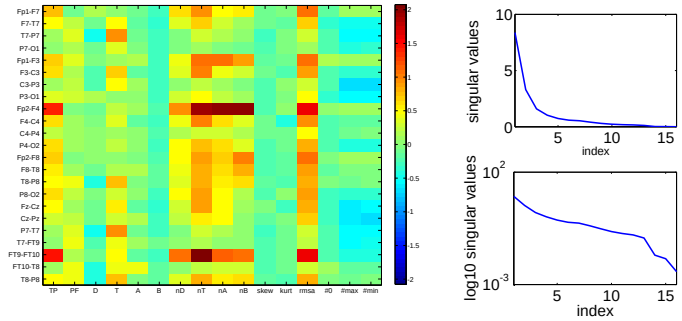

(c) EI (d) EI

Figure 4.7: Classifier matrices (a, c) and their singular values (b, d) obtained by training with the first seizure of patient 1, using the NNL and EI approaches, respectively. (a) also shows the left and right singular vectors. It is visually observed that outer product of the singular vectors closely approximates the classifier matrix. (b) shows fast decaying singular values: the first singular value carries 97.6% of the total energy, indicating an approximately rank-1 structure. The values of the left and right singular vectors represent the relative discriminative power of the channels and features, respectively. Note that the highest channel entries (electrodes over the right temporal and parietal area), and highest feature entry (normalized power in the theta band) characterize well the seizure pattern on 4.6. In comparison, the classifier matrix (c) obtained by EI is less structured. Its singular values decay slower, the first singular value carries 47.6% of the total energy.

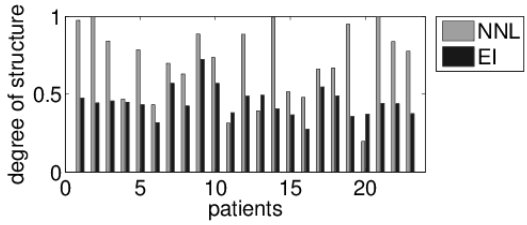

Figure 4.8: The bar plot compares the degree of structure in the classifiers obtained by NNL and EI. The degree of structure is expressed as percentage of energy carried by the first singular value of the classifier matrix. In 20 out of 23 cases the NNL approach results in more structured classifier.

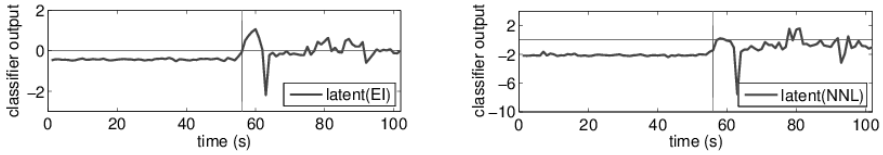

Figure 4.9: Classifier outputs obtained by the EI approach (a) and the NNL approach (b) for the first test seizure of Patient 8. The vertical line indicates the onset of the seizure according to the labelling of an expert. This is one of the few examples where a seizure was missed by the NNL but detected by the EI approach. The output time courses of both classifiers follow a similar pattern, indicating comparable discriminative power. The seizure is missed by NNL due to the relatively high detection threshold.

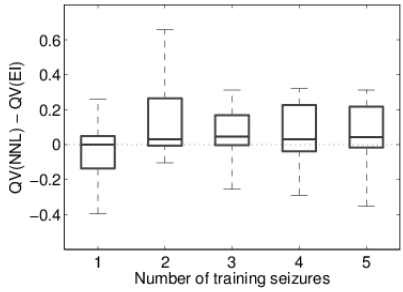

Figure 4.10: Boxplot depicting the patient-by-patient differences of NNL and EI-LSSVM performance in terms of quality value, evaluated based on the test data, given different number of training seizures

than the EI approach, and its sensitivity and alarm delay is just slightly worse. The false detection rate of the LI approach lies between the one of NNL and EI. At the same time its sensitivity is lower than both other approaches, despite the fact that the OR function integrating the channel decisions facilitates the highest possible sensitivity.

It is worth to observe how the performance on the test data evolves due to additional training seizures. The detection sensitivity increases in all cases, nevertheless, at the cost of a higher false alarm rate. It is important to note, though, that while the mean false alarm rates of the EI and LI approaches exceed 0.5/h — a value not acceptable in clinical applications [169] — the false alarm rate of NNL approach always remains below.

The inevitable trade-off between sensitivity and specificity explains why some seizures were missed by the NNL and not by the EI approach. Figure 4.9 shows the classifier outputs obtained by the EI and NNL approach during the first seizure of Patient 8. The output time courses of both classifiers follow a similar pattern, indicating comparable discriminative power. However, the seizure was missed by the NNL, due to the relatively high detection threshold compared to the one of the EI approach. The detection threshold was set according to the training data, and is only an estimation of the optimal threshold. Observing the classifier outputs of Patient 8, this detection threshold could be decreased, facilitating better sensitivity, but still preserving high specificity.

Due to the ambiguous results regarding the comparison of sensitivity and false detection rate of the NNL and EI approaches, a measure reflecting to both aspects is needed. Therefore, the quality value introduced by [169] was applied to the results of each patient. The boxplot in Figure 4.10 shows the distribution of the test performance differences between the NNL and EI over the individual patients.

Wilcoxon signed rank tests were performed investigating whether any approach provides a significant improvement in the median quality value with respect to the other approaches. The test results are reported in Table 4.5, where the P-values below the significance level $\alpha = 0.05$ are indicated in boldface letters. The results show that the approaches utilizing multichannel information (NNL and EI) provide significant improvement compared to the LI approach, which processes the channels independently. Improved performance was obtained also in cases where the NNL and the EI was trained with less seizures than the LI approach. Moreover, the NNL approach performed significantly better than the EI given two and three training seizures; also when the EI approach was trained with one additional seizure.

The performance of a seizure detector evaluated on the same EEG dataset

Table 4.4: Event-based performance evaluation measures computed on the test data comparing the performance of the three detection approaches given different training sets. Sensitivities, false detection rates and alarm delays are reported in terms of median and mean (in brackets) over all 22 patients. The number of seizures used for training is indicated in the first column of the table.

		NNL	EI	LI
1	dS (%)	75 (63)	93 (76)	75 (57)
	R_{fa} (/h)	0.06 (0.26)	0.31 (0.71)	0.09 (0.45)
	D (s)	7.6(10.4)	5.5 (8.1)	9.7 (12.1)
2	dS (%)	100 (74)	100 (76)	60 (52)
	R_{fa} (/h)	0.11 (0.29)	0.31 (0.71)	0.10 (0.60)
	D (s)	7.8 (9.8)	5.5 (8.4)	5.0 (8.2)
3	dS (%)	100 (78)	100 (81)	90 (64)
	R_{fa} (/h)	0.12 (0.40)	0.50 (0.76)	0.14(0.61)
	D (s)	10.5 (10.1)	7.0 (8.1)	6.8 (9.1)
4	dS (%)	100 (76)	100 (82)	93 (64)
	R_{fa} (/h)	0.11 (0.33)	0.47 (0.82)	0.43 (0.77)
	D (s)	9.8 (10.7)	7.0(8.4)	7.9 (9.8)
5	dS (%)	100 (80)	100 (83)	100 (67)
	R_{fa} (/h)	0.14 (0.41)	0.50 (0.88)	0.23(0.76)
	D (s)	9.0 (10.0)	7.0 (8.5)	8.5 (11.2)

is reported in [186]. This algorithm reaches a median of 2 false detections daily. Moreover, using one training seizure, it reaches 55% sensitivity on five randomly selected patients, claimed to be representative for the dataset. Given one training seizure the NNL algorithm presented here produces only 1.5 false detections daily, and reaches a median detection sensitivity of 75%, confirming the superiority of our approach.

4.3.4 Discussion

In this section we presented a novel patient-specific seizure detection algorithm and compared it to two existing approaches. All the three solutions make use of the same feature set; they differ in how the individual channel information is integrated into a final decision. The late integration approach processes the channel information independently, and integrates the channel decisions with an OR function. The early integration approach stacks the features extracted from all the channels in one long feature vector, which is used to train the classifier. Finally, the nuclear norm approach constructs channel-feature

Table 4.5: P-values obtained by Wilcoxon signed rank tests comparing the detection approaches. The number of training seizure used to train each method is shown after the name of the approach in the different rows and columns. As we are interested to know whether spatial/ structural information significantly improves seizure detection, comparisons were made between NNL m and EI n; NNL m and LI n or EI m and LI n for $m \leq n$. Values corresponding to significant differences at level $\alpha = 0.05$ appear in bold.

NNL vs EI					
	EI 1	EI 2	EI 3	EI 4	EI 5
NNL 1	0.6389	0.6482	0.4842	0.5034	0.6051
NNL 2		**0.0459**	**0.0335**	0.0619	0.1997
NNL 3			**0.0392**	**0.0170**	0.1485
NNL 4				0.1886	0.1311
NNL 5					0.0918
NNL vs LI					
	LI 1	LI 2	LI 3	LI 4	LI 5
NNL 1	0.1396	0.1011	0.3221	**0.0221**	0.0777
NNL 2		**0.0061**	**0.0033**	**0.0014**	**0.0056**
NNL 3			**0.0002**	**0.0002**	**0.0010**
NNL 4				**0.0002**	**0.0004**
NNL 5					**0.0002**
EI vs LI					
	LI 1	LI 2	LI 3	LI 4	LI 5
EI 1	0.0630	0.0534	0.0617	**0.0156**	**0.0244**
EI 2		**0.0108**	**0.0045**	**0.0067**	**0.0108**
EI 3			0.0457	**0.0355**	**0.0420**
EI 4				**0.0078**	**0.0208**
EI 5					**0.0071**

matrices and exploits structural information from these during the learning procedure.

All the three approaches facilitated successful seizure detection. However, our results suggest that methods analysing the multichannel EEG as one entity perform better than approaches analysing the channels independently. This confirms the results presented by [83], where the early integration and late integration approaches were compared in a non-patient specific setting. Moreover, enforcing a low-rank structure by nuclear norm regularization is proven to bring additional improvement compared to the early integration approach, where the inter-channel information is synthesized without postulating any underlying

model.

Our seizure detection system performed better than a reference method reported by [186], tested on the same online available EEG dataset. Direct comparison with other patient-specific studies in the literature is not feasible, as they use different datasets, moreover, those datasets often contain preselected patients (e.g. [169, 144]). In order to demonstrate the real-life clinical applicability of our method, we chose to avoid any preselection whatsoever.

The detector presented in this work is a patient-specific system. It achieves high performance by capturing spatial information from the available multichannel seizure recordings. The spatial information is incorporated by assuming a low-rank model underlying the seizure epochs, defined by the relative discriminative power of the features and their distribution over the channels. Our model and the learning algorithm is closely related to the concept of singular value decomposition. Similar structural assumptions were made by [1, 52], where the epileptic seizures were successfully localized by canonical decomposition, a possible tensor extension of singular value decomposition.

The localization can be expected to be consistent among the seizures of patients with unifocal epilepsy. However, seizures of multifocal epilepsy patients will have different spatial distributions and will not all be detected by our algorithm, unless seizures of all types occurring in the patient are available in the training.

A real-life application requires that the seizure detection system collects sufficient information already from a few seizures, and can start monitoring within a short time. Thus, our classifiers are trained using small amount of seizure datapoints. The consequence of this is twofold. This results in a highly unbalanced training set, where, in addition, the dimensionality of one datapoint is relatively large compared to the number of available positive samples. Such system is prone to overfitting, nevertheless, the representation and model assumption used within the nuclear norm learning approach helps overcome this issue.

Due to the unbalanced input data, additional bias term correction has to be performed after the training to obtain the correct detection threshold. Considering the low amount of available seizure samples, the bias term correction was performed on the training data. The classification performance was assessed by computing the misclassification error. We have tested several alternative optimality criteria, which take into account the skewed class ratios, such as F2 score [1], balanced error rate [2], or a certain working point on the

[1] F-score is an evaluation metric combining precision (=TP/(TP+FP)) and recall (=TP/(TP+FN)) using their harmonic mean, with TP: true positives, FN: false negatives, FP: false positives. F2-score weights recall twice as much as precision.

[2] Balanced error rate is the average of errors over each class

ROC curve. However, none of them showed significant improvement compared to the misclassification error.

The performance of our algorithm may be further improved by applying additional features, however, finding an optimal feature set is beyond the scope of this study. The features used here are successfully applied in the literature, and they are developed to characterize repetitive, rhythmic seizure patterns. Nevertheless, seizures which are difficult to assess visually, due to the lack of such patterns or artefacts, will also be poorly described with these features. On the contrary, different data representations capturing more complex interactions between the channels might improve detection in these difficult cases as well.

Besides the morphology, spectral structure and spatial distribution, the temporal evolution is an important characteristic of the seizure pattern as well [197, 186]. A possible extension of the presented algorithm is to take into account temporal evolution by analyzing consecutive EEG epochs together, forming a tensor from their feature-channel matrices. Both training and detection are performed on such tensorial data. The size of the tensors are $n \times m \times k$, with n and m are the number of channels and extraced features, respectively, and k is the number of consecutive EEG epoch analysed at once. When choosing an appropriate value for k, one has to take into account that a large k will delay the detection. On the other hand, small k captures less information.

We presented successful seizure detection by using linear models, i.e. linear separation of seizure and non-seizure data. Although a non-linear separation might be better suited for this problem, the low amount of available seizure information does not allow the use of non-linear kernels. The early integration approach has been tested with an RBF kernel, however, it performed worse compared to the other approaches, and the test results are not shown here. Nonetheless, future work will be focused on structure-preserving tensorial kernel methods, which were shown to be relevant in solving such problems [188].

This study presents for the first time the nuclear norm learning approach applied for seizure detection. There might be several related EEG applications where this technique can be beneficial. For instance, it is directly applicable in brain-computer interfaces based on event-related potentials or event-related synchronization and desynchronization. Such responses are consistent in their waveform, frequency content and spatial distribution among the trials, consequently, they can also be modelled with low-rank structures. Using the nuclear norm learning approach could reduce the training time necessary for reaching successful discrimination of these brain responses.

4.4 Conclusion

This chapter tackled the problem of automated seizure detection. First, the utility of a universal seizure detection algorithm was explored. Although the proposed algorithm achieved promising preliminary results, its practical use as a warning device would require even lower false detection rates. Therefore, we subsequently developed an alternative, patient-specific approach. Considering that the characteristics of the ictal patterns are consistent across the seizures of a focal epilepsy patients, an improved performance is expected. Indeed, similar sensitivity could be achieved while reducing the number of false alarms and the alarm delay by 60%.

The strength of the patient-specific method lies within conveying structural information from the multichannel EEG data. Such formulation allows to automatically include crucial spatial information characteristic to a patient's seizures. The results of the proposed approach were compared with two other techniques, making use of the same feature set but integrating the multichannel information in different ways. Our results show improved detection performance compared to those alternative approaches, even if less seizure information is available for training. We conclude that the presented method potentially reduces the time needed to train the detection system before starting monitoring.

In a future practical setting a combination of a universal and a patient specific system could be beneficial. More specifically, at the arrival of a new patient a universal seizure alarm system can be activated. In case too many false alarms are set off, the detection threshold can be tuned by the caregiver. Alternatively, active learning strategies may be used to refine an initial classifier [21]. After the occurrence of the first seizure, however, the patient-specific system should be trained and switched on.

Chapter 5

Block term decomposition for extracting seizure sources from EEG

In the previous chapter we discussed the issue of automated seizure detection. Once a seizure occurrence is identified, the next step in the diagnostic procedure is to determine the seizure onset zone based on the EEG. As explained in section 2.4.2, the visual interpretation of the EEG is often hindered by artefacts superimposed on the ictal pattern. Several BSS methods exist which can remove artefacts or extract the source of interest. As each method uses different model assumptions, their use is appropriate in certain situations and are limited in others. In this chapter BTD, a novel tensor decomposition technique is applied to extract the seizure source from ictal EEG patterns. In section 5.1 a more detailed motivation is given for the choice of methodology. Subsequently, section 5.2.1 presents two alternative ways of representing EEG signals in a tensor. Each alternative presumes a different underlying signal model. Accordingly, appropriate model parameters have to be chosen carefully. Section 5.2.2 elaborates further on this issue. Sections 5.2.3 and 5.2.4 presents the simulation study and the clinical data which are used to test the performance of the decomposition. Results are analysed in section 5.3 and section 5.4 is dedicated to discussion. This study is also described in [101].

5.1 Introduction

Recordings of neural activity, such as EEG, are an inherent mixture of different ongoing brain processes as well as artefacts and are typically characterised by low signal to noise ratio. Several studies have applied various BSS methods to overcome this limitation of EEG.

BSS techniques can extract and remove artefacts contaminating the EEG recordings. The first study in this direction applied principal component analysis (PCA) to estimate and remove eye activity [15]. Later on, independent component analysis (ICA) has gained popularity. While PCA assumes orthogonal source component, the independence constraint imposed by ICA is more realistic. This theoretical advantage has also proven effective in practice. ICA does not only outperform PCA but it is also capable of removing a wide variety of artefacts from the multichannel EEG [112]. From a clinical perspective, it was shown that elimination of artefacts by ICA increases the quality and interpretability of ictal EEG recordings [216]. However, muscle artefacts, which commonly occur during ictal recordings, might cause crosstalk between brain and artefact sources. Canonical correlation analysis (CCA) used as a BSS technique [40] outperformed the ICA JADE algorithm in removing muscle artefacts. It was also shown that EEG source localisation is rendered more reliable if eye and muscle artefacts are removed using spatially constrained ICA and BSS-CCA, respectively [89].

It is clear that BSS techniques are very useful for removing artefact sources and help the visual interpretation of the EEG signals. Importantly, the source of interest itself can also be extracted with BSS approaches. A well estimated ictal source provides useful information about the epileptic seizure morphology and spatial distribution. The topographic maps corresponding to the ictal component indicate the lateralisation [153] or even the localisation of the seizure onset [1, 52].

The BSS methods discussed until now, namely PCA, ICA and CCA, work on two-dimensional data. In case of EEG data this means that the input matrix describes $channel \times time$ information. EEG datasets, however, are often inherently multidimensional, comprising information in time, along different channels, subjects, trials, etc. Additional information may be conveyed by expanding the signal into even more dimensions, e.g. incorporating spectral features applying wavelet transform. The underlying sources might show differences in each of these modes. Therefore, tensor based blind source separation techniques which can extract the sources of interest from such multiway arrays, simultaneously exploiting the signal characteristics in all dimensions, have gained increasing interest.

Canonical polyadic decomposition (CPD) has been successfully used to extract epileptic seizure activity from wavelet transformed EEG data [1, 52]. CPD decomposes the $channel \times time \times frequency$ EEG tensor into a sum of rank-1 tensors. As such, each extracted component is defined by the combination of exactly one spatial, temporal and spectral signature. CPD is a trilinear model, i.e. the vectors along each mode are proportional to each other. For example, the spectral signature is linearly scaled over the time and channel modes, where the weights of the scaling are given by the values of the temporal and spatial signatures. Similarly, the temporal and spatial signatures are linearly scaled over the other two modes. Hence, the CPD model assumes that the source maintains the same spectral structure and topography within the observed window. However, focal epileptic seizures are typically characterised by evolving repetitive sharp waves. The evolution can occur in frequency, amplitude, morphology and topography [197]. Decomposition methods which allow more variability and more interaction between the factors are needed in order to capture such nonstationarities.

Here we describe the first biomedical application of Block Term Decomposition (BTD) [44, 42], a generalisation of CPD allowing decomposition in terms which are of higher multilinear rank. As such, depending on the mode–n rank of a certain component, BTD facilitates modelling two or more distinct underlying patterns present along mode–n. We decompose wavelet transformed EEG tensors into rank-$(L_r, L_r, 1)$ terms to extract the epileptic source from ictal EEG recordings. Such decomposition facilitates the extraction of sources with a fixed spectral structure which spatially spread over time; or sources which evolve in frequency but retain a fixed localisation.

Alternatively, EEG signals can be modelled as a sum of exponentially damped sinusoids [104, 39, 71]. Mapping the signal observations to Hankel matrices allows the retrieval of the poles generating the system by singular value decomposition [122]. Furthermore, such representation leads to a new, deterministic blind source separation technique. More specifically, a mixture of R signals, each generated by L_r poles, can be uniquely decomposed into rank-$(L_r, L_r, 1)$ terms [43]. Therefore, we will also apply BTD-$(L_r, L_r, 1)$ on EEG tensors, where the slices along the spatial mode are Hankel matrices corresponding to the observations from each EEG channel.

In a simulation study we investigate the robustness of the tensor decomposition techniques against noise, the impact of the chosen model parameters, as well as the advantages and differences of each approach. Finally, we compare the performance of BTD and CPD on various real ictal EEG signals recorded from different patients.

5.2 Materials and Methods

5.2.1 Tensor construction

Multichannel EEG data naturally take the form of a matrix $\mathbf{A} \in \mathbb{R}^{S \times Ch}$, where S and Ch correspond to the number of samples and channels, respectively. Below we present two different approaches to extend this to a tensorial representation by expanding the time course into an extra dimension, with the aim of conveying additional information about the signal.

Wavelet expansion

As the frequency content of EEG signals carries crucial information, wavelet transformation is often used to expand the EEG matrix into a tensor $\mathcal{A} \in \mathbb{R}^{S \times Ch \times F}$, where F is the number of wavelet scales or frequencies [1, 52]. Before wavelet transformation the EEG data is normalised by subtracting the mean and dividing each channel signal by its standard deviation. Note that after decomposition the scalp potentials are multiplied again with this standard deviation in order to preserve topographic information. Continuous wavelet transform (CWT) was performed using the *mexican hat* wavelet of 30 scales, corresponding to a linear range of frequencies between $1 - 30$ Hz. After tensor decomposition the different modes describe the spatial, spectral and temporal signature of the components. The source signals can be reconstructed by an inverse CWT (ICWT) of the retrieved time-frequency planes. We will refer to a BTD performed on tensors obtained by wavelet expansion as CWT-BTD.

Hankel expansion

EEG signals can be modelled as the sum of exponentially damped sinusoids [104, 39, 71]. Such signal model allows unique blind source separation in rank-$(L_r, L_r, 1)$ terms [43]. To exploit the desired structure, each EEG channel signal $[a_1 \ a_2 \ \cdots \ a_S]$ is mapped to a Hankel matrix $\mathbf{H} \in \mathbb{R}^{J \times K}$ with $J + K - 1 = S$. The Hankel matrix is structured as follows:

$$\begin{bmatrix} a_1 & a_2 & a_3 & \cdots & a_K \\ a_2 & a_3 & \cdots & a_K & a_{K+1} \\ a_3 & \cdots & a_K & a_{K+1} & a_{K+2} \\ \vdots & \iddots & \iddots & \iddots & \iddots \\ a_J & a_{J+1} & \cdots & a_{S-1} & a_S \end{bmatrix}$$

Depending on the number of underlying poles generating the signals, the Hankel matrix has low rank and the BTD is unique [43]. A Hankel matrix of a pure exponential is rank 1, while the ones of sinusoids and exponentially damped sinusoids are rank 2. Noisy or nonstationary signals such as chirps give rise to Hankel matrices of higher rank. Before creating the Hankel matrices, the EEG channel signals are divided by their standard deviation. Note that the mean is not subtracted here as this could introduce an additional pole. After the tensor decomposition the signal can be reconstructed by taking the mean along the anti-diagonals of the retrieved matrix. We will refer to a BTD decomposition performed on tensors obtained by Hankel expansion as H-BTD.

5.2.2 Model selection

Certain model parameters have to be determined prior to performing blind source separation. The number of extracted components or terms R have to be chosen for both CPD and BTD. Additionally, the rank of each mode needs to be set for BTD. In case of BTD-$(L_r, L_r, 1)$, this means to determine which mode should be rank-1 and choose the rank L_r for the two other modes. If not stated otherwise, we set $L_1 = L_2 = ... = L_R$.

Several procedures have been proposed for automatic model selection in tensor decompositions. For CPD type models the core consistency diagnostic [19] seems to be the most powerful approach [151], and has been successfully used to guide the blind source separation of epilepsy tensors [1, 52]. However, parameter selection for more flexible tensor models such as BTD-$(L_r, L_r, 1)$ is the topic of still ongoing research (see Discussion for an overview), and is out of the scope of this study. Our aim is rather to give an insight to the sensitivity of CPD and BTD to the different parameters and to illustrate what can be achieved with well-chosen model parameters.

Therefore, we simulated various ictal activity patterns superimposed on artefacts and background activity. The signals were subsequently decomposed with CPD and BTD using a wide range of values for each model parameter in order to investigate the impact of the chosen model parameters. The goodness of the model fit is evaluated in terms of the dipole localisation error as well as

based on the root mean square error (RMSE) between the spatial distributions, time courses and the $time \times frequency$ or Hankel matrices of the simulated and extracted ictal pattern. The results of the simulation study are compared to results obtained by the core consistency measure in case of CPD.

5.2.3 Simulation study

EEG activity of 2s length was simulated in different scenarios following [50].

1. Stationary seizure: One dipole with a sinusoidally varying moment at 5.7Hz, located at coordinates $(x, y, z) = (-0.5, 0, 0.1)$, where x, y and z, ranging between -1 and 1, indicate the relative positions between the following extrema: left ear to right ear, posterior to anterior and from down upwards through the Cz electrode, respectively.

2. Seizure with varying frequency: One dipole with a moment of linearly decreasing frequency from 8Hz to 4Hz located at coordinates $(x, y, z) = (-0.5, 0, 0.1)$.

3. Seizure with varying localisation: Two dipoles, each with a sinusoidally varying moment at 5.7Hz located at $(x, y, z) = (-0.5, -0.2, 0.1)$ and $(x, y, z) = (-0.5, 0.5, 0.1)$. While the activity of the first dipole gradually decreased, the activity of the second dipole increased in amplitude.

The forward problem was solved for each scenario in a three-shell spherical head model consisting of a brain, a skull and a scalp compartment [179]. The ratio between the conductivities of the brain, skull and scalp compartment was equal to $1 : 1/16 : 1$, respectively [159], where the conductivity of the brain and scalp was $3.3 \cdot 10^{-4} \Omega/mm$ [34]. The radii of the outer boundary of the brain, skull and scalp compartments were set to 8 cm, 8.5 cm and 9.2 cm, respectively. The forward solution was computed for twenty-one electrodes placed according to the 10/20 system with 2 additional electrodes over the temporal region. The time course of the scalp potentials was stored in a 500×21 dimensional matrix $\mathbf{A}$, representing 2s of EEG with sample frequency of 250 Hz. Awake background EEG activity was recorded with the same electrode configuration from a healthy subject. Muscle artefacts were separated from a contaminated segment of background activity using BSS-CCA [40]. Subsequently, the muscle artifacts were superimposed on a clean background EEG segment and the data were stored in a noise matrix $\mathbf{B}$. In the simulation study, the noise matrix $\mathbf{B}$ was superimposed on the signal matrix $\mathbf{A}$ containing the ictal activity: $\mathbf{X}(\lambda) =$

$\mathbf{A} + \lambda \cdot \mathbf{B}$ with $\lambda \in \mathbb{R}$. We varied the parameter λ resulting in various signal-to-noise ratio (SNR) levels, quantified as:

$$\mathrm{SNR}(\lambda) = \frac{\mathrm{RMS}(\mathbf{A})}{\mathrm{RMS}(\lambda \cdot \mathbf{B})}, \tag{5.1}$$

where the root mean square value (RMS) of a signal matrix $\mathbf{M} \in \mathbb{K}^{Ch \times S}$ consisting of Ch channels and S samples, is defined as:

$$\mathrm{RMS}(\mathbf{M}) = \sqrt{\frac{1}{Ch \cdot S} \sum_{ch=1}^{Ch} \sum_{s=1}^{S} (\mathbf{M}(ch, s))^2}. \tag{5.2}$$

The noisy ictal EEG segments were expanded with the wavelet or Hankel method and were subsequently decomposed with CPD and BTD in order to extract the ictal component. Note that CPD was not applied on tensors obtained with Hankel expansion, as the Hankel matrix of a sinusoidal or chirp signal is always different from rank-1. The component corresponding to the ictal source was selected automatically as the one showing the lowest RMSE in spatial distribution with the simulated ictal source. Subsequently, one dipole was fitted on the extracted ictal source signal to compute the localisation error. The goal of the simulation study was to assess the robustness of each method against noise. Furthermore, as explained above, it also serves to investigate the impact of different choices of model parameters and ultimately to determine the optimal model parameters.

5.2.4 Clinical examples

Ictal EEG recordings were selected from the database used in [52, 227]. The original database consisted of 37 refractory partial epilepsy patients who underwent full presurgical evaluation including seizure semiology, structural MRI, interictal EEG, subtraction of ictal SPECT coregistered with MRI (SISCOM) and neuropsychological assessment. A patient was included in the database if all measurements were concordant and reliably defined the epileptogenic zone. In a majority of cases the seizure onsets were correctly localised using CPD of wavelet transformed EEG tensors [52]. In these cases the trilinear signal model assumed by CPD is sufficient, therefore, we don't expect an improvement using BTD. However, in cases where no perfect separation was obtained by CPD due to severe artifacts, BTD might provide improved results. Although [52] focussed on localising the seizure onset zone, one might be interested in modelling other aspects of the seizures, such as its evolution in morphology or topography. As opposed to CPD, BTD can model

such nonstationary sources. Here we will discuss the following patients, each representing a particular case (severe artefacts or presence of nonstationarities), where we expect that BTD can provide more appropriate signal models than CPD.

Patient 1

Patient 1 suffers from right temporal lobe epilepsy. The seizure consists of 5–6 Hz activity lateralised to the right, most prominently present over the right anterior and midtemporal region (F8, T4 and right sphenoidal channels). Severe eye blinks and muscle artefacts are superimposed on the low voltage ictal activity at onset (Figure 5.8a). Our aim here is to separate the seizure activity from the artefacts and background using a 2s EEG segment at onset and thereby localise the seizure onset zone as in [52]. The window length of 2s was chosen considering that the number of samples provide sufficient amount of information about the signal, but it is short enough to assume that the seizure does not spread yet from the onset region. As we are interested in the exact onset localisation of the seizure, the spatial mode of BTD is chosen to be rank-1, while the frequency and temporal modes are higher rank.

Patient 2

Patient 2 suffers from left temporal lobe epilepsy. The seizure starts with a 4Hz delta rhythm which is most prominent over the left anterior and midtemporal region (F7, T3 and left sphenoidal channel). 11 seconds after onset the seizure pattern evolves in amplitude and frequency into a sharp, up to 8 Hz theta activity. Our aim here is to correctly model the frequency evolution of the seizure. Therefore, the frequency and temporal mode of the BTD is chosen to be higher rank while we assume a stationary localisation, i.e. rank-1 spatial mode. As the transition takes place over a longer period of time, here we use a 10s long EEG segment, shown in Figure 5.9a.

Patient 3

Patient 3 suffers from right temporal lobe epilepsy. The seizure starts with a high amplitude 4Hz delta activity over the right anterior, mid- and posterior temporal region (F8, T4, T6 and right sphenoidal channels). After 14 seconds the seizure activity spreads to the bi-fronto-central region. Our aim here is to correctly model the spatial spread of the seizure using a 10s EEG segment shown in Figure 5.10a. Therefore, the spatial and temporal mode of the BTD

is chosen to be higher rank and we assume a stationary frequency, i.e. rank-1 frequency mode.

5.3 Results

5.3.1 Simulation study

Scenario 1 and 2

CPD successfully extracted the single epileptic source from a $channel \times time \times frequency$ tensor in case of a stationary ictal source or an ictal source with evolving frequency. Figure 5.1 shows the RMSE in time course and in spatial distribution between the simulated and reconstructed ictal source. The ictal source is captured already in the first CPD component for an $SNR > 0.4$, and the reconstruction does not benefit from extracting additional components. However, for $SNR < 0.4$ the ictal signal is covered in noise, therefore, two or more components are required. In such cases one CPD component captures the ictal source and the others serve to remove artefacts and model background activity. Note that if the number of components is set too high ($R > 4$) in scenario 2, the nonstationary ictal source is split into two components, compromising the reconstruction of the time course. These observations are in accordance with results obtained with the core consistency diagnostic, suggesting 2, 3 or perhaps 4 stable components.

Figure 5.2 shows the performance of BTD on tensors obtained with wavelet expansion. In Scenario 1 and 2 the channel mode is modelled with rank-1, while the time and frequency modes are modelled with higher ranks. The results are very sensitive to the chosen number of block terms R both in case of a sinusoidal or a chirp-like ictal source. The best reconstruction can be achieved with $R = 2$ in both cases. Note that a stationary ictal source has rank-1 structure, therefore, BTD is an inherently suboptimal model. Still, one term will resemble the ictal source, where the various signatures constituting the rank-L_r term are the superposition of the true ictal pattern and noise, as depicted in Figure 5.4. However, the exact choice of $L_r > 1$ does not seem to have a large influence on the RMSE between the reconstructed and true ictal source.

In case of an ictal source with evolving frequency $L_r = 2$ gives the best reconstruction, although the performance is compromised for very low SNRs. On one hand, the ictal pattern can be captured for very low SNRs if L_r is set higher. On the other hand, setting L_r too high has similar effects as the BTD

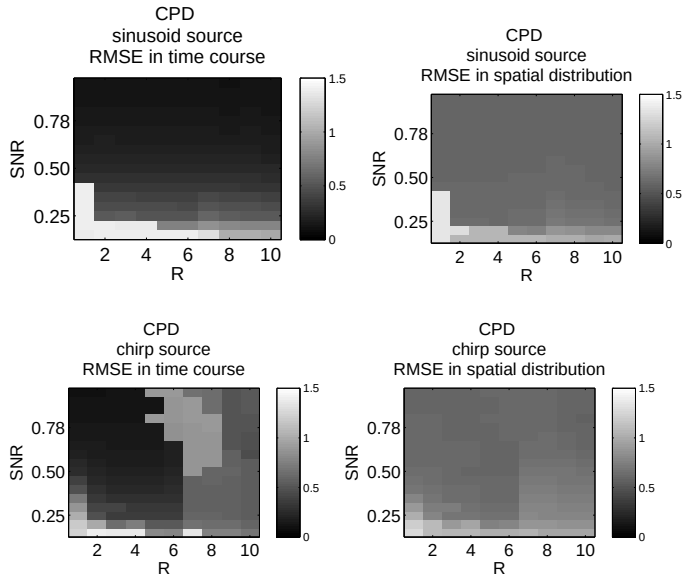

Figure 5.1: RMSE between the simulated and reconstructed ictal source obtained from $channel \times time \times frequency$ tensors with CPD for various number of extracted components (R) and various SNR values.

model of a sinusoid source: artefacts are superimposed on the ictal signal even for high SNR values, hindering interpretation.

Figure 5.3 shows the performance of BTD on tensors obtained with Hankel expansion. Regardless of the number of extracted block terms, H-BTD can robustly reconstruct the spatial map corresponding to the ictal source both in case of a sinusoidal or a chirp-like time course. Similarly, a chirp-like ictal source is well localised given an arbitrary choice for the rank of the factor matrices. However, this is not the case for the sinusoidal ictal source. Moreover, the choice of the rank has a strong influence on the reconstruction of the ictal time course. While the sinusoidal time course is best reconstructed with L_r=2 in accordance with theory, the reconstruction of the chirp-like source requires L_r=6. Note that the rank of a chirp signal depends on how nonstationary it is. With the above choices for L_r the time course of the ictal source is best reconstructed with $R = 3$ according to our simulation results.

For a direct comparison between the BSS methods, the model parameters which gave the most robust result were chosen, i.e. $R(CPD) = 4$, $R(CWT{-}BTD) = 2$, $L_r(CWT - BTD) = 2$ and $R(H - BTD)$=3, $L_r(H - BTD) = 2$ for a sinusoidal

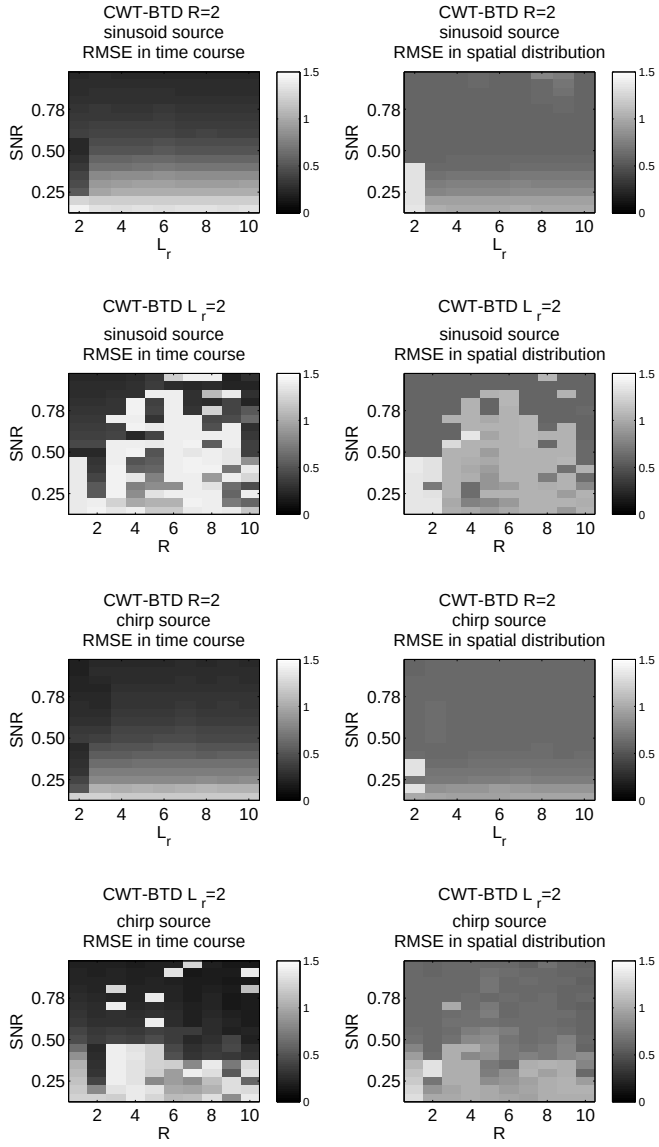

Figure 5.2: RMSE between the time courses of the simulated and reconstructed ictal source obtained from $channel \times time \times frequency$ tensors with BTD for varying SNR values and varying the number of components R while the rank of the factor matrices L_r is kept constant, or varying L_r while R is kept constant.

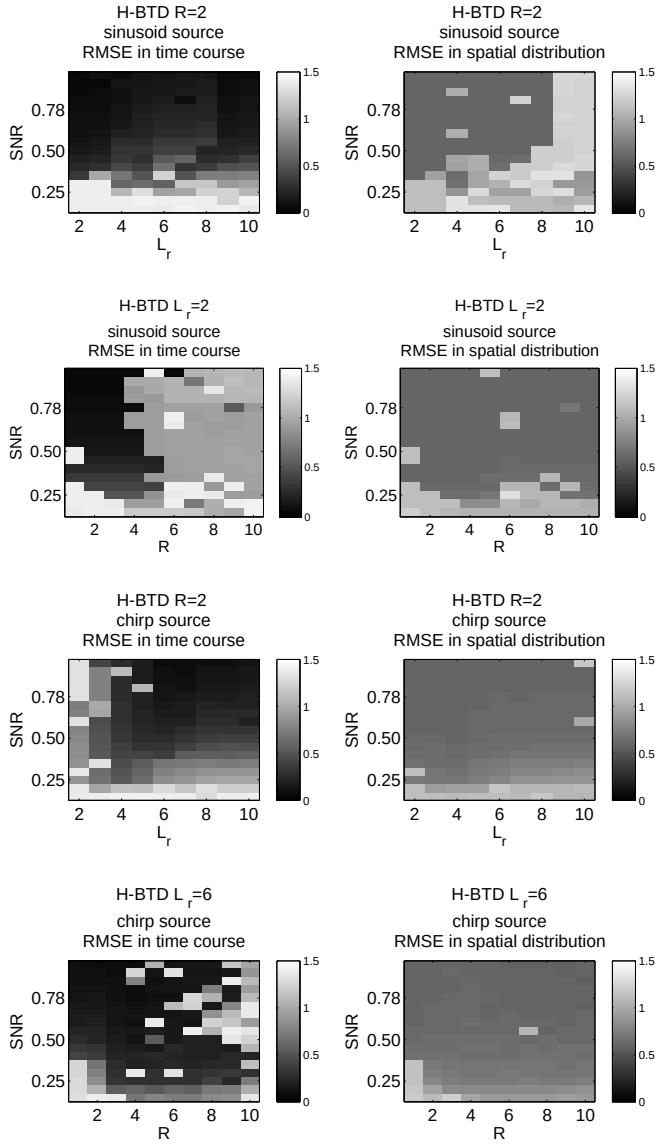

Figure 5.3: RMSE between the time courses of the simulated and reconstructed ictal source obtained from Hankel tensors with BTD for varying SNR values and varying number of components R while the rank of the factor matrices L_r is kept constant, or varying L_r while R is kept constant.

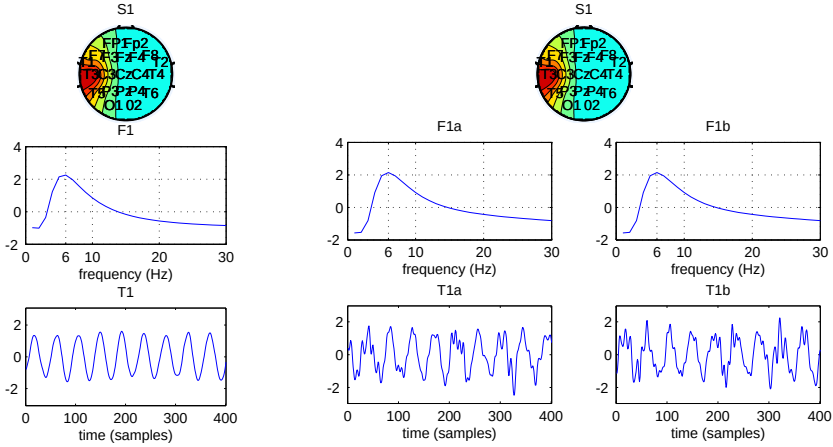

(a) CPD (b) CWT-BTD

Figure 5.4: Scenario 1: Simulated ictal source with stationary frequency at SNR=0.9. The spatial, frequency and temporal signatures are shown on the upper, middle and bottom panels, respectively. Only the components corresponding to the ictal source are shown. The spatial and frequency signature of CPD and BTD are in agreement with each other and the true ictal source. The temporal signature of CPD closely follows the true underlying ictal pattern, while noise is superimposed on the two BTD signatures (T1a and T1b) constituting the rank-2 BTD term. Still, a fair assessment of the ictal pattern is possible.

or $L_r(H - BTD) = 6$ for a chirp-like ictal source. The performance of all BSS methods are compared in Figure 5.6.

H-BTD outperformed CPD and CWT-BTD in reconstructing the time course of both the stationary and the evolving ictal source. Regarding the retrieval of the spatial maps, all three BSS approaches performed equally well, reaching an RMSE in spatial distribution below 0.6 with the simulated ictal source, which corresponds to a dipole localisation error of less than 5mm. However, CWT-BTD was not robust against very low SNRs. As already stated, BTD is an inherently suboptimal model for a sinusoidal source, which is also reflected by its lower performance in reconstructing the $time \times frequency$ matrices and the ictal time course.

In case of an ictal pattern with evolving frequency CWT-BTD achieves a lower RMSE with the true $time \times frequency$ representation compared to CPD.

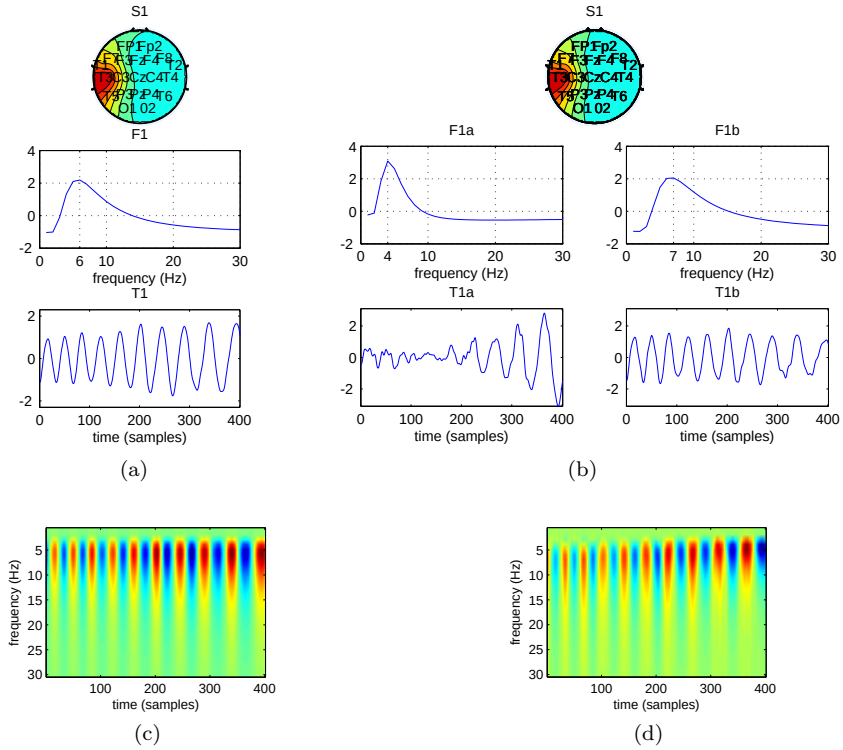

Figure 5.5: Scenario 2: Simulated ictal source with evolving frequency at SNR = 0.9. (a) CPD decomposition. The frequency signature (F1) of the first component, corresponding to the ictal source, shows a single peak at 6Hz, i.e. at the average of the start and end frequency. (b) BTD decomposition. The spatial mode of the BTD components were set to be rank-1, while the frequency and temporal modes were set to rank-2. Therefore, this block component comprises the spatial signature S1, the frequency signatures F1a and F1b and the temporal signatures T1a and T1b. The frequency signature F1a and F1b, corresponding to the ictal source, represent a spectrum peaking at 4Hz and 7Hz, respectively. From the corresponding temporal signatures one can deduce that the ictal pattern is slowing down, as T1a gains amplitude towards the end. (c) The $time \times frequency$ matrix obtained with CPD. No frequency shift can be seen. (d) The $time \times frequency$ matrix obtained with BTD. The frequency shift from 8Hz to 4Hz can be assessed.

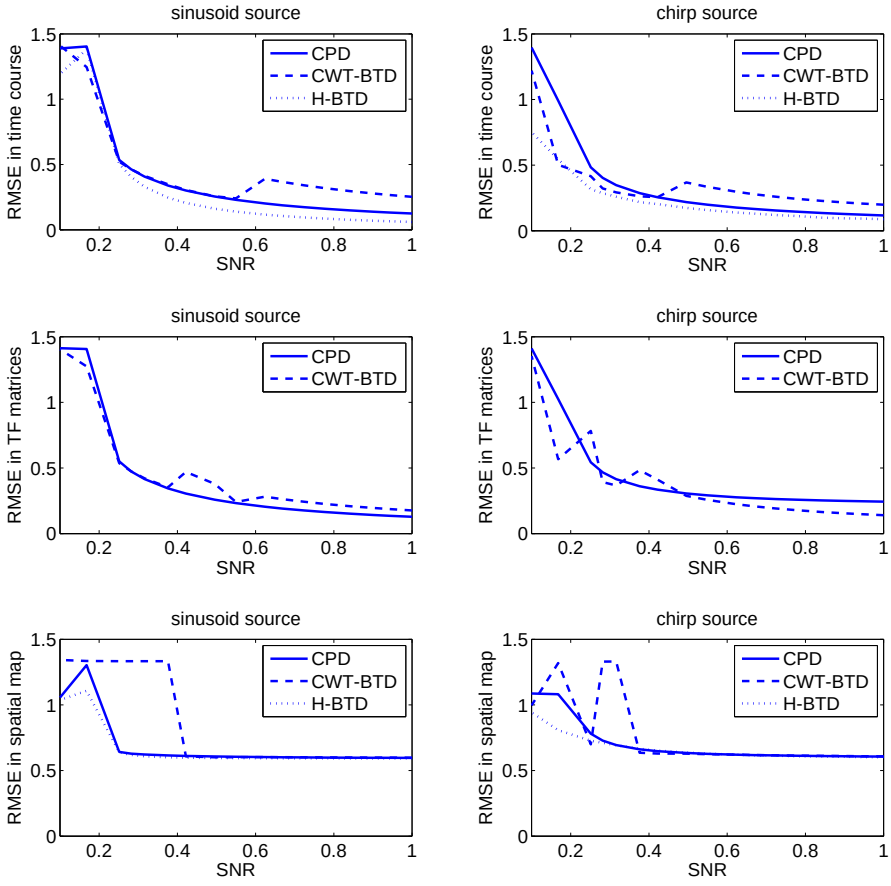

Figure 5.6: Performance of the different BSS approaches with optimal model selection, namely $R(CPD) = 4$, $R(CWT - BTD) = 2$, $L_r(CWT - BTD) = 2$ and $R(H - BTD) = 3$, $L_r(H - BTD) = 2$ for a sinusoidal or $L_r(H - BTD) = 6$ for a chirp-like ictal source.

While the frequency signature of CPD shows a single peak at 6Hz, i.e. at the average of the start and end frequency, the frequency signature vectors obtained with BTD-(1,2,2) represent a spectrum peaking at 7Hz and another peaking at 4Hz. From the corresponding temporal BTD signatures one can deduce that the ictal pattern is slowing down, the latter gains amplitude towards the end. Although they provide a sufficiently clear interpretation, note that due to the indeterminacy of the factors (see Section 3.2.5) the signatures T1a and T1b as well as F1a and F1b can be any linear combinations of the true temporal and frequency characteristics of the underlying source. However, the $time \times frequency$ matrix is unique, and can also be used to observe the spectral-temporal properties of the source. An example where SNR=0.9 was chosen is shown in Figure 5.5. Interestingly, after the inverse wavelet transform of the $time \times frequency$ matrices the reconstructed time course of the BTD ictal term shows higher RMSE with the true ictal pattern than the CPD component does.

So far the wavelet transformed EEG tensors were modelled with $L_1 = L_2 = ... = L_R = 1$ using CPD and $L_1 = L_2 = ... = L_R = 2$ using BTD. However, BTD allows different choices for each L_r. Considering that $R = 2$ gave a robust solution against noise in each case, we also tested an intermediate solution, namely, using $L_1 = 2$ and $L_2 = 1$. For low noise levels the ictal source was captured in the rank-2 term. In contrast, if $SNR < 0.6$ the high power noise requires a higher complexity representation and occupies the rank-2 term, while the seizure pattern is modelled in a rank-1 term, providing a similar ictal component as CPD.

Scenario 3

The performance of CPD and CWT-BTD was evaluated for this scenario. Our goal here is to capture a moving ictal source, therefore, we are looking for a single source with a spatial and temporal signature of higher rank and with a frequency signature of rank 1. H-BTD is not tested in this scenario, considering that using Hankel representation mode-2 and mode-3 are both different from rank-1, therefore, a source which also has higher rank spatial signature cannot be modelled in rank-$(L_r, L_r, 1)$ terms. In a similar assessment as above, varying the SNR and the model parameters we observed that the best reconstruction of the ictal source, in terms of spatial distribution was achieved with $R(CPD) = 3$ (confirmed by the core consistency diagnostic as well) and $R(CWT - BTD) = 2$, $L_r(CWT - BTD) = 2$. Using these parameters for the decomposition, a dipole was fitted to 2 CPD components and to both signatures constituting the rank-2 BTD term showing the lowest RMSE with the simulated ictal source. The localisation error of the extracted sources with respect to the corresponding simulated source is shown on Figure 5.7a. The second CPD

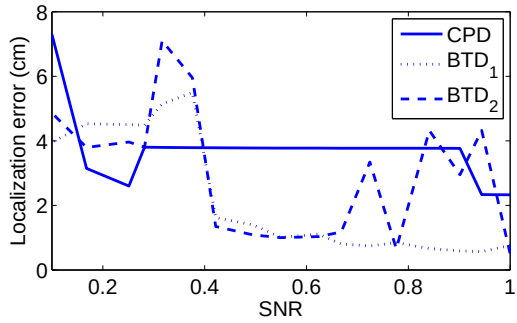

(a)

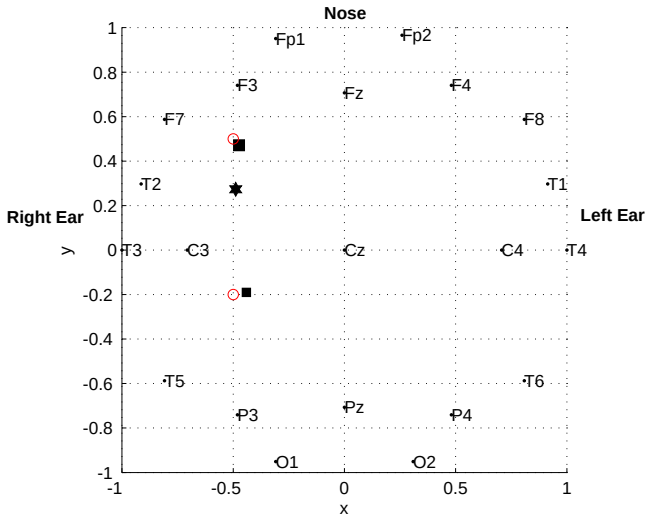

(b)

Figure 5.7: Scenario 3: Seizure with varying localisation. (a) Localisation error of the dipole fitted on the CPD component and each of the signatures in the $L_r = 2$ BTD term corresponding to the ictal source for various SNR values. (b) The positions of the simulated sources (circles), the ictal source extracted by CPD (star) and BTD (squares) for SNR =0.77.

component is omitted in this figure, as it was severely contaminated by noise and in most cases did not correspond to either of the ictal sources. In such cases, the two sources were combined in the same CPD component, located in between the initial and final location of the ictal source. In contrast, BTD successfully captured the ictal source in one $L_r = 2$ block term where the two spatial signatures capture its initial and final localisation. The positions of the simulated and the extracted ictal sources are shown in Figure 5.7b.

5.3.2 Clinical examples

The optimal number of CPD components was estimated with the core consistency diagnostic. Additionally, the results of the simulation study were also considered in the model selection for both CPD and BTD. In all the examples below, the following parameter settings were chosen: $R(CPD) = 2$, $R(CWT - BTD) = 2$, $L_r(CWT - BTD) = 2$ and $R(H - BTD) = 3$, $L_r(H - BTD) = 6$.

Patient 1

Figure 5.8 shows the results of the CPD and BTD decompositions of the 2s EEG segment at the onset of the seizure of patient 1. CPD failed to extract an epileptic source where the spatial signature matches the seizure onset zone. The spatial signature of both components shows a distribution typical for eye movement related artefacts. Interestingly, BTD comprises both these components in one block term, term 2. Note the similarity between the spatial signatures S1 of CPD and S2 of BTD, and the correspondence of F1 and T1 with F2b and T2b, as well as of F2 and T2 with F2a and T2a. The seizure activity is successfully modelled in the first block term. The spatial signature corresponds well with the seizure onset zone as assessed during the presurgical evaluation. Moreover, the frequency signature F1b indicates the dominant frequency of the seizure pattern (5Hz) and the temporal signature T1b reflects the semi-rhythmic time course of the ictal pattern. The ictal pattern was successfully extracted by H-BTD as well. The spatial signature of the retrieved CWT-BTD and H-BTD ictal term resemble each other closely.

Patient 2

The CPD and BTD decompositions of the seizure of patient 2 are depicted in Figure 5.9. The first CPD component corresponds to the ictal source, with clear left temporal localisation and a rhythmic oscillatory temporal pattern

with increasing frequency. However, these peculiar frequency characteristics cannot be directly seen on the frequency signature, which shows a single peak at 6Hz. BTD captured the seizure source in the first block term. Note the close resemblance between S1 of BTD and S1 of CPD. Moreover, the temporal signatures T1a captures the late fast one, while T1b captures the early slow oscillatory pattern of the seizure. The frequency characteristics can be directly seen from the frequency signatures, namely the 8Hz peak in F1a and the 4Hz peak in F1b. H-BTD also extracted the ictal source, successfully capturing both the localisation and the temporal pattern of the seizure.

Patient 3

The CPD and BTD decompositions of the seizure of patient 3 is depicted in Figure 5.10 (b) and (c), respectively. The first CPD component corresponds to seizure activity, showing a clear right temporal localisation and a 4Hz oscillatory pattern. The first block term captures the same ictal source (compare S1 with S1a and T1 with T1a), however, also captures a source with the same frequency characteristics located frontally. While T1b increases in amplitude after 3s, T1a decreases in amplitude after 4s. This can be interpreted as the seizure spreading from the temporal to the frontal region, in accordance with the visual assessment of the ictal EEG pattern. The changing localisation of the seizure source was not captured with CPD.

5.4 Discussion

Block term decomposition is a recently introduced tensor decomposition technique which has also been proposed as a blind source separation technique for exponential polynomials. Here we present its first biomedical application, a novel way of modelling epileptic seizure activity. We partly rely on the signal model presented in [43], and assume that the sources are the linear combinations of exponentially damped sinusoids. This signal model is conveyed by constructing a Hankel matrix from each channel time course. In addition, we present an alternative approach where the multichannel signal is expanded by a wavelet transform. The method can be seen as an extension of the method based on canonical decomposition of EEG tensors, which has been successfully used to localise the seizure onset [52, 1]. In the majority of cases a short EEG segment will be stationary in its spatial, spectral and temporal characteristics, therefore, CPD will be successful in extracting the source of interest. However, the extension of CPD to BTD is necessary when this assumption is violated. We showed three related examples, a seizure severely contaminated with eye

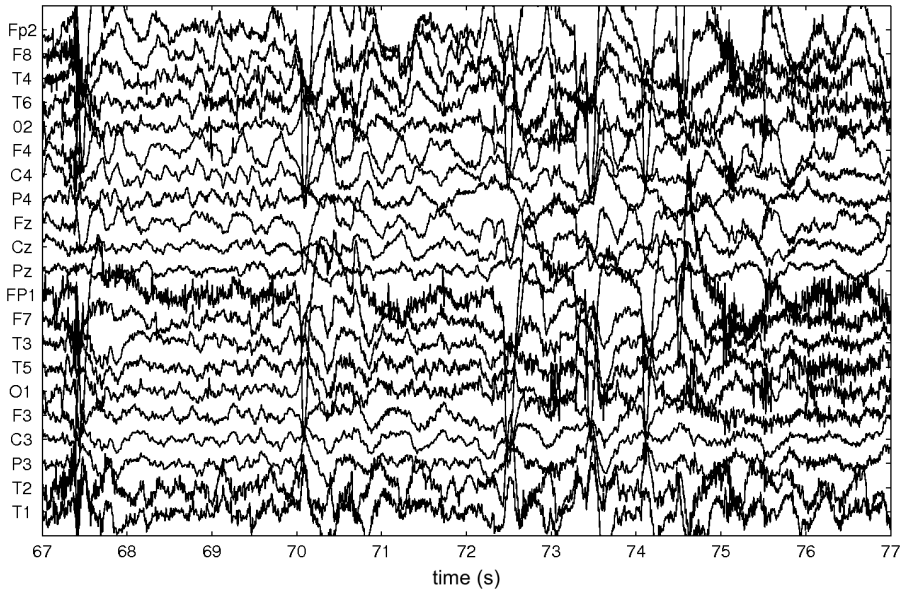

(a) Raw EEG

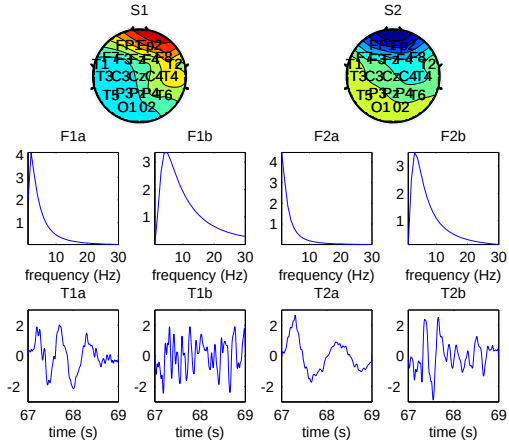

(b) CWT-BTD

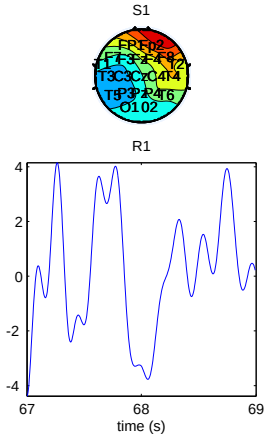

(c) H-BTD

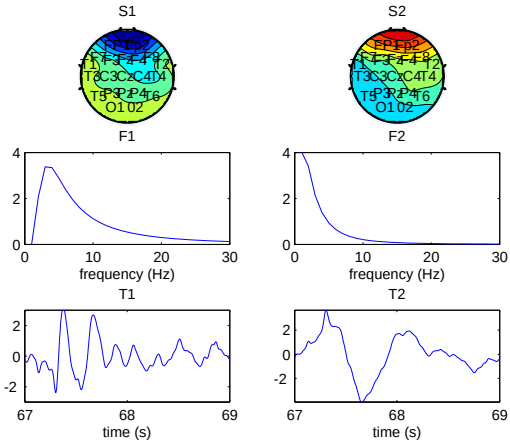

(d) CPD

Figure 5.8: (a) Seizure onset of patient 1. The first 2s window was used to model and localise the seizure onset. (d) CPD. The spatial signature of both components show a distribution typical for eye movement related artefacts, thus, CPD failed to extract an epileptic source where the spatial signature matches the seizure onset zone. (b) CWT-BTD. The second CWT-BTD component captures both eye movement related CPD components in one block term. Note the similarity between the spatial signatures S1 of CPD and S2 of BTD, and the correspondence of F1 and T1 with F2b and T2b, as well as of F2 and T2 with F2a and T2a. The seizure activity is successfully modelled in the first block term. The spatial signature corresponds well with the seizure onset zone as assessed by the epileptologist during the presurgical evaluation. Moreover, the frequency signature F1b indicates the dominant frequency of the seizure pattern (5Hz) and the temporal signature T1b reflects the semi-rhythmic time course of the ictal pattern. (c) H-BTD. The first H-BTD component capturing the seizure source is shown. The spatial signature corresponding to this source closely resembles the spatial map of the ictal source obtained with CWT-BTD. As the mode-2 and mode-3 signature do not carry physiological information, these are omitted here. Instead, R1 shows the reconstructed time course of the seizure source.

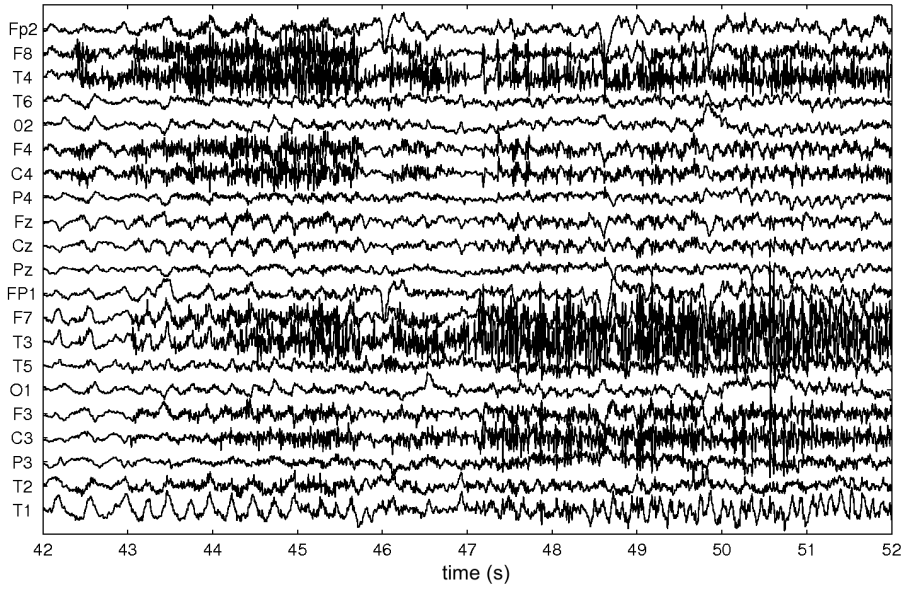

(a) Raw EEG

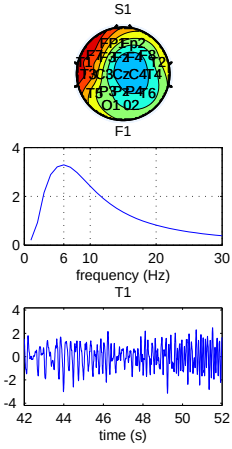

(b) CPD

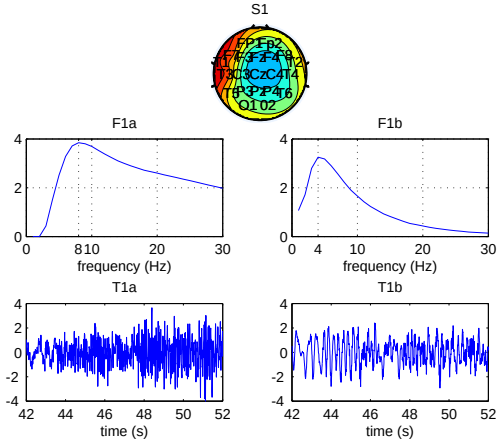

(c) CWT-BTD

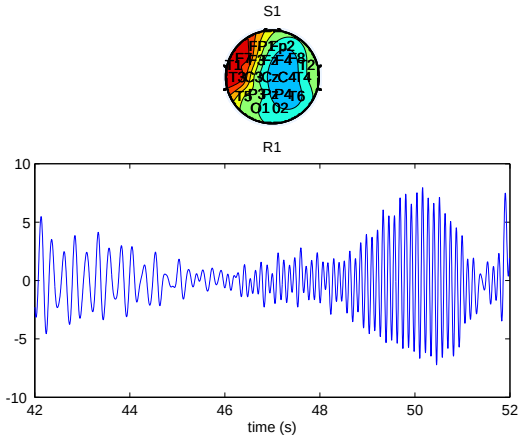

(d) H-BTD

Figure 5.9: (a) A segment of the seizure of patient 2. The whole 10s window was used to model the frequency evolution of the seizure. (b) CPD of the seizure of patient 2. Only the first component is shown. This component corresponds to the seizure source, with clear left temporal localisation and a rhythmic oscillatory temporal pattern with increasing frequency. However, these peculiar frequency characteristics can not be directly seen on the frequency signature, which shows a single peak at 6Hz. (c) CWT-BTD of the seizure. BTD captures the seizure source in the first block term, the second block term is not shown. Note the close resemblance between S1 of BTD and S1 of CPD. Moreover, T1a captures the late fast, while T1b captures the early slow oscillatory pattern of the seizure. The frequency characteristics can be directly seen from the frequency signatures, namely the 8Hz peak in F1a and the 4Hz peak in F1b. (d) H-BTD of the seizure. The first BTD term captures the seizure source. The reconstructed time course (R1) clearly reflects the peculiar characteristics of the seizure pattern, starting with a slow oscillation and evolving into a fast oscillation.

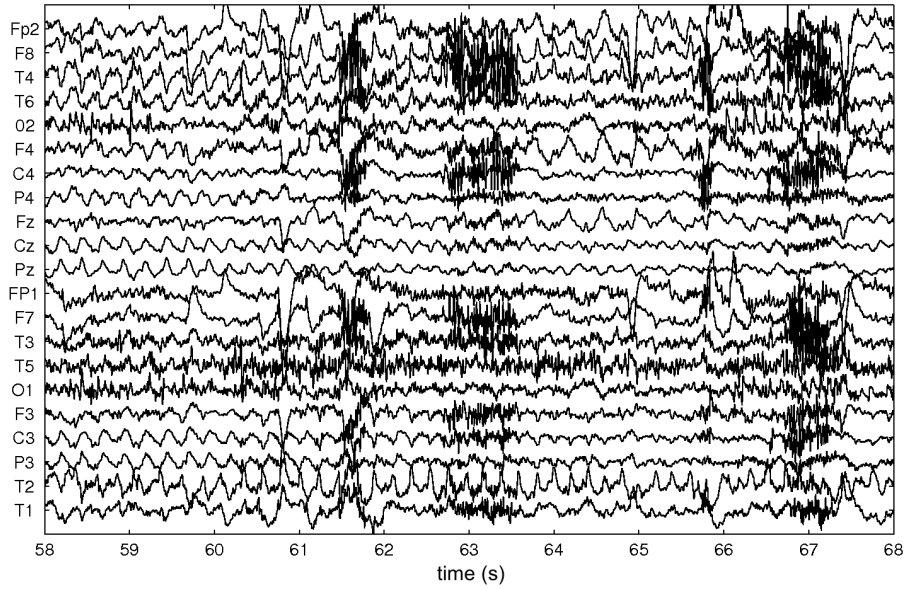

(a) Raw EEG

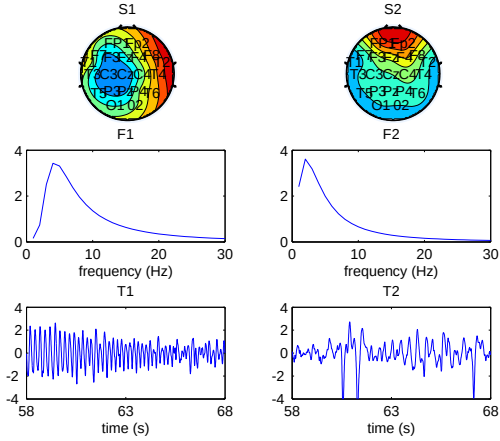

(b) CPD

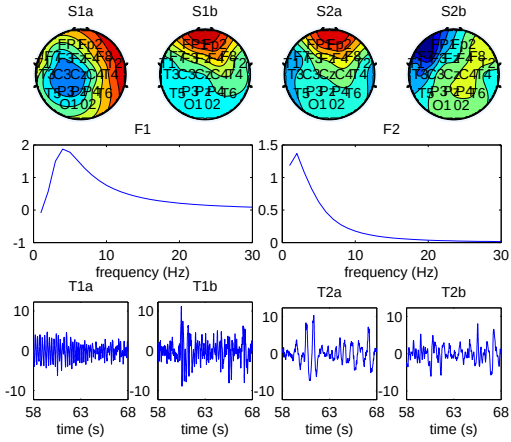

(c) CWT-BTD

Figure 5.10: (a) A segment of the seizure of patient 3. The whole 10s window was used to model the spatial spread of the seizure. (b) CPD decomposition of the seizure of patient 3. The first component corresponds to seizure activity, showing a clear right temporal localisation and a 4Hz oscillatory pattern. (c) The first block term captures the same seizure source (compare S1a and T1a with S1 and T1), however, also captures a source with the same frequency characteristics located frontally. While T1b increases in amplitude after 3s, T1a decreases in amplitude after 4s. This can be interpreted as the seizure spreading from the temporal to the frontal region, in accordance with the visual assessment of the ictal EEG pattern.

artefacts, one with evolving frequency and finally another one which spreads to distant brain regions. We demonstrated that while CPD failed to model these seizures correctly, BTD could extract an ictal source which corresponded well with the clinical assessment.

However, the success of this method largely depends on the appropriate selection of model parameters, namely the number of extracted components and the rank of the factor matrices. In a simulation study we investigated the impact of the model parameters given different underlying ictal patterns and different noise levels. We found that H-BTD was very robust against noise and against the number of extracted components. It outperformed CPD and CWT-BTD in reconstructing the time course of the ictal pattern. However, depending on the waveform of the ictal source, different rank settings were necessary. In contrast, the best model parameters for CWT-BTD were identical regardless of the underlying ictal pattern. Although CWT-BTD was less robust than CPD

or H-BTD against a SNR below 0.4, one can expect lower noise levels in real EEG recordings.

The optimal choice for L_r and R found in this particular simulation study can not be generalised, in fact, it strongly depends on the characteristics of both the ictal source and the artefacts. Nevertheless, considering that low rank models are realistic in this application and the chosen tensor representations, a rapid visual evaluation for setting the model parameters is feasible. Several procedures have been proposed for automatic model selection of tensor decompositions. Some are specific to CPD, while others were proposed for a general Tucker3 model. Note that the latter are also applicable to CPD and BTD-$(L_r, L_r, 1)$ type decompositions, i.e. restricted Tucker3 models. A commonly followed approach consists in estimating the optimal model parameters based on the decrement of the Tucker3 model error while increasing the complexity of the model, as performed in DIFFIT [208, 116]. However, certain artefacts, such as muscle related activity, might account for a large amount of variability in the data but cannot be modelled with a low rank component. Consequently, such methods overestimate the rank or the number of components in the current application. In fact, we are not interested in modelling artefacts or noise, but in correctly modelling the source of interest. In view of this, an interesting tool was implemented in Tensorlab [192], which chooses the number of rank-1 terms for a CPD decomposition given a desired model fit as the corner of the L-curve [26] representing the trade-off between fit and the order of the model. Note that this approach requires a reliable estimate of the noise level. Subsequently, model selection for a BTD-$(L_r, L_r, 1)$ type decomposition can be performed by clustering the rank-1 terms to form R rank-$(L_r, L_r, 1)$ terms, where R is estimated as the number of significant singular values of the rank-1 factor matrix, or based on the gap statistic [207]. Alternatively, a Bayesian framework for model selection based on automatic relevance determination was proposed and proven to outperform DIFFIT [151]. Nevertheless, in the same study the core consistency diagnostic [19] was shown to be the most robust technique for estimating CPD models [151]. The core consistency diagnostic has been successfully applied for CPD model estimation for decomposing epilepsy tensors [1, 52]. Although the core consistency diagnostic has recently been extended for testing the validity of hypothesised restricted Tucker3 models [118], it has not been applied or evaluated yet as a systematic tool for model parameter estimation. Future work will focus on experimental validation and comparison of the different model selection approaches for BTD-$(L_r, L_r, 1)$ decompositions in a realistic simulation study and on real EEG data.

In this study we showed various examples where the BTD provides a better model of an epileptic seizure than CPD. These more accurate models can

lead to better source localisation as well as to better feature extraction, and, consequently, more successful seizure detection. Furthermore, a wide range of neuroscience applications could benefit from BTD. CPD, as an exploratory tool for wavelet transformed event related potential (ERP) data successfully revealed condition-specific differences in a visual task paradigm [152]. However, the evoked response of some subjects deviated too much from the average activity, therefore, they did not contribute to the CPD source representing the condition-specific effect. In other words, the assumption behind CPD analysis that the same stimuli elicit the same response in all subjects was violated, leading to a model which did account for the subject specific differences. A BTD type decomposition can offer a more flexible model and we anticipate that it might not only yield more accurate results but allow more insight into subject specific brain dynamics. CPD has also been shown to be a promising tool in brain computer interfaces. Wavelet transformed single trial ERPs in response to different stimuli were distinguished by CPD in a motor imagery task [127] and in case of visual evoked potentials [132]. Recently, the trial mode in the CPD decomposition of $channel \times time \times trials$ tensor was used to accurately classify different stimulus types in a visual detection task [223]. However, single trial ERPs in response to the same stimulus show large variability compared to grand average ERPs, due to physiological modulation and to low signal to noise ratio. Considering that BTD is able to capture more variability in one term, we believe that it could improve single-trial ERP classification as well.

Chapter 6

Localisation of the seizure onset zone based on fMRI

In the previous chapter we introduced a novel methodology to extract the ictal source from noisy EEG signals in order to help delineate the SOZ. Although the current procedure in presurgical evaluation heavily relies on it, identification of the SOZ based on ictal EEG is a time consuming procedure, as seizures occur rarely. Seeking an alternative, many researchers have been investigating the utility of localising the irritative zone with EEG correlated fMRI analysis. However, as discussed in section 2.4.2, EEG-fMRI studies often fail due to the absence or unsuccessful marking of interictal spikes during the EEG-fMRI recording. In [106] we presented a proof of concept, namely, we demonstrate that ICA is capable of extracting sources related to epileptic activity even in patients where no interictal spikes were seen in the EEG. More particularly, these epileptic sources were shown to be capable of pinpointing the SOZ. This study is recapitulated in section 6.1. In order to utilise this approach in clinical practice, the epileptic source has to be identified blindly. In section 6.2 we introduce a method to automatically select the epileptic independent component.

6.1 Extracting epileptic sources using ICA

6.1.1 Introduction

Functional magnetic resonance imaging (fMRI) combined with simultaneously recorded electroencephalogram (EEG) is a powerful multimodal approach, which potentially provides information with high spatial and temporal resolution. It has been extensively used for characterizing cognitive processes, e.g. [54, 143]. It is capable of localizing ictal, e.g.[206] and interictal epileptic activity, e.g. [80, 177] and can be applied as part of presurgical evaluation [234].

As EEG-correlated fMRI studies often fail due to insufficient EEG information, there is a strong demand for data-driven techniques capable of analysing fMRI time series. Relying on the assumption that the sources generating the measured BOLD signals are mutually statistically independent in space, ICA has been successfully used in numerous fMRI studies.

ICA was first proposed to process fMRI data by [141]. It has been widely used to explore resting state networks (RSNs), e.g. [217], task-related activations, e.g. [24], or to characterize the variability of the hemodynamic response [61]. In [48] a method was developed which automatically classifies the independent components (ICs) extracted from the fMRI time series as BOLD related, artefactual or noise related using IC-fingerprints constructed by 11 features.

ICA has also been applied to the fMRI time series recorded from epilepsy patients during ictal [129, 131, 206] and interictal [129, 146, 173] period. The ICs were automatically grouped [173, 206] using the technique presented by [48]. Within the BOLD related class the epileptic ICs were identified based on spatial accordance with the seizure onset zone defined on intracranial EEG recordings or with the GLM EEG-fMRI activation maps and temporal correlation with the EEG-derived temporal regressor. Successful identification of the epileptic activity showed the potential of ICA in analysing fMRI time series of epilepsy patients.

In summary, several studies have demonstrated that ICA can reveal BOLD sources related to epileptic activity. In all these works the selection of the component of interest relied on the known timing of the epileptic events. However, the application of ICA is of particular interest in those cases where no epileptic events can be identified during the recordings, consequently, an alternative to the traditional GLM based approach is needed. Therefore, the present study primarily focuses on focal epilepsy patients in whom no ictal or interictal activity could be identified on the EEG. Our aim is to demonstrate

that ICA can estimate a component related to the epileptic network in such cases as well. We retrospectively identify the epileptic component based on its spatial correspondence to the known localization of the SOZ. To validate our findings, we analyse the data of a group of control subjects to investigate whether component maps resembling the SOZ exist in healthy individuals.

6.1.2 Materials and Methods

Data acquisition and preprocessing

A total of 28 patients were included in this study based on the following criteria: (1) consecutive adults who underwent a full presurgical evaluation for refractory focal epilepsy between August 2010 and January 2012, including seizure history, neurological and physical examination, interictal and ictal scalp EEG-recordings, video-analysis of seizures, high-resolution MRI of the brain, interictal and ictal single-photon emission computed tomography (SPECT) and subtraction ictal SPECT co-registered to MRI (SISCOM), neuropsychological assessment, and when available interictal ^{18}F-fluorodeoxyglucose Positron Emission Tomography (^{18}F-FDG PET) and intracranial EEG-recordings; and (2) concordant data pointing to one epileptic focus using all presurgical investigations. For clinical details of the patients, see patients 1-28 in the table shown in Appendix B. The ictal onset zone was defined as follows. In 11 patients who underwent epilepsy surgery with successful outcome (ILAE classification 1-4), we considered the region of ictal hyperperfusion, determined by SISCOM, inside the resection zone as the SOZ. The hyperperfusion on SISCOM was thresholded with $z > 1.5$. This threshold was shown to be optimal for localizing the epileptogenic zone [156]. In patients, planned or ineligible for surgery because the epileptogenic zone was within eloquent cortex, the SOZ was determined as the SISCOM hyperperfusion cluster ($z > 1.5$) in a manually outlined hypothetical resection area, based on multidisciplinary clinical consensus using all noninvasive and invasive data except EEG-fMRI results. Note that an injection delay of less than 20s was shown to correlate with correct localization [128], whereas the median injection delay was 16.5s in our dataset. In cases where injection delay and propagation did occur, visual recognition of so-called "hourglass" patterns helped differentiate between onset and propagation areas [62]. Nevertheless, by confining the SOZ to the hyperperfusion region inside the actual or hypothetical resection zone, we avoided the inclusion of hyperperfusion clusters corresponding to areas of propagated ictal activity. Multimodal concordant seizure focus localizing data increase the likelihood of benefit from surgical treatment [123, 125, 191]. Since

patients were selected for concordant localizing data, we ensured not to rely on a single testing modality.

BOLD fMRI data were acquired in the selected patients using a 3T MR scanner (Intera or Achieva, Philips) with a whole brain single-shot T2* gradient-echo Echo Planar Imaging sequence (TE = 33ms, TR = 2.2-2.5s, voxel size 2.6×3×2.6 mm). The images were realigned, slice-time corrected, normalized to MNI space and spatially smoothed with an isotropic Gaussian kernel of 6 mm full width at half maximum using SPM8 software (Wellcome Department of Cognitive Neurology, London, UK). Scalp EEG was simultaneously recorded with a 64 or 32 channel MR-compatible EEG cap (Brain Products, Munich, Germany) or a 24 channel electrode set (Ives EEG solutions inc). The EEG signals were amplified (BrainAmp amplifier, sampling rate 5000 Hz, resolution $0.5\mu V$) and transmitted outside the scanning room. From each patient 2 to 4 sessions were recorded, which lasted on average 12 minutes, ranging from 10 to 22 minutes each. The patients were asked to rest with closed eyes. The EEG was band-pass filtered offline between 1 and 50 Hz, using windowed sinc FIR filters with a Hann window, gradient artefacts were removed using a realignment-parameter informed template subtraction algorithm ([148], Bergen plug-in for EEGLAB, Bergen fMRI Group, Bergen, Norway), and BCG artefacts were subtracted using a dynamic average artefact template subtraction method ([5], Brain Vision Analyzer software, Brain Products, Munich, Germany). After artefact correction, interictal epileptic spikes, if present, were visually marked by a neurologist based on the EEG. Interictal epileptic activity was identified in 13 out of 28 patients. Clinically concordant interictal spikes were marked in 11 out of 28 patients during the EEG-fMRI recordings. Additionally, in 3 cases, contralateral or bilateral spikes (patient 14, 19 and 26) and in 2 cases pathological slow wave activity were identified (patient 10 and 24).

Functional images were also acquired from 12 healthy controls (4 male, 8 female, age range 21-56, mean age 34.4) using the same protocol and preprocessing as described above.

Scans recorded during large movements of the patients and controls were discarded: the largest consecutive series of scans were retained where the momentary displacement did not exceed 1mm. Additionally, movement related effects were estimated by constructing nuisance regressors based on the realignment parameters, were fitted to the fMRI time series using SPM8, and were finally regressed out from the fMRI time series. A combined gray and white matter mask obtained in SPM8 was applied to remove voxels within cerebral spinal fluid structures and resected lesions.

Independent component analysis of fMRI time series

The measured fMRI time series is the result of the mixture of ongoing neural activity, artefacts and noise. Assuming that the activity of interest has a fixed spatial pattern which is independent of the ones related to other underlying processes, ICA separates them in the following way:

$$U = VZ, \tag{6.1}$$

where $U \in \mathbb{R}^{n \times m}$ is formed by the component voxel values where n is the number of independent spatial components, which equals the length of the time series, and m is the number of voxels. $Z \in \mathbb{R}^{n \times m}$ contains the measured fMRI time course of all voxels and $V \in \mathbb{R}^{n \times n}$ is the unmixing matrix. The columns of the mixing matrix $M = V^{-1}$ are the time courses associated with each IC. In such formulation, the ICA of the fMRI will deliver as many independent components as the number of samples in the time series. However, the data usually can be explained by a smaller number of underlying processes. In order to reduce the number of components, the temporal dimension of each time series is reduced by principal component analysis to an estimated optimum. The optimal number of ICs was estimated automatically for each session of each patient using the minimum description length (MDL) criteria ([172], as implemented in the GIFT toolbox (http://www.nitrc.org/projects/gift/). For each patient and control, the maximum of the optimal number of ICs over all sessions were taken, resulting in 53.3 ± 13.1 components across the individuals. Individual sessions were first reduced in dimension, then concatenated into an aggregate dataset and reduced again to obtain the optimal dimension. Subsequently, independent component analysis was performed on each aggregate dataset using the infomax algorithm [10]. Spatial maps and time courses of individual sessions were backreconstructed using the aggregate mixing matrix [23]. Finally, the mean spatial map over all sessions were considered for each patient and control.

Identification of the epileptic IC

In order to identify ICs corresponding to the epileptic network, the procedure below was followed. The component voxel values were converted to z-scores by extracting the mean and dividing by the standard deviation of all voxel values within the component map. A threshold of $z > 5$ was used to create component

activation maps. Finally, the component activation maps were ordered based on their overlap with the SOZ.

$$ovl^{(i)} = \frac{v_{SOZ} \wedge v_{IC}^{(i)}}{v_{SOZ} \vee v_{IC}^{(i)}}, \tag{6.2}$$

where v_{SOZ} and $v_{IC}^{(i)}$ denote the set of voxels within the SOZ and the set of suprathreshold voxels of the i^{th} IC, respectively. Note that suprathreshold voxels may occur at several distant regions in the brain, i.e. various distant groups of adjacent suprathreshold voxels will form various activation clusters throughout the brain.

The high threshold of $z > 5$ was chosen in order to achieve high specificity and omit ICs which show negligible overlap with the SOZ. Note that the overlap measure defined here is symmetric, unlike others used in the literature (e.g. considering an overlap larger than 10% of the extent of GLM-activation map a match [173]). As such, our measure is not sensitive to the chosen threshold for the IC maps: lowering the threshold increases the extent of the overlap but increases the set of activated voxels outside the SOZ as well. We will consider an overlap large if its value exceeds 5%. As the average extent of the SOZ over all patients was approximately $5 \cdot 10^3$ voxels, the average number of suprathreshold voxels in the ICs was $2 \cdot 10^3$ and the total number of voxels after masking out CSF structures exceeds $2 \cdot 10^5$, an overlap larger than 5% is unlikely to occur by chance.

ICs showing a significant temporal correlation ($p < 0.01$, corrected for multiple comparisons using Bonferroni's method) with the realignment parameters and showing spatial patterns such as outstretched activation clusters along the surface of the brain or several scattered clusters, assessed by visual inspection, were considered as head movement related artefacts and were excluded. The remaining sources, which overlap with the SOZ, are candidate ICs, i.e. potentially related to epileptic activity. Finally, the candidate IC showing the largest overlap with the SOZ will be called the epileptic IC (eIC).

Validation with control subjects

In order to assess the risk of finding false overlaps (coincidental overlap with an IC which is not related to epileptic activity), the overlaps between the ICs of each control and the SOZ of each patient were analysed. For each SOZ, the IC showing the largest overlap with it was selected from each control. The values of these overlaps (28 times 12 values in total) were then averaged to obtain

an expected false overlap extent for each of the 28 SOZ. The expected false overlap extents were then compared to the overlap between the SOZ and the eIC in the corresponding patient.

Analysis of the eIC time course

For the 13 patients who showed interictal activity during the fMRI recordings, the timing of the epileptic events were compared to the time courses of all ICs. Reference BOLD time courses were created by convolving the timing of epileptic events with the canonical hemodynamic response function.

6.1.3 Results

Description of the epileptic ICs

Figure 6.1 shows the extent of overlap between the ICs and the SOZ for each patient. If the voxel with maximal z-score belongs to the cluster which overlaps with the SOZ, the IC is marked with a filled green circle. If the voxel with maximal z-score belongs to another cluster, the IC is marked with an empty circle. ICs which are significantly correlated to the timing of the epileptic activity are marked with an outer black circle additionally. ICs corresponding to movement artefacts are marked in red. Figure 6.2 shows the example of patient 12, a case without interictal spikes recorded in the EEG, where several different ICs showed large overlap with the SOZ. However, only one of them is considered to be a candidate IC, as the others are due to movement related effects. The eIC of each patient, selected as the IC showing the largest overlap with the SOZ from the candidate ICs, is marked with an arrow on Figure 6.1.

The average overlap between the eIC and the SOZ is 10.6% ± 7.2, more particularly, 12.5%±7.0 and 9.60%±7.1 for patients with and without interictal activity, respectively. The difference between the patient groups is insignificant (p=0.19, F-test). Figure 6.3 shows 2 examples, patient 11 and patient 27, where no interictal spikes were present in the EEG. In both cases the eIC shows an extensive overlap with the SOZ, and the voxel with maximal z-score is within the cluster overlapping with the SOZ.

The location of the voxel with the maximal z-score is particularly important from various aspects. First, a spatial map might consist of various activation clusters, however, the extent and the number of these clusters are threshold dependent, unlike the location of the voxel with the maximal z-score. Therefore, if the voxel with the maximal z-score belongs to the cluster overlapping with

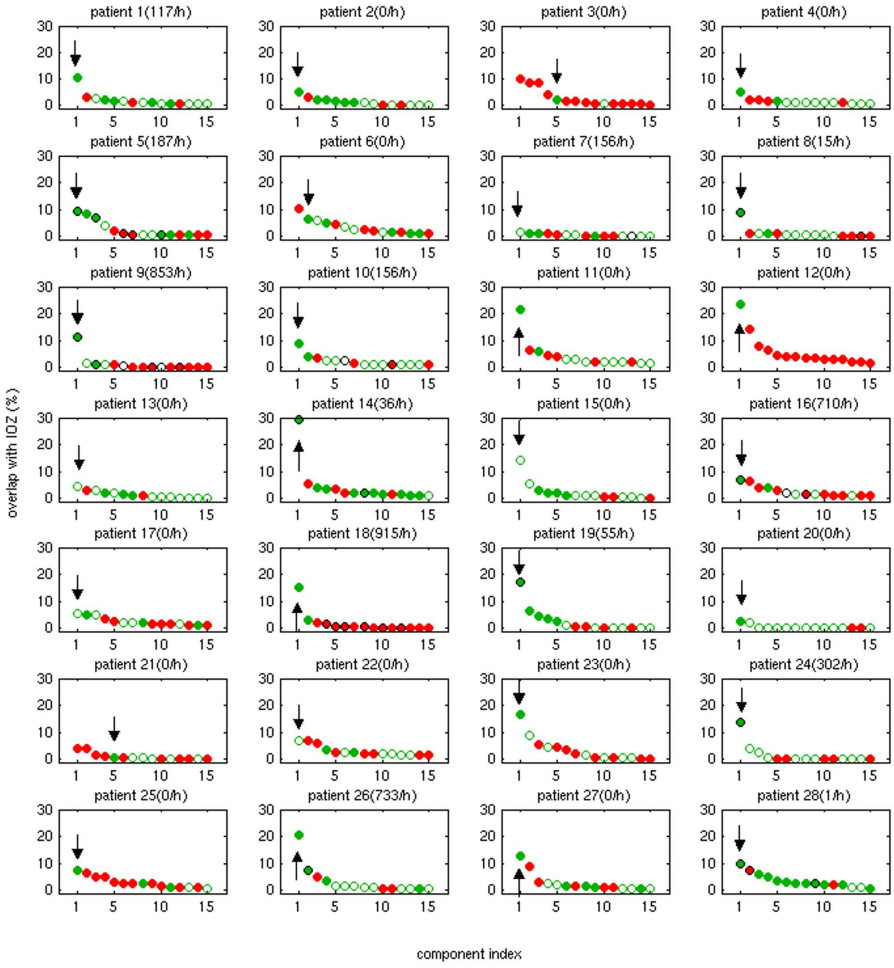

Figure 6.1: The extent of overlap of ICs with the SOZ for each patient. The number of spikes marked on the EEG inside the scanner is indicated in brackets next to the patient number. For each patient 15 ICs with the highest overlap are plotted in descending order. The eICs are indicated with an arrow. If the voxel with maximal z-score belongs to the cluster which overlaps with the SOZ, the IC is marked with a filled green circle. If the voxel with maximal z-score belongs to another cluster, the IC is marked with an empty circle. ICs resembling movement artefacts are marked in red. ICs which are significantly correlated to the timing of the epileptic activity are marked with an outer black circle additionally.

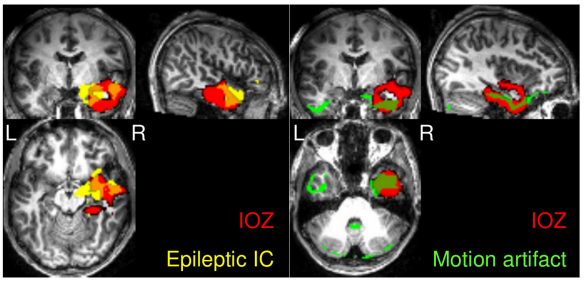

Figure 6.2: In several patients multiple ICs overlapped with the SOZ. Here the example of patient 12 is shown. The IC marked with green is a head movement related artefact, its time course showing significant correlation to the realignment parameters. Therefore, only the IC marked in yellow is considered to be a candidate eIC. Note the extensive overlap (23%, marked in orange) with the SOZ (marked in red) and that in this patient no interictal spikes where recorded in the EEG.

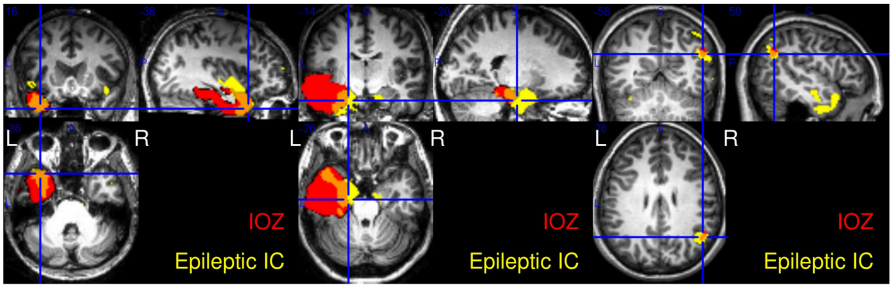

Figure 6.3: Examples of patients, in whom no interictal spikes were recorded in the EEG. Patient 11 and patient 27 (left and middle): in both cases the eIC (in yellow) shows large overlap (in orange) with the SOZ (in red), 22% and 13%, respectively. Patient 20 (right): Despite the quantitatively small overlap, the eIC is highly informative with respect to the SOZ. In all three cases the voxel with maximal z-score, indicated by the crosshair, is within the cluster overlapping with the SOZ.

the SOZ, the assumption that the selected eIC is really epileptic gains further support. Furthermore, it shows that these eICs are informative with respect to the SOZ, i.e. if in a future application the eIC is selected automatically, the voxel with the maximal z-score indicates the SOZ.

The cluster within the eIC which overlaps with the SOZ contains the voxel with the largest z-score in 23 out of 28 patients. In patients 13 and 17 with temporal lobe epilepsy the eIC is a symmetrical bitemporal activation map, where the voxel with the maximal z-score is in the contralateral temporal lobe. The eICs of patients 7, 15 and 22 the eIC are contaminated with movement artefacts, which showed correlation with the realignment parameters below significance level. However, in all patients, even if it does not hold for the eIC, there exists a candidate IC, where the voxel with the largest z-score is within the cluster overlapping with the SOZ.

The eIC shows small (i.e. $< 5\%$) overlap with the SOZ in 5 patients (patients 3, 7, 13, 20 and 21). Figure 6.3 shows such an example, the eIC and its overlap with the SOZ of patient 20. Despite the quantitatively small overlap, the IC is highly informative with respect to the SOZ. Similarly, in patient 3 and 21, where the voxel with the maximal z-score is within the overlapping cluster, the eIC is indicative of the SOZ. Note that in patients 7 and 13 there is a small overlap between the eIC and the SOZ, moreover, the voxel with the maximal z-score is not indicative of the SOZ.

Validation with control subjects

The extent of the overlap between the SOZ and the eIC, $10.6\% \pm 7.2$ on average, was significantly larger than the expected false overlap, $5.6\% \pm 2.4$ on average ($p < 10^{-3}$, Wilcoxon signed rank test). However, control ICs showed a larger overlap than patient ICs in 7 out of 28 cases, in patients 3, 7, 13, 16, 17, 21 and 25. In patients 16 and 25 the SOZ is in the mesial frontal cortex and right frontal cortex close to the midline, respectively. In controls a map resembling the resting state network related to executive control [9] was consistently found, which showed large overlap with the SOZ of these patients. In the other 5 cases the eIC showed small (i.e. $< 5\%$) overlap with the SOZ or the voxel was not indicative to the SOZ. The question raises, whether the epileptic network was inactive in these patients, or ICA failed to extract it correctly.

In order to make sure that the significant difference in overlap between patients and controls above was not due to some confounds, further tests were performed. First, the above procedure was repeated after excluding 6 patients who had surgical lesions, resulting in significantly larger overlap between patient ICs and SOZ ($p < 10^{-3}$). Second, the 12 controls were gender and age-matched to

12 patients and the overlaps of patient ICs were compared to the overlaps of the corresponding control ICs. Patient ICs overlapped significantly more with the SOZ ($p < 10^{-2}$). Finally, the severity of the patients' and controls' movements was compared based on the realignment parameters. There was no significant difference between the maximal displacement of patients and controls.

In summary, patient ICs showed a significantly larger overlap with the SOZ than control ICs did on the group level. On the individual level, in 75 % of the cases an eIC was found which showed larger overlap with the SOZ than the extent of a coincidental overlap.

Analysis of the eIC time course

ICs showing significant correlation with the epileptic activity are marked with a black outer circle on Figure 6.1. The time course of the eIC was significantly correlated to the reference BOLD signal in 6 cases, and significantly anticorrelated in 2 cases. Interestingly, in most cases more than one IC showed significant correlation with the regressor. Several components exist which are significantly correlated both to the epileptic events and to head movement.

Although our definition implies that there is exactly one eIC per patient, there might exist multiple meaningful components. Both spatial overlap with the SOZ and temporal correlation to the interictal epileptic discharges were found in multiple ICs in several patients.

In case of patient 14 one IC shows a lateralised, the other a bilateral activation (see Figure 6.4). On the EEG of this patient both left sided and right sided spikes were marked. IC # 36 has a left lateralised activation map and its time course is significantly correlated to the reference BOLD signal derived from the left sided spikes and anticorrelated to the one derived from the right sided spikes ($p = 1 \cdot 10^{-4}$ and $p = 0.02$, respectively), while IC # 24 has a bilateral activation map and its time course is significantly correlated to reference BOLD signal derived from the left sided spikes ($p = 4 \cdot 10^{-6}$). This suggests that the different ICs correspond to 2 different aspects of epileptic activity, which only partially overlap.

6.1.4 Discussion

Several studies have shown the clinical usefulness of EEG-fMRI in localising interictal epileptic activity in the brain. The main disadvantage of this

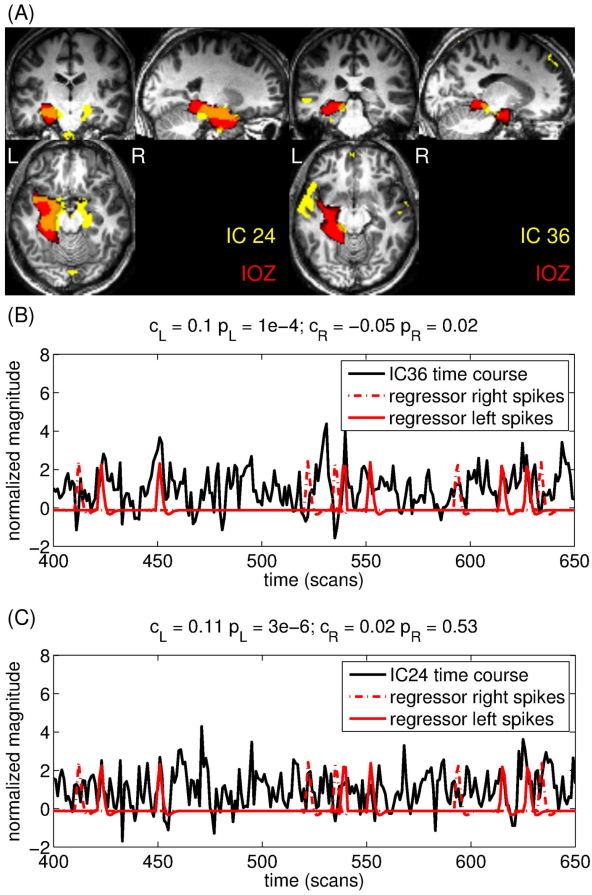

Figure 6.4: There are 2 ICs showing extensive overlap with the SOZ in patient 14. (A.) Left: IC # 36 has a left lateralised activation map and its time course (B.) is correlated with the reference BOLD signal based on the left-sided interictal spikes and anticorrelated to the regressor based on the right-sided spikes. (A.) Right: IC # 24 has a bilateral activation map and its time course (C.) is correlated with the reference BOLD signal based on the left-sided interictal spikes. For better visualization, only a short segment of the time courses are shown. The correlation coefficients and the significances are shown above the graphs.

technique is that it relies on the timing of epileptic activity as read on the EEG, which is, in a majority of the cases, not available or not reliable.

We apply a data-driven methodology, namely ICA, which can estimate neural sources purely from the fMRI data without any information on the temporal pattern of their activation. Our aim was to demonstrate that a source related to the epileptic network exists among the components extracted by ICA. It has been shown previously by [173] that ICA can find epileptic sources, where the time course of the epileptic source is correlated to the timing of epileptic events, and the spatial map is similar to the GLM-based activation map. To our knowledge, it is shown here for the first time that the epileptic network can be found with ICA even in patients where no ictal or interictal activity was present on the EEG during the fMRI recordings. This result suggests that the epileptic network is continuously active in the brain even if it is invisible on the EEG.

The epileptic source was selected from all the estimated components based on spatial overlap with the a-priori known SOZ. The identification involved an arbitrary $z < 5$ threshold on the spatial maps. Varying this threshold, however, had limited influence on our main findings. Components related to head motion artefacts were excluded prior to the selection of the candidate epileptic components. Several other types of artefacts were described in the literature and were recognized among our components. Due to the lack of available tools these components were not excluded automatically. Visual inspection nevertheless confirmed that the selected epileptic components were not originated from artefacts.

Additionally to the spatial overlap with the SOZ, we demonstrated in several other ways that the selected eIC is truly epileptic. The voxel with the maximal z-score belonged to the cluster overlapping with the SOZ in 23 out of 28 cases, i.e. the selected component is not a threshold dependent coincidental overlap. This is especially relevant information in those cases, where the overlap between the eIC and the SOZ was small ($< 5\%$). Considering this aspect, the criteria for selecting the eIC could be redefined in the following way: eIC is the candidate (not artefact related) IC showing the largest overlap with the SOZ where the overlap is at least 5% or the overlapping cluster contains the maximal z-score. These alternative criteria would select different eICs only in 2 patients, hence, this does not have an implication on our main findings. As further validation, we showed that eICs extracted from patient data overlap significantly better with the SOZ than ICs extracted from healthy individuals. Finally, in the majority of cases where interictal activity was reliably identified on the EEG, the eIC time course correlated with the timing of this activity. Although it has been reported in the literature that an epileptic IC with both spatial correspondence and significant correlation with epileptic activity was found

in up to 90% of focal epilepsy patients, in these studies the patient group was preselected for concordant GLM-fMRI results. In the current study no such preselection was made. Simultaneous non-invasive and invasive recordings [32] have provided evidence that many spikes recorded with invasive techniques can not be detected with surface electrodes. Therefore, we argue that components showing high overlap with the SOZ might reflect a certain type of epileptic activity in EEG-negative and non-correlated cases as well, despite the fact this activity is invisible oni EEG.

As our aim was to demonstrate the existence of an IC informative of the SOZ, we selected, by definition, one eIC. However, note that in some patients multiple candidate ICs were found showing extensive overlap with the SOZ, which are potentially all meaningful. Similarly, it has been reported, that ICA finds multiple components corresponding to the same functional network [36, 117] in resting state fMRI. The question arises whether in such cases the same network is captured partially by various components, or the components reflect actually different underlying neurophysiological processes. In most cases multiple ICs correlated with the spike-derived regressor, including ICs which showed no or negligible overlap with the SOZ. This might mean that the onset and propagation zones are separated in different components. In case of one patient it was possible to match the different epileptic fMRI components to partially different types of electrophysiological interictal activity. A thorough analysis including all patients should be carried out to further investigate this aspect. Furthermore, in patients where the eIC showed small overlap with the SOZ, it is uncertain whether the epileptic network was inactive, or ICA failed to decompose it correctly. This ambiguity is an inherent limitation in data-driven methods.

Our ICA procedure is not an automatic identification method, as the epileptic source was chosen retrospectively, according to the known localization of the SOZ. Nevertheless, assuming that the epileptic network can be selected automatically, the voxel with the maximal z-score could identify the cluster overlapping with the SOZ. In our database the vast majority of patients had an eIC in which the voxel with the maximal z-score belonged to the cluster overlapping with the SOZ. Note that all patients had at least one candidate IC with such property, and these ICs are all potentially useful for identifying the SOZ. This implies that ICA of fMRI could facilitate the identification of the SOZ even in EEG-negative patients. Therefore, it has the potential to extend the applicability of fMRI assisting presurgical evaluation in epilepsy.

6.2 Automatic selection of epileptic fMRI sources

The proof of concept study presented in the previous sections serves as a motivation for future research. We have proven in a retrospective manner that ICA can extract sources related to the epileptic network. Moreover, in the majority of cases these sources substantially overlapped with the SOZ. The goal of the current section is to develop a prospective technique which can automatically select the epileptic fMRI source. Ultimately, such a technique could identify the SOZ based on fMRI, blinded to all other clinical information and imaging modalities.

6.2.1 Introduction

A few studies have already presented promising approaches in this direction applying a variety of model based and/or data-driven techniques.

One group of methods aims at extracting meaningful information from the simultaneously recorded EEG without recurring to the identification of epileptic events per se. In [84] EEG voltage maps were created by averaging interictal epileptiform discharges recorded during long-term clinical monitoring outside the scanner. Subsequently, the correlation of this map with the EEG recordings inside the scanner was computed for each time frame. The time course of this correlation coefficient was used as a regressor for fMRI analysis to map hemodynamic changes related to these epilepsy-specific maps. The method revealed concordant activation maps in 78% of the cases with previously inconclusive EEG-fMRI results. However, it was shown recently that this method yields low specificity [212]. The same study proposed an improved methodology, where both the morphology and the topography of the spike template is taken into account when constructing the regressor. Their approach reached a high specificity of 90%, although at the cost of lower sensitivity. Alternatively, [129] computed spectral metrics from independent components extracted from the EEG recorded inside the scanner. These spectral metrics express different transfer function models between EEG and BOLD signals. The resulting time courses are convolved with a canonical HRF and used as regressors of interest in a GLM analysis of the fMRI data. The advantage of this approach lies within providing insight into the link between neuronal and hemodynamic signals.

Another emerging group of approaches analyse solely fMRI data and do not require the simultaneous recording of EEG. Temporal clustering analysis (TCA, [150]) and its improved version, 2dTCA, [149] was developed to detect multiple activation patterns of irregular, transient behavior. Recently, activelets, a new

wavelet dictionary matching BOLD characteristics was developed [115]. The activelets are constructed based on the linear approximation of the balloon model [22] of the hemodynamic response function (HRF). As the activelet waveforms follow the shape of the BOLD response of a transient neural activation, such transient activity will be sparsely represented in the activelet basis. The timing of transient, sparse neural activity can be estimated using a convex optimization algorithm. [137] applied activelets to detect transient activations related to epileptic spikes on each voxel time course, and used spatiotemporal clustering to gather voxels showing similar timing of activity. The cluster with the sparsest temporal activation pattern was selected as epilepsy related. Both the TCA and the activelet based methods showed promising results in simulation studies, however, only limited validation on EEG-negative patient data was performed.

The work presented here is motivated by the findings of section 6.1, namely, that ICA is capable of extracting epileptic sources even in patients where no interictal spikes were seen on the EEG. For a prospective use of ICA to identify epileptic activity on the fMRI, an automatic technique for selecting the eIC is required. In study presented in [48] the authors developed 11 features distinguishing BOLD related ICs from non-BOLD related, artefactual ICs. Recently, a similar approach has been developed which utilises a much wider range of features and combines various classification approaches via classifier stacking [178]. The method in [48] was used successfully by [173] to reduce the number of potential epileptic ICs. However, the epileptic IC best resembling the GLM-based activation maps was visually selected from this reduced set.

This section introduces a method which aims at fully automating this procedure, by characterizing the eICs revealed by our approach and to develop new features distinguishing epilepsy related ICs from other BOLD related sources. We developed our approach based on a set of patients, where interictal spikes did appear on the EEG, so that GLM-based EEG-fMRI activation maps can serve as a ground truth for the blind identification method.

6.2.2 Data collection

For the purpose of this study data from focal epilepsy patients were used, who underwent presurgical evaluation between August 2010 and November 2013. Data acquisition and inclusion criteria were the same as explained above in section 6.1.2, with an extra constraint that the GLM-based EEG-fMRI activations maps were concordant with all other clinical information. This constraint was necessary in order to make sure that the fMRI data is of sufficient quality and indeed contains epileptic activity patterns informative to

the SOZ. Furthermore, in order to avoid inconsistencies in the data which might bias the method, only patients with identical recording parameters (TR=2.5s) were included. Finally, one recording session was selected arbitrarily from each patient. This way the final dataset consisted of the interictal fMRI time series of 10 patients: patient 9, 10, 26, and 29-35 in the table shown in B.

In addition, fMRI data from 13 healthy individual were included in this study as well in order to assess the behaviour of the proposed method in the absence of pathological activity.

A detailed description of the data and the results of the GLM-based EEG-fMRI analysis is described in [212].

6.2.3 Blind selection method

A flowchart depicting the various steps involved in the proposed algorithm is shown in figure 6.5.

First, ICA is performed on the fMRI time series. Consecutively, a cascade of classifiers is applied: after discarding artefact related ICs in the first classification step, the epileptic ICs are selected from the remaining reduced set of BOLD related ICs using the second classifier. Finally, localisation information is retrieved from the spatial map corresponding to the epileptic ICs.

The ICA step and the discrimination between BOLD and artefact related ICs, together with the corresponding feature extraction was performed using the Fix plug-in of the FSL toolbox (`http://fsl.fmrib.ox.ac.uk/fsl/fslwiki/FIX`). Within this approach the temporal and spatial characteristics of the ICS are described by over 180 features. Multiple different classifiers are utilised, which are combined via classifier stacking. Detailed explanation about the extracted features and the applied classification technique is available in [178]. The contribution of this thesis is the development of the features and the classifier for the second discrimination step in the cascade.

Feature extraction

The aim of this study is to automatically select epileptic independent components. In section 6.1.4 we argue that there might be multiple ICs corresponding to partially overlapping parts of the epileptic network, reflecting different aspects of epileptic activity. However, considering that the automatic recognition of an epileptic IC corresponding to the SOZ would be the clinically

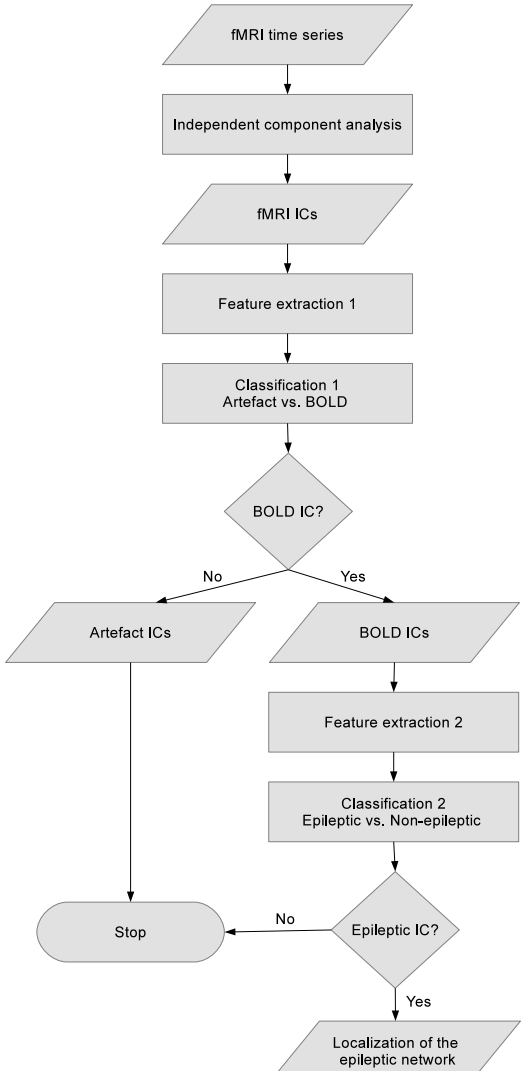

Figure 6.5: The proposed algorithm for automatic localisation of the SOZ involves several steps. First, ICA is performed on the fMRI time series. Consecutively, a cascade of classifiers is applied: after discarding artefact related ICs, the epileptic ICs are selected from the remaining reduced set of BOLD related ICs. Finally, localisation information is retrieved from the spatial map corresponding to the epileptic ICs.

most relevant finding, we concentrate on characteristics which are peculiar to such ideal components. Therefore, the following features were extracted from the fMRI ICs.

Number of clusters. Suprathreshold voxels in the spatial map corresponding to an IC are spatially organised in one or more clusters. We only take into account clusters which comprise at least 30 suprathreshold voxels. The number of activation clusters in an epileptic IC is ideally 1, corresponding to the ictal onset zone. In contrast, various RSNs consist of multiple active regions.

Activation asymmetry. The ictal onset zone of a unifocal epilepsy patient is restricted to a region in strictly one hemisphere, thus will show asymmetry. The activation asymmetry of an IC is assessed by the following formula:

$$AA = |\sum_{i=1}^{H} v_i^{(l)} - v_i^{(r)}|, \tag{6.3}$$

where $v_i^{(l)}$ denotes the i^{th} voxel in the left hemisphere, $v_i^{(r)}$ denotes the corresponding contralateral voxel and H is the total number of voxels in one hemisphere.

Sparsity in activelet basis. Activelets are a recently developed dictionary of wavelet basis functions [115], which has been applied to detect interictal epileptic activity from fMRI [137]. The activelet waveforms were specifically constructed to fit the BOLD signal in response to a sparse transient event. Therefore, the representation of a time course constituting sparse transient events, such as interictal epileptic spikes, will be sparse in the activelet basis.

The neural activity of interest consists of k interictal epileptic spikes with amplitudes A_k and onsets t_k. The fMRI measures the BOLD signal changes as a result of this neural activity. The hemodynamic system linking the neural activity to the BOLD signal is denoted by h, and is commonly assumed to be linear and shift-invariant. The BOLD signal recorded by the fMRI can be written as follows:

$$y(t) = \sum_k A_k h(t - t_k) + \epsilon(t), \tag{6.4}$$

where $\epsilon(t)$ is an unknown noise term comprising noise, baseline, drifts, physiological artefacts and possibly other unrelated neural activity. The goal is to recover the activity of interest from the noisy signal. Given that the neural events are sparse in time, the linearity assumption holds and the transient BOLD signals can be sparsely represented in the activelet basis. Let

ϕ be the overcomplete dictionary matrix containing the basis functions of the undecimated activelet transform. Then the estimated neural activity x will be given by $x = \phi\beta_0$, where β_0 is the solution of the convex l_1 optimization problem:

$$\min_{\beta}(\frac{1}{2}\|y - \phi\beta\|_2^2 + \lambda\|\beta\|_1) \tag{6.5}$$

The regularization parameter λ controls the trade-off between the sparsity of the solution and the reconstruction error, a higher value favouring a sparser solution. The value of λ was set to 2.5 in this study. ϕ is a matrix of size $T \times P$, where T is the length of the time series and $P = 3 \cdot T$ as the number of wavelet decomposition scales was set to 3 [137]. The minimization problem in 6.5 was solved by the Homotopy algorithm [60].

We have demonstrated the usefulness of activelets in characterizing the time course of ICs derived from the fMRI time series in [103]. The time course of an epilepsy related IC is expected to have a sparser representation in the activelet basis compared to non-related ICs. The sparsity of the representation in the activelet basis was quantified with the Gini index [108], which measures the statistical dispersion of the magnitude of the coefficients.

Sparsity in sine dictionary. In contrast, the time course of resting state networks is characterized by low-frequency (0.01-0.1 Hz) fluctuations [33]. As such, they have a sparse representation in a sine dictionary restricted to this frequency band. A matching pursuit algorithm was used to retrieve the coefficients corresponding to the best nonlinear approximation of the fMRI IC. Again, the sparsity was quantified using the Gini index.

Kruskal-Wallis tests were performed in order to assess whether the extracted features differentiate between epileptic and non-epileptic ICs. The distribution of the feature values are shown in Figure 6.6. The statistical significances are indicated in brackets. The difference of the number of clusters was marginally insignificant, while the other features were significantly different between the two groups.

Classification

A least-squares support vector machine (LS-SVM) classifier was applied to learn an optimal classifier based on the above extracted features. A linear kernel was chosen, and the kernel parameter was tuned using leave-one-component-out crossvalidation on the training data. Positive training examples, i.e. the class of epileptic ICs consisted of the ICs showing the largest overlap with the cluster

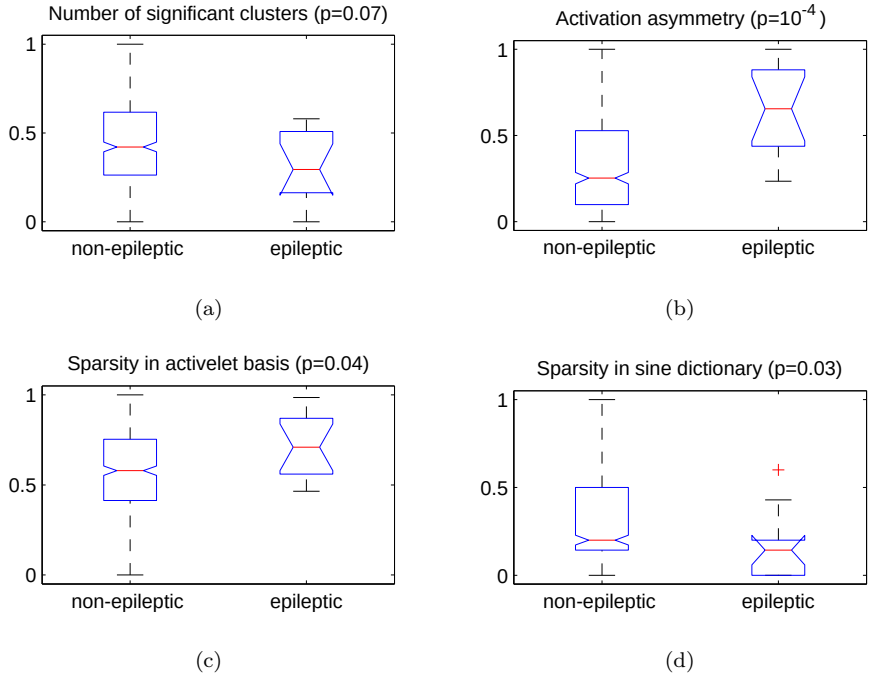

Figure 6.6: The features values significantly differ between the epileptic and non-epileptic ICs, except, the difference in number of clusters is marginally insignificant.

containing the maximally activated voxel in GLM-based fMRI activation map in each patient. In addition, ICs which showed at least 10% overlap with the same cluster and significantly correlated with the spike-derived regressor, were also included in the epileptic class. All other ICs were included as negative training examples, i.e. in the class of non-epileptic ICs.

Note that our final goal is to select an IC which overlaps with the SOZ, nevertheless, we prefer to define the training examples based on the GLM-based activation maps for the following reason. While the SOZ reflect ictal phenomena, in this study interictal processes were recorded in the fMRI. We do expect that the fMRI-based maps will contain the SOZ, but perfect overlap is unlikely. The GLM-based fMRI maps provide a more reliable image of how the epileptic ICs should look like.

Recall that LS-SVM takes decisions according to the following formula:

$$y(x) = \text{sign}(\mathbf{w}^T \varphi(\mathbf{x}) + b),$$

This formula might assign multiple ICs to the epileptic class, however, we are interested in selecting exactly one epileptic IC in each patient. Therefore, we modify decision as follows:

$$y(x_i) = \begin{cases} 1 & \text{if } \arg\max_{\mathbf{x}}(\mathbf{w}^T \varphi(\mathbf{x})) = i \text{ and } \mathbf{w}^T \varphi(\mathbf{x}) + b > 0 \\ 0 & \text{otherwise.} \end{cases} \tag{6.6}$$

This way at most one IC is selected in each patient. The values $\mathbf{w}^T \varphi(\mathbf{x})$ determine a ranking of the ICs, the highest value corresponds to the IC which resembles most of the eICs of the training data. In case this value exceeds the threshold $-b$, the first ranked IC is selected as epileptic. Otherwise, if no IC shows enough resemblance to the training eICs, no selection is made.

The performance of the proposed method was estimated in a leave-one-patient-out scheme: individual classifiers were trained for each patient using data from all other patients.

Evaluation measures

The voxel values in the spatial maps of the selected ICs were converted to z-score and thresholded at 5 in order to obtain activation maps. Afterwards, the overlap between the IC activation maps and the SOZ as well as the GLM-based EEG-fMRI activation map were assessed in each patient.

On one hand, an overlap with the GLM-based EEG-fMRI map indicates that the selected IC represents some aspect of the epileptic network. On the other hand, a method selecting an IC which overlaps with the SOZ would have real clinical significance.

Following the considerations made in [213], sensitivity and specificity of the proposed method for localising the SOZ were defined as follows.

Activation maps of the selected ICs overlapping with the SOZ were considered true positive cases. Patients where no IC was selected or no overlap was found were considered false negative cases. In order to define specificity, the data from healthy controls were analysed. Controls where no IC was selected or the selected IC contained no suprathreshold voxels were considered true negatives, and others false positives. Finally, sensitivity and specificity was calculated with the standard formula:

$$\text{Sensitivity} = \frac{\text{true positive}}{\text{true positive} + \text{false negative}} \tag{6.7}$$

$$\text{Specificity} = \frac{\text{true negative}}{\text{true negative} + \text{false positive}} \tag{6.8}$$

6.2.4 Results

An IC was selected in 7 out of 10 patients. These ICs, together with the SOZ and the GLM-based activation map of each patient are shown on Figure 6.7 in yellow, red and violet, respectively. Detailed qualitative analysis of the selected ICs are given in the figure caption. Below we quantitatively summarise the results.

In 6 out of these 7 cases the selected IC overlapped either with the SOZ or with the GLM-based EEG-fMRI activation map. Moreover, the cluster containing the maximally activated voxel overlapped either with the SOZ or with the GLM-based EEG-fMRI activation map in 5 out of 7 cases. These results indicate that the method is very selective for components related to the epileptic network.

However, an IC overlapping with the SOZ was selected only in 4 cases, i.e. the proposed method has a sensitivity of 40% for localising the SOZ. Looking at the cluster with the maximally activated voxel, the sensitivity drops to 30 %.

Nevertheless, the method selected an IC in only 3 controls out of 13, corresponding to a specificity of 77%. This suggests that the ICs selected in patients are truly related to epilepsy, despite of the low sensitivity of the method regarding the localisation of the SOZ.

The low sensitivity is partly explained by the fact that we insist on selecting one IC per patient. However, there are strong evidence that in some patients more than one epileptic IC is present. Patients 26, 29, 30 and 34 showed more than one type of IEDs in the simultaneously recorded EEG. While the GLM activation maps based on the preponderant spike type overlaps with the SOZ in most cases [213], BOLD activations corresponding to other spike types may be remote from the SOZ. In fact, the IC activation maps selected in patients 26 and 30 correspond to the field of the secondary spike type. The ICs concordant with the prepondent spike type, i.e. overlapping with the GLM-based activation maps, were ranked 3rd on average across all patients. This high average ranking suggests that ICs reflecting different aspects of epileptic activity compete for the first ranked position.

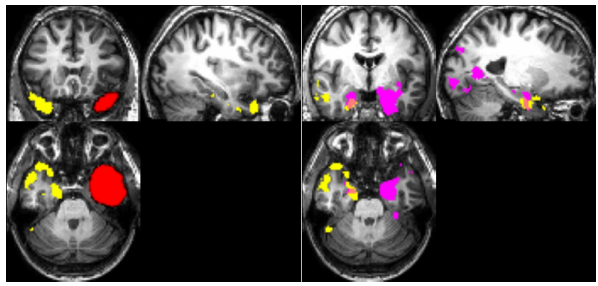

(a) Patient 26. The selected IC map shows an overlap with the GLM-based activation map in the temporal lobe contralateral to the SOZ. The patient had spikes both in the left and right temporal lobe. Hence, the selected IC is assumed to correspond to propagated epileptic activity.

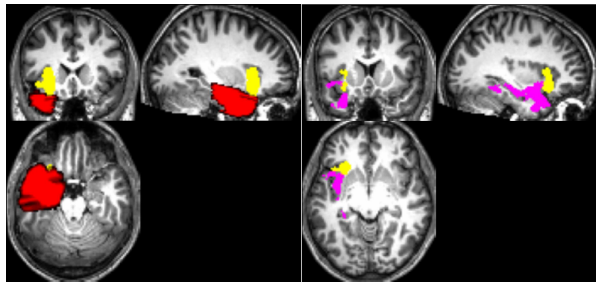

(b) Patient 29. The cluster containing the maximally activated voxel in the selected IC map shows a small overlap with both the SOZ and the GLM-based activation map. Moreover, the time course of the selected IC significantly correlates with the spike-derived GLM regressor.

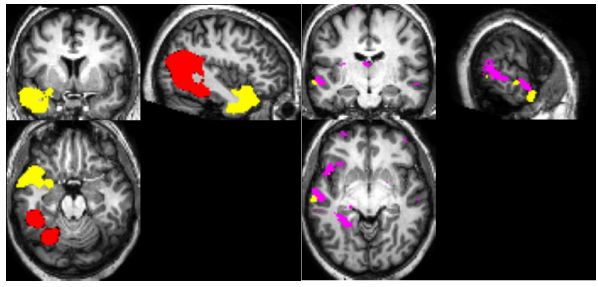

(c) Patient 30. The SOZ is located in the temporooccipital lobe. The GLM-based activation map consists of cluster in both the temporoccipital region and in the anterior temporal lobe. The cluster with containing the maximally activated voxel in the selected IC overlaps with the GLM-based activation map in the anterior temporal lobe. Further, the selected IC shows activated cluster in the occipital lobe as well, but not overlapping with the SOZ.

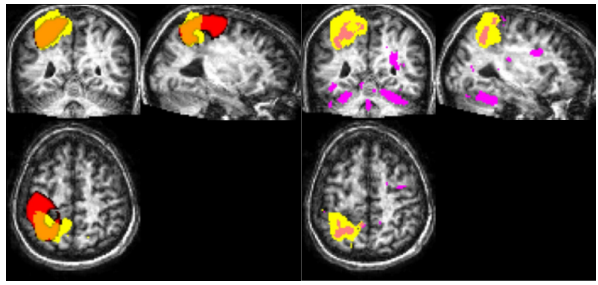

(d) Patient 31. The single activation cluster of the selected IC shows a clear overlap with both the SOZ and the GLM-based activation map. Note that while the GLM-based activation map shows a widespread epileptic network, the selected IC is specific to the SOZ. The significant correlation between the IC time course and the spike derived regressor provides further evidence for the the goodness of the selected IC.

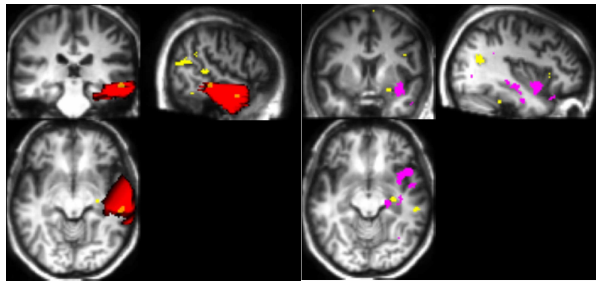

(e) Patient 32. The cluster containing the maximally activated voxel is located in the occipital lobe. Other small clusters are found in the temporal lobe where it overlaps with the SOZ. These clusters are in the vicinity of some clusters in GLM-based activation map, but they show no overlap at this threshold.

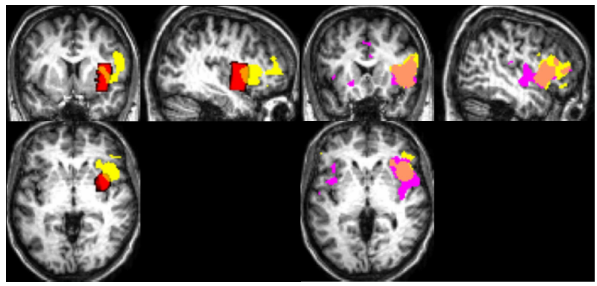

(f) Patient 33. The single activation cluster of the selected IC maps clearly overlaps with both the SOZ and the GLM-based activation map.

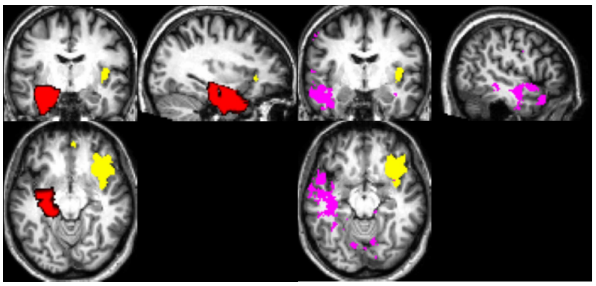

(g) Patient 34. The selected IC does not show overlap with either the SOZ or the GLM-based activation map.

Figure 6.7: An IC was selected in 7 out of 10 patients. The selected ICs are shown in yellow, while the SOZ and the GLM-based activation maps are shown in red and violet, respectively.

6.2.5 Discussion

In this section an automatic method was developed which selects the epileptic source among fMRI ICs. To this end, artefact related ICs were first rejected using a recently introduced and online available technique [178]. Afterwards, the remaining BOLD related ICs were characterised with four features, which were fed to a LS-SVM classifier. The proposed technique was evaluated on a dataset including fMRI recordings of 10 focal epilepsy patients and 13 healthy controls. It reached 77% specificity, indicating that the proposed technique reliably selects ICs related to epileptic activity. Indeed, in the vast majority of patients where a selection was made, the selected IC overlapped either with the SOZ or the GLM-based EEG-fMRI activation map.

Considering the small size of the patient group, these results are only preliminary, however, promising. In comparison with the semi-blind approach presented in [213], our method reaches lower sensitivity (62% vs. 40%) and specificity (77% vs 90%). However, the semi-blind approach relies on simultaneously recorded EEG information. In case EEG recordings are not available or of insufficient quality, our approach may be very valuable. Moreover, the performance of our technique is in line with the results obtained with another fully blind approach [137] using activelet based representation and spatiotemporal clustering of the fMRI voxel time series. This approach performed very well on fMRI runs with only a few epileptic events as these data matched the sparsity assumption of the method. However, in a group of runs containing more than five events, the obtained activation maps were concordant with GLM activation maps in 69% of cases. Our technique, tested

on patients who showed plenty of IEDs, provided maps concordant with the GLM activation maps or with the SOZ in 5 out of 7 cases (71%).

Although we emphasised in section 6.1.4 that multiple epileptic ICs may exist in each patient, we insist on selecting exactly one. The goal is to pinpoint an epileptic IC which can help identifying the SOZ without any further visual inspection or prior information from other modalities. An inherent limitation of our algorithm in its current stage is that it cannot differentiate between initial and propagated activity or sources corresponding to different IED types. Allowing the selection of more ICs per patient presumably increases the sensitivity of our method. However, manual intervention would be necessary to determine the one corresponding to the SOZ based on some prior knowledge, e.g. the spike field of the preponderant spike type. In order to overcome this limitation, future work will aim at characterising the differences between ICs representing initial (preponderant) and propagated (secondary) activity.

Note that the dataset used in this study consisted of patients where IEDs were recorded in the EEG. However, our methodology is especially relevant in cases where no epileptic activity is present, hence, GLM based analysis cannot be carried out. Therefore, the proposed blind selection method should be tested on a dataset of EEG-negative cases as well. We expect that the proposed technique will pinpoint the SOZ in at least a few such cases, which would yield a considerable improvement over the state of the art.

6.3 Conclusion

This chapter tackled the problem of localising the SOZ based on fMRI recordings. This work is motivated by the fact that traditional fMRI studies which use EEG to determine the timing of interictal epileptic activity often fail due to insufficient EEG information. First, a retrospective proof of concept study was conducted and presented in 6.1. Namely, it was shown that ICA is capable of extracting epileptic sources from the fMRI even in patients where no epileptic events were recorded in the EEG. Moreover, these sources were shown to be informative with respect to the SOZ. In order to put this theoretical concept into practice, the epileptic IC has to be selected blindly. Therefore, such a blind selection method is proposed and some preliminary results are presented in section 6.2. Although the proposed method reached promising specificity, its sensitivity for localising the SOZ should be improved in order to be useful in clinical practice.

Chapter 7

Conclusion and future work

7.1 Conclusions of the thesis

We summarise the main contributions and conclusions of the thesis from both the application and methodology point of view.

7.1.1 Applications

In chapter 2 three bottlenecks were identified in the current presurgical evaluation procedure, related to the analysis and the interpretation of EEG and fMRI signals. The goal of this thesis was to propose novel approaches and develop new algorithms to solve these issues.

1. **Automated seizure detection**
   First the utility of a universal seizure detector was explored. A novel algorithm was developed, which translates the visually appearing characteristics and human interpretation and reasoning process to mathematical features and decision rules, mimicking the expert EEG reader. The advantage of the algorithm lies within its transparency and easy interpretability [102]. Although it reaches high sensitivity, it suffers from a high false detection rate. Therefore, it is not practical to use in clinical practice as a warning device. This is an inherent problem in universal seizure detectors, as the seizure characteristics of different patients are very diverse and may resemble non-ictal activity of other patients.

However, there is low intra-patient variability considering both the morphology and the spatial distribution of the ictal pattern. A patient-specific system can be expected to reach higher specificity, however, at the cost of a necessary training period for each individual patient. Therefore, a patient-specific seizure detection approach was also developed in this thesis. The strength of the proposed technique lies within incorporating spatial information from the multichannel EEG. The method proved to outperform traditional techniques, where spatial information is not exploited, even if less seizure examples were used for training [105].

2. **Modelling ictal sources in EEG**
   The morphology and spatial distribution of the seizure pattern provides important information about the localisation, configuration and the size of the epileptogenic zone [231]. As the ictal EEG pattern is superimposed on background EEG activity and is often obscured by artefacts, BSS techniques are very useful to extract the clean activity pattern. In chapter 5 ictal EEG patterns were decomposed using a recently introduced tensor decomposition technique, called block term decomposition (BTD). We applied wavelet transformation or Hankel expansion to organise the EEG data in a tensor. The former approach was capable of modelling nonstationary seizures which evolve either in frequency or spatial distribution, while the latter was useful for extracting the ictal pattern covered by severe artefacts. Nevertheless, the successful use of this technique in practice depends on blind selection of appropriate model parameters.

3. **Localisation of interictal sources in fMRI**

   Chapter 2 explained the utility of interictal fMRI in the precise localisation of the irritative zone in focal epilepsy, as well as the limited applicability of standard EEG-correlated fMRI analysis. In this thesis an alternative solution was proposed based on independent component analysis. We showed that ICA can extract sources from the fMRI time series which coincide with the ictal onset zone even in cases where no interictal activity was seen in the EEG [106].

   This proof of concept has motivated further research towards developing an automated technique to select the epileptic independent component. A cascade of two classifiers is proposed. The first classifier is a recently introduced and publicly available solution [178] which distinguishes artefact related components from BOLD signal related ones. Subsequently, the second classifier distinguishes epileptic sources from non-epileptic ones among the BOLD related components, based on four newly developed discriminative measures fed to a LS-SVM classifier. The spatial map

corresponding to the selected epileptic component provides localising information. The proposed method provided promising preliminary results. We expect that the technique will pinpoint the SOZ in several EEG-negative cases, which would yield a considerable improvement over the state of the art.

7.1.2 Methodology

The methodology behind all these applications shares a common concept, namely, exploiting the spatial structure underlying the multivariate time series, i.e. the multichannel EEG signals and the voxel-by-voxel fMRI time series. Different ways of incorporating such information can be distinguished:

1. Explicitly, via feature extraction
   This approach aims at explicitly quantifying a certain aspect of the spatial structure. In focal epilepsy the spatial distribution of the signal carries crucial information: while normal processes tend to have a symmetric structure, focal epileptiform patterns are restricted to a certain brain area and hence are asymmetric. We successfully applied a measure of asymmetry as a discriminative feature both in EEG-based seizure detection and in localising the ictal onset zone based on fMRI.

2. Implicitly, expressing a preference via regularisation
   Regularisation in supervised learning promotes a solution with certain desired characteristics via a penalty term in the objective function. In this thesis we applied a regularisation scheme using nuclear norm penalty, which helps to facilitate a low rank solution. We classified EEG data represented in the form of a matrix or a tensor, where the EEG channels are organised along one mode. A low rank solution means in this case that the discriminative pattern has a well-defined spatial distribution. This concept was successfully applied for patients-specific seizure detection [105] and single-trial classification in an auditory oddball task [104]. The latter study is also summarised in Appendix C.

3. Implicitly, in blind source separation
   The blind source separation problem in EEG and fMRI analysis consists in retrieving the activity generated by several neural and non-neural sources located at distinct sites, based on a weighted mixture of their activity measured at each electrode or voxel position. Different blind source separation techniques exploit different properties of the sources. For example, ICA of the fMRI signals relies on the assumption that the sources generating the measured BOLD signals are mutually statistically

independent in space. The application of CPD and BTD on EEG data presumes that the pattern of interest has rank-1 or low rank structure in a carefully chosen data representation. CPD and BTD of wavelet expanded EEG tensors allows to model oscillatory seizure patterns with fixed localisation and oscillatory seizure patterns which evolve in frequency or localisation, respectively. Finally, BTD of Hankel structured EEG tensors allowed to model seizure pattern of fixed localisation as a sum of exponentially damped sinusoids.

7.2 Future perspectives

7.2.1 Future work in epilepsy

Here we discuss possible improvements of the fMRI-based localisation method of the seizure onset zone. Future perspectives on other epilepsy related applications, which represent a less direct extension to the work of this thesis, are presented in section 7.3.

Chapter 6 introduced a method to localise the SOZ purely based on data-driven fMRI analysis. The method consist of two consecutive steps. During the first step ICA of the fMRI is performed. Afterwards, based on certain features extracted from the independent components the second step automatically selects the epileptic one. The corresponding spatial map indicates the SOZ.

Future work will focus on combining the two steps of the proposed method. More particularly, instead of explicit feature extraction one can impose constraints on the decomposition, hence, enforcing a solution where at least one source component matches the desired characteristics. The great advantage of such a constrained ICA approach is that, in contrast with the original ICA algorithm, the components are ordered, i.e. there is no need for an additional step to select the source of interest.

ICA is based on the strong assumption that the underlying signal sources are spatially statistically independent. However, this assumption may not hold in interictal epileptic fMRI time series. In fact, there is evidence that depending on the specific epilepsy syndrome, interictal epileptic discharges lead to a unique and widespread network activity [64]. Therefore, the objective within this approach is to apply tensor based methods which do not impose independence constraints. We have seen in previous chapters that CPD and BTD can express a signal as a sum of rank-1 or low rank tensors, respectively. These decompositions are unique under mild conditions. A suitable tensor representation of the fMRI signals has to be established, e.g. by stacking

data from consecutive recording sessions along the third mode. Furthermore, the structure underlying the signal of interest using this representation has to be identified in order to select and successfully apply an appropriate tensor decomposition method.

7.2.2 Neonatal brain monitoring

Throughout this thesis the concept of exploiting the spatial structure of multichannel EEG played a crucial role. So far we utilised of this concept for analysing epileptic EEG and for classifying ERPs, but it can be of use in many EEG applications.

In neonatal monitoring, as well, the spatial characteristics of the EEG is an important aspect. It helps differentiate physiological patterns from artefacts and carries diagnostic information. On one hand, the characteristics of adult and neonatal EEG are very different and techniques developed for adult EEG analysis are in general not directly applicable. Neonatal seizures, for instance, do not follow a consistent spatial distribution as focal seizures do. On the other hand, some aspects of background EEG analysis can benefit from concepts developed in this thesis. Two concrete applications are discussed below.

Brain areas in very young infants are barely interconnected, however, during brain development a sophisticated network is formed through spontaneous interactions [224, 190]. The interaction between various brain regions can be assessed from the spatial properties of the EEG signal. In section 4.2 we developed a new measure called channel symmetry index (CSI) to quantify interhemispheric symmetry of the EEG. Recently, this measure has been applied to distinguish physiological and pathological asymmetries in the EEG and successfully detected abnormal lateralised lesions in the neonatal brain [119].

Furthermore, the duration of the so-called burst-interburst intervals provides important information on the maturation of the brain as well. These patterns are global phenomena in the sense of appearing on most EEG channels simultaneously. An existing automatic burst-suppression segmentation method [135] employs a set of features similar as the ones used in chapter 4.3. However, instead of effectively taking into account the spatial distribution, multichannel information is simply integrated by taking the median value of the features across all the channels. This suboptimal solution is prone to misclassify artefacts. The nuclear norm regularisation approach presented in chapter 4.3 is directly applicable for this problem and presumably improves the segmentation performance.

7.3 Long term vision

We have argued in chapter 1 that technological advancement has already been transforming healthcare in many ways. Examples include digitally storing large amounts of medical data, the increased use of different recording and imaging techniques as well as automated analysis and decision support systems. As current trends point toward wearable devices and home monitoring, we can expect an accelerating growth of available medical information and demand for intelligent systems.

However, before wearable home monitoring systems could be widely used, several issues has to be addressed, including accessible design, robustness and reliability, real-time acquisition and processing, privacy and confidentiality of the medical data, and reimbursement planning [57, 196]. Below we discuss some signal processing challenges which may be solved by extending the methodology used in this thesis.

A crucial requirement in intelligent wearable devices is efficient acquisition and signal processing. Decisions have to be made in real time, possibly using low complexity algorithms to prolong battery life. Moreover, data should be efficiently stored for further inspection. Compressive sensing methods offer the possibility to sample the data at a much lower rate than the Nyquist frequency by exploiting some structural properties of the signals, e.g. sparsity or low-rank structure [134]. In chapter 4 we have shown the low-rank structure is a useful signal model for ictal EEG patterns, which can convey crucial spatial information about the seizure and facilitate discrimination. Current seizure detection systems designed for wireless systems work in three steps: (1) reduce data by compressive sensing or by extracting low complexity features such as energy or line length, (2) transmit the data and (3) perform classification on the server side [30]. Alternatively, one could combine the different approaches in step (1) by using nuclear norm regularisation for compressive sensing of the EEG and directly use the reduced representation as features for classification.

In chapter 4 and 5 we emphasized the impact of artefacts on the interpretability of EEG signals and we discussed various methods to remove them. However, one has to take into account that mobile recordings might give rise to new types of artefacts, e.g. due to the gait cycle [27]. ICA performs sufficiently well in cleaning the EEG recorded during standing and walking conditions. However, a template based artefact rejection had to be applied in the running condition [81, 87]. It would be worthwhile to investigate how tensor based BSS techniques perform in this condition. Furthermore, we have seen in chapter 5, that CPD and BTD are not only useful for removing artefacts, but to characterise and localise epileptic seizures. Computing tensor decompositions via updating

techniques can be useful to continuously track the source of interest during long-term monitoring. Both applications — online artefact removal and source tracking — require efficient, low-complexity updating algorithms [158].

Another challenging aspect of wearable monitoring systems is the need of adaptation to the ever changing environment, recording conditions and physiological state of the brain. In mobile BCI experiments it was shown that ERP characteristics and single-trial classification accuracies significantly differ in inside and outside conditions. Whether this reflects the presence of residual artefact or a difference in cognitive processing in different conditions, is an open question. [53]. In other applications it may not be the activity of interest that changes, but the background neural activity. As the brain produces rhythmic patterns in different stages of the sleep-wake cycle, the optimal decision boundary between seizure and non-seizure pattern may vary in time. Similarly, due to the maturation of the neonatal brain, the activity patterns present in the EEG may evolve in time. Since the available training and testing data might substantially differ from each other, all these applications could benefit from adaptive learning algorithms which can adjust their decision function in response to new information.

Interesting methods in this direction from the BCI field include adaptive LDA with or without error correction [17] or transferring information between different subjects about the confounding effects [180]. This latter approach is based on the observation that there are systematic differences between training and testing sessions among the subjects due to learning effects. A future direction in mobile BCI research could be to investigate whether such systematic confounds between different recording conditions can be captured. Furthermore, the interpretation of the confounding subspace might give an insight into the artefact vs. altered cognitive state ambiguity and might lead to new directions for improvement in BCI classification.

Finally, multisubject or multipatient information can be exploited via multitask learning. In contrast with the above approach the assumption in this case is that there is common discriminative information among subjects or patients. Recent advances in the field allow to take into account structural information from multitask data and individual multilinear data simultaneously [174]. The multiway kernel-based formulation in [189] does not only give rise to a nonlinear extension of the former method, but also facilitates transfer learning. That is, transferring knowledge gained while solving a specific problem to different, but related problems. Transfer learning approaches are useful in case little or no training data are available for a specific task, but sufficient information is available in a related task, where the data follows a different distribution [161]. This phenomenon presumably underlies the problems discussed in the previous paragraphs.

Appendix A

Nuclear norm learning

A.1 CVX implementation of the nuclear norm regularization

The `CVX` implementation of the algorithm solving equation 4.7 is as follows:

```
cvx_begin
    variables e(N) A(I,J)  b
    minimize(1/2*e'*e+reg_par*norm_nuc(A))
    subject to
    diag(y)*(X*A(:)+b)==ones(N,1)-e
cvx_end
```

where X is a $N \times (IJ)$ matrix (the generic row n is the vectorization of the $n-$th input data matrix of size $I \times J$), A is the $I \times J$ classifier matrix and b is a scalar bias term; y is the vector of labels. For consistency we have reported a constrained formulation of the problem that mimic the one used in the LS-SVM primal problem, see 3.20.

A.2 Algorithmic steps of the nuclear norm learning approach

Algorithm 1: Nuclear norm learning

Input: multichannel EEG recording broken down into N 2s long segments
Output: classifier matrix A and bias term b

1. create the input data $X \in R^{d \times p \times N}$ and labels $y \in R^{N \times 1}$
  preprocess EEG
  segment EEG to 2s windows
  for each EEG segment
    extract d features from each channel
    order the feature vectors in p rows to create $p \times d$ matrix
    assign corresponding label
    stack into X
  end
2. model selection: obtain μ
  for cv-loop
    split X into training and validation set
    for all μ_i values in a predefined range
      solve Eq. (4.7) on the training set to obtain A, b
      evaluate on the validation set to obtain misclassification
    end
  end
3. select μ with the best corresponding misclassification
4. solve Eq. (4.7) with μ to obtain A, b

A.3 EEG features extracted for seizure detection in the nuclear norm learning approach

Time domain features were extracted directly from the preprocessed EEG window:

- Number of zero crossings (#0), maxima (#max) and minima(#min)
- Skewness

$$\text{skew} = \mathbb{E}[(\frac{A - \mu}{\sigma})^3] \tag{A.1}$$

  where A is the EEG time series, μ is the mean and σ is the standard deviation and $\mathbb{E}$ denotes the expected value.

- Kurtosis

$$\text{kurt} = \mathbb{E}[(\frac{A-\mu}{\sigma})^4] \tag{A.2}$$

- Root mean square amplitude:

$$\text{rmsa} = \sqrt{\frac{1}{N}\sum_{k=1}^{N} A(k)^2} \tag{A.3}$$

The frequency domain features were extracted from the power spectral density ($S(f)$) computed by Welch's method:

- Total power:

$$TP = \sum_{f_i=1}^{30} S(f_i), \tag{A.4}$$

- Peak frequency

$$PF = \arg\max_{f\epsilon[1,30]} S(f) \tag{A.5}$$

- Mean power in delta, theta, alpha and beta frequency bands:

$$D = \sum_{f_i=1}^{3} S(f_i), \tag{A.6}$$

$$T = \sum_{f_i=4}^{8} S(f_i), \tag{A.7}$$

$$A = \sum_{f_i=9}^{13} S(f_i), \tag{A.8}$$

$$B = \sum_{f_i=14}^{20} S(f_i) \tag{A.9}$$

- Normalized power in delta, theta, alpha and beta frequency bands:

$$nD = \frac{\sum_{f_i=1}^{3} S(f_i)}{\sum_{f_i=1}^{30} S(f_i)}, \tag{A.10}$$

$$nT = \frac{\sum_{f_i=4}^{8} S(f_i)}{\sum_{f_i=1}^{30} S(f_i)}, \tag{A.11}$$

$$nA = \frac{\sum_{f_i=9}^{13} S(f_i)}{\sum_{f_i=1}^{30} S(f_i)}, \tag{A.12}$$

$$nB = \frac{\sum_{f_i=14}^{20} S(f_i)}{\sum_{f_i=1}^{30} S(f_i)} \tag{A.13}$$

Appendix B

Patient demographics in the fMRI study

Table B.1: Clinical description of the patients

Patient	Gender/ age/ age at onset	Ictal onset zone	Etiology	SPECT injection time/ seizure duration (s)	Structural lesion	icEEG concordant	Resection	Outcome ILAE 2001 (1-6)	Follow-up time after surgery (m)	Pathology	Spikerate (spikes/h) during fMRI
1	F/38/12	R temporal	CNS infection	15/76	Ischaemic R parietotemporooccipital lesion	N/A	Planned				1171
2	M/24/2	L posterior temporal	Postsurgical gliosis	42/47	L temporal gliosis after L amygdalohippocampectomy	N/A	Planned				0
3	M/26/22	L anterior temporal	FCD	12/42	Normal	N/A	Yes	1	25	FCD	0
4	M/34/18	R anterior temporal	HS	10/58	Normal	N/A	Yes	1	14	HS	0

5	F/23/9	L anterior temporal	DNET	15/54	L temporal DNET	N/A	Yes	2	18	DNET	187
6	M/24/18	R anterior temporal	Unknown	53/90	Normal	N/A	Refusal				0
7	F/56/8	R parieto-occipito-temporal	Sturge-Weber	16/33	Superficial angioma and hemiatrophy R posterior convexity	N/A	Planned				156
8	M/20/7	L parieto-temporal	Unknown	94/139	L parietal gliosis after surgery	Yes	Overlap elo-quent cx				15
9	F/34/15	R frontal	FCD	3/20	Subtle R frontal FCD	Yes	Yes	2	13	Gliosis, micraglia activation, neuronal loss	853
10	F/55/38	L anterior temporal	HS	38/73	L HS	N/A	Yes	1	18	HS	156
11	M/39/31	L temporal	DNET	27/64	L temporal DNET	N/A	Yes	1	13	DNET	0
12	M/17/3	R anterior temporal	CNS infection+HS	5/76	R HS	N/A	Yes	1	15	HS	0
13	M/44/12	R temporal	HS	21/72	R HS	N/A	Yes	1	10	HS	0
14	M/27/22	L anterior temporal	Unknown	10/94	Normal	Yes	Planned				36

15	F/21/12	L temporal	Post-traumatic	23/45	L HS and bi-parietal contusions	N/A	Planned				0
16	M/26/1	L mesial frontal	Tuberous sclerosis	3/29	L frontal gliosis and FCD L frontal, bi-parietal and bioccipital	N/A	Planned				710
17	M/40/27	R mesial temporal	CNS infection+FS	21/60	R HS	N/A	Refusal				0
18	F/61/12	L frontal	FCD	3/18	L frontal FCD	N/A	Overlap eloquent cx				915
19	F/29/18	R occipital	Unknown	26/122	Normal	N/A	Overlap eloquent cx				0
20	M/19/10	R parietal	Leptomeningitis	14/68	Normal	Yes	Yes	1	13	Leptomeningitis	0
21	F/31/9	L perirolandic	Stroke	18/80	Ischaemic L frontoparietal lesion, L temporal hypoplasia	N/A	Overlap eloquent cx				0
22	F/63/21	R mesial temporal	FS+HS	30/162	R HS	N/A	Yes	1	14	HS	0

23	F/39/27	R ventrotemporal	Cavernous angioma	10/52	R temporal cavernous angioma	N/A	Yes	2	11	Angioma	0
24	M/45/36	L parietotemporal	Unknown	17/45	Normal	N/A	Overlap eloquent cx				0
25	M/29/2	R frontal	Postsurgical gliosis	4/25	R frontal gliosis	Yes	Planned				0
26	M/30/15	R temporal	Unknown	12/58	Normal	N/A	Planned				733
27	F/23/2	L temporal	FCD	43/158	L temporal FCD	N/A	Overlap eloquent cx				0
28	F/33/7	L anterior temporal	FS+HS	61/92	L HS	N/A	Planned				1
29	M/20/8	L anterior temporal	HS	N/A	Temporal	N/A	Yes	1	6	HS	8
30	F/33/6	L temporooccipital	FCD	15/57	L posterior temporal FCD	N/A	Overlap eloquent cx				1613
31	F/40/1	L parietal	FCD	18/423	L parietal FCD	N/A	overlap eloquent cx				589
32	F/45/19	R temporal	Unknown	23/64	Normal	N/A	Refusal				168

33	F/48/3	R insula	Unknown	1/5	Normal	Concordant	Planned				384
34	F/30/0	L temporal	HS	17/97	L HS	N/A	Yes	1	2	HS	40
35	F/56/32	R temporal	HS	10/179	R HS	N/A	Refusal				602

Appendix C

Learning from structured EEG data in brain computer interfaces

In Chapter 4 a seizure detection algorithm was presented that exploits structural information from the EEG data matrix via nuclear norm regularisation. The low-rank structure conveyed by the nuclear norm represented spatial information, which is a crucial aspect of the seizure patterns in focal epilepsy. In Chapter 5 also the temporal structure of the signals were taken into account. We have seen that ictal EEG, represented in the form of a $channel \times Hankel\ matrix$ tensor, is successfully modelled by a low multilinear rank component. The underlying spatiotemporal structure is an essential property of the EEG signals in general, therefore, we expect that other applications will benefit from these models as well. In this chapter we apply this concept for classifying auditory ERPs, with its prospective application in brain computer interfaces in mind. First, section C.1 gives a short overview about BCI and section C.2 presents the state of the art methodology in the field. Further, the data acquisition, preprocessing, signal representation and classification approach is explained in section C.2.1. The classification results are analysed in comparison with different approaches in section C.3. Finally, section C.4 is devoted to discussion.

C.1 Introduction

Brain Computer Interfaces (BCI) provide users with radically new communication channels which do not depend on peripheral nerves or muscles. As such, it can facilitate communication for totally paralysed locked-in individuals and those with severe neurovascular impairment. Over the past decades a lot of studies have been investigating various ways to record and interpret neural activity recorded at the scalp or within the brain and to finally use it to control a cursor, select a letter or operate a neuroprothesis [229, 181]. The most successful non-invasive approaches are based on visually evoked potentials, e.g. [6], event related desynchronisation patterns during motor imagery, e.g. [163] and the P300 component of the event-related potentials in response to stimuli in an oddball paradigm, e.g. [65]. The BCI records and analyses the user's brain activity and infers to his intention by assigning the neural response to one of two or more possible groups (yes or no, left or right, etc.) Therefore, single-trial ERP classification is a key issue in BCI design.

C.2 Single trial ERP classification

Successful single-trial classification of EEG data depends on discriminative feature extraction combined with a suitable classifier. Both aspects have been tackled extensively in the literature.

Regarding classification approaches, linear discriminant analysis (LDA) is probably the most common approach in BCI research, and was shown to be optimal if proper preprocessing is applied. To limit the influence of outliers and account for the estimation error of the covariance matrix, regularized or shrinkage LDA can be used. Various different algorithms were successfully applied as well, such as Bayesian techniques, support vector machines, neural networks, etc. For an overview, see [130, 138]. Nevertheless, the features used as input to any classifier need to be carefully chosen to obtain real discriminative power.

A common approach for feature extraction in ERP-based BCI is the decimation and concatenation of the signals from each channel to a long feature vector. However, this leads to high dimensional input data, moreover, it ignores the spatial properties of multichannel data. Feature extraction approaches exploiting spatial information from the multichannel EEG include common spatial patterns (CSP) [170] and beamforming techniques [165]. Recently, higher order discriminant analysis was proposed to extract features capturing the multilinear structure in tensor expansion of EEG data [164].

Here we consider an auditory oddball paradigm, recorded in normal indoor and walking outdoor conditions. The signal of interest, in our case the P300 ERP component, unlike noise, is a structured signal in the multidimensional space spanned by channels, time, frequency or possibly other types of features. The proposed classification approach finds an optimal discriminative subspace exploiting the inherent multidimensional structure of the EEG data through spectral regularization using nuclear norm without explicit feature extraction. It was shown that exploiting tensor structure in the learning algorithm is especially useful for small samples sizes [91], which is a typical challenge in BCI reseach. Regularization with nuclear norm for matrix classification was proposed in [210, 211] for BCI data, and was successfully applied for epileptic seizure detection, as shown in chapter 4. Nuclear norms were extended to the case of higher order arrays as a heuristic for multilinear rank constrained problems [189].

In the proposed approach single trials are represented in a tensor, where Hankel matrices constructed from the decimated signals of each channel are stacked along the third mode. The performance of the proposed nuclear norm regularization technique applied on tensorial data is compared with two alternative approaches: (1) classification using nuclear norm regularization on matrices, where decimated signals from each channel constitute each row of a matrix, and (2) shrinkage LDA applied on concatenating the decimated signals from each channel.

C.2.1 Methods

Data acquisition

Sixteen healthy volunteers free of past or present neurological or psychiatric conditions participated. 616 standard and 84 deviant tones (600 and 1200 Hz, respectively) were presented in randomized order at a fixed interstimulus interval (1,000 ms) in two experimental conditions. Participants were asked to silently count the rare tones. In the indoor recording condition, they sat in a quiet office room; in the outdoor recording condition, they walked slowly on campus. No instructions were given for head and eye movements. The route consisted of different surfaces and the environment included substantial ambient noise. The order of indoor and outdoor conditions was balanced across subjects. Stimulus presentation was controlled with OpenViBE. EEG was recorded with a 14-channel wireless EEG (128 Hz sampling rate; 0.16-45 Hz band-pass; Emotiv: www.emotiv.com) connected to a state-of-the-art infracerebral electrode cap (www.easycap.de), with electrodes positioned at sites according to the standard 10-20 system. The resulting system is of small size and weight, could be

tightly attached to the cap. The signal quality was improved due to the sintered Ag/AgCl electrodes. Data were analyzed offline using EEGLAB and MATLAB. Extended infomax independent component analysis (ICA) was used to semiautomatically attenuate eye blinks [49]. EEG data were 20 Hz low-pass filtered, and trial epochs were extracted (-200 to 700 ms) and baseline corrected (-200 to 0 ms) and re-referenced to the average of Tp9 and TP10. Trials with large or non-stereotypical artifacts were rejected. Standard trials preceding deviants were selected to equalize the number of standard and deviant trials, resulting in a minimum of 70 standard and deviant tones per subject.

Feature extraction

EEG data from all 12 electrodes was subdivided in 30 non-overlapping time windows comprising 0 to 700 ms. The mean signal amplitudes of each time window served as the initial features. Different organization of these initial features leads to the following three different data representations: (1) Features extracted from each electrode concatenated in a long vector of size $1 \times 12 \cdot 30$. (2) Features extracted from each electrode constitute each row of a matrix of size 12×30. (3) Features extracted from each electrode $(x_{ch}(n), n = 1, ..., N)$ are organized in a Hankel matrix of dimensions $L \times M$, with $N = L + M - 1$, as seen in section 5.2.1. The resulting matrices are stacked in a tensor of size $12 \times 16 \times 15$.

Classification.

In order to mimic an online scenario, the first half of the trials ($N_{tr} = 70$) were used for training, and the second half ($N_{te} = 70$) was used for testing. In order to test the influence of the training set size on the performance of the classifiers, different training set sizes were tested, ranging from 10 to 70. Note the relatively low number of available training samples in each case and the high dimensionality of our feature space. Modelling with such a dataset carries the risk of overfitting. Therefore, the following classification approaches were considered.

Linear discriminant analysis with shrinkage. In linear discriminant analysis (LDA) a crucial role is played by the estimation of the class covariance estimator. The empirical covariance matrix, however, is systematically biased towards larger eigenvalues in case of small sample sizes. Therefore, shrinkage LDA was applied on the feature vector representation.

Spectral regularization with nuclear norm. Regularization via nuclear norm conveys a-priori structural information and therefore facilitates good classification for small sample sizes. Therefore, it particularly fits the P300 classification problem, where the signal of interest has a multilinear structure and only a limited number of training samples are available. The nuclear norm regularization approach was applied on the matrix and tensor based feature representation. We refer to these appoaches as mNNL and tNNL, respectively.

C.3 Results

Figure C.1 shows the performance of each classification approach in the inside and outside conditions using $N_{tr} = 70$ training samples for each subject. Each classifier performed better than chance level, although higher mean accuracies were achieved in the inside condition (LDA: 74%, mNNL: 77% and tNNL: 81%) than in the walking outside condition (LDA: 66%, mNNL: 70% and tNNL: 72%). Note that the P300 ERP component was significantly larger in the indoor condition [53]. In each condition both mNNL and tNNL outperformed LDA significantly ($p < .05$ and $p < .01$, respectively). Moreover, in the inside condition tNNL outperformed mNNL significantly ($p < .05$).

Figure C.2 shows the performance of each classification approach in the inside and outside conditions using different training set sizes. In the inside condition, using only 10 training samples, each classifier achieves a moderate performance, and improves significantly if more training samples are included ($p < .01$). However, in the outside condition, LDA fails to generalize from the additional training samples and maintains approximately constant performance with increasing training set size. In contrast, tNNL and mNNL are able to capture additional information even from such noisy samples and reach significantly higher performance for larger training sets ($p < .01$).

Finally, the feature weights obtained for a single subject in each classification approach is depicted in Figure C.3. In case of LDA, the long feature vector is matricised in order to get a channel x time representation. For the tNNL approach the classifier tensor is unfolded along the second mode, resulting in a matrix representation where the features corresponding to the Hankel matrices obtained from each channel are concatenated. Note that the classifier matrix and tensor obtained by the mNNL and tNNL approaches clearly resemble P300 properties (maximal feature weights at channel Pz around 300ms after stimulus), as opposed to the unstructured feature weights obtained by LDA.

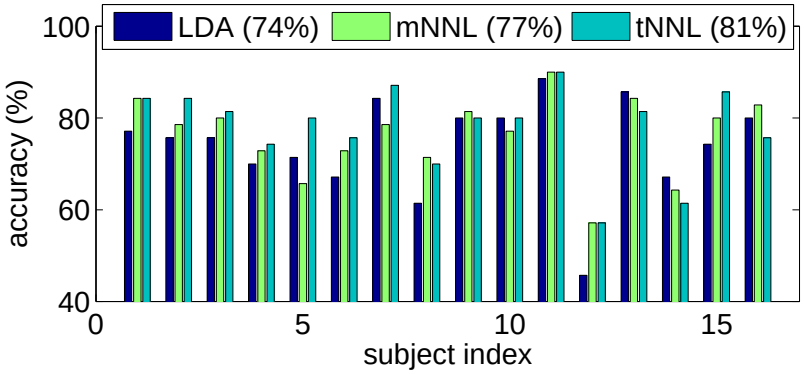

(a) Inside

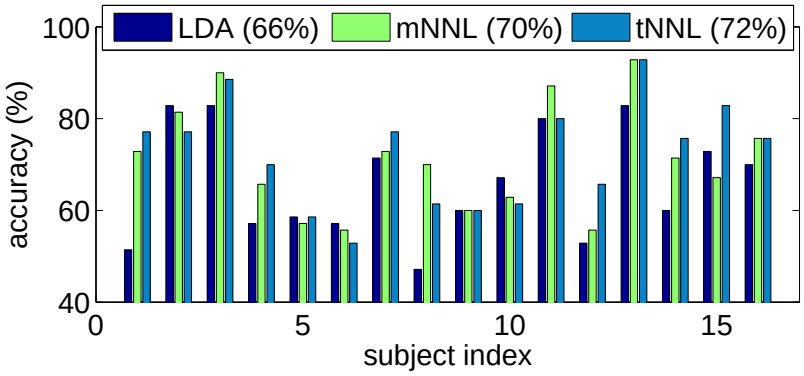

(b) Outside

Figure C.1: Comparison of accuracies obtained with the different classification approaches for a training set size of N_{tr} = 70. Mean accuracies are shown in brackets.

C.4 Discussion

In this work we considered the problem of classifying high dimensional, small sample size data, namely an auditory P300 paradigm recorded under normal and under noisy conditions. We showed that spectral regularization with nuclear norm outperforms shrinkage LDA in both conditions. Moreover, we demonstrate that under noisy conditions, while shrinkage LDA overfits and fails to benefit from additional training samples, spectral regularization can generalize from such a diverse manifold. Initially support vector machines with linear and with RBF kernels were also considered, however, as their

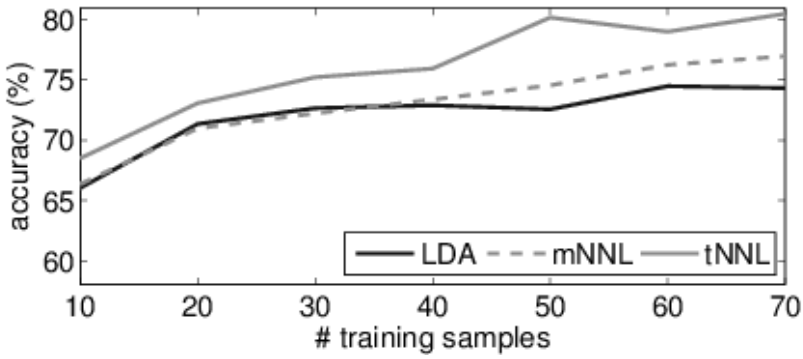

(a) Inside

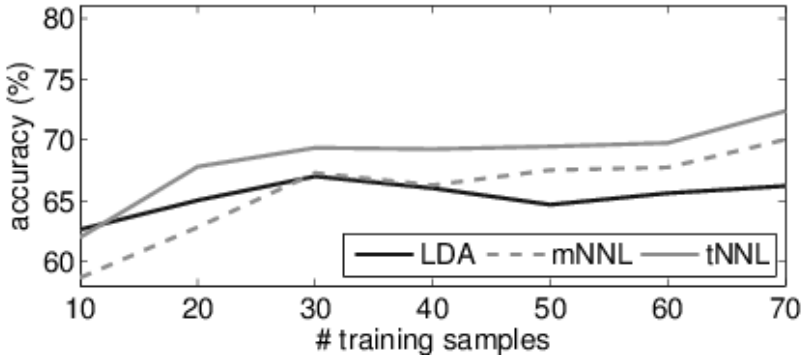

(b) Outside

Figure C.2: Comparison of median accuracies of the different classification approaches with increasing training set size.

performance was comparable to shrinkage LDA the results are not shown here. Due to its low computational cost, LDA remains a popular classification method. Computational complexity of the nuclear norm regularization approach scales with the order of the tensor. However, for small training set sizes and for second and third order tensors it remains within reasonable limits [107]. The strength of spectral regularization with nuclear norm penalty lies within conveying structural information from the higher order input arrays. In our study this means conveying spatiotemporal structure in the matrix case and spatial-temporal-spectral structure in the tensor case. Such a-priori structural information facilitates good generalization even in case of small sample sizes and in the presence of noise. The auditory oddball task used in this work is not

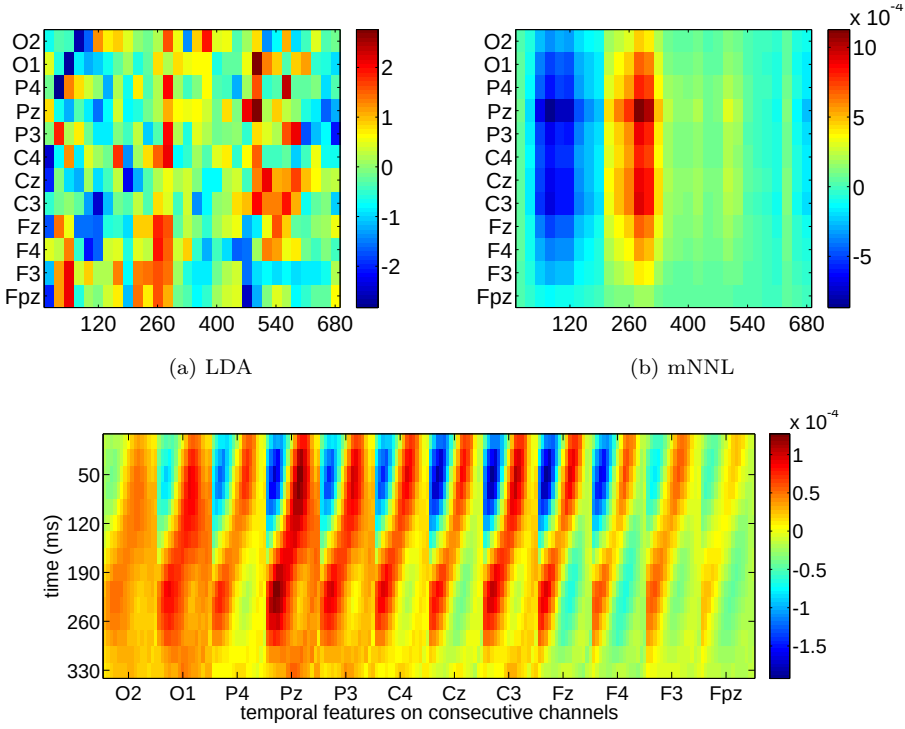

(a) LDA

(b) mNNL

(c) tNNL

Figure C.3: Feature weights obtained for a single subject. In case of LDA, the long feature vector is matricised in order to get a channel x time representation. For the tNNL approach the classifier tensor is unfolded along the second mode, resulting in a matrix representation where the features corresponding to the Hankel matrices obtained from each channel are concatenated.

directly applicable as a BCI paradigm. Instead, a three-stimulus oddball task should be used, including a standard and two target stimuli. The objective in this case is to differentiate between target 1 and target 2, allowing the user to express binary choices [88]. Future work should be carried out to test the proposed approach in such a three-stimulus dataset.

Bibliography

[1] Acar, E., Aykut-Bingol, C., Bingol, H., Bro, R., and Yener, B. Multiway analysis of epilepsy tensors. *Bioinformatics 23*, 13 (2007), i10–i18.

[2] Acar, E., Bingol, C., Bingol, H., Bro, R., and Yener, B. Seizure recognition on epilepsy feature tensor. In *Engineering in Medicine and Biology Society, 2007. EMBS 2007. 29th Annual International Conference of the IEEE* (Aug 2007), pp. 4273–4276.

[3] Adeli, H., Ghosh-Dastidar, S., and Dadmehr, N. A wavelet-chaos methodology for analysis of eegs and eeg subbands to detect seizure and epilepsy. *Biomedical Engineering, IEEE Transactions on 54*, 2 (2007), 205–211.

[4] Adeli, H., Zhou, Z., and Dadmehr, N. Analysis of eeg records in an epileptic patient using wavelet transform. *Journal of neuroscience methods 123*, 1 (2003), 69–87.

[5] Allen, P. J., Josephs, O., and Turner, R. A method for removing imaging artifact from continuous eeg recorded during functional mri. *NeuroImage 12*, 2 (2000), 230 – 239.

[6] Allison, B. Z., McFarland, D. J., Schalk, G., Zheng, S. D., Jackson, M. M., and Wolpaw, J. R. Towards an independent brain–computer interface using steady state visual evoked potentials. *Clinical Neurophysiology 119*, 2 (2008), 399–408.

[7] Alpaydin, E. *Introduction to machine learning*. MIT press, 2004.

[8] Altenburg, J., Vermeulen, R. J., Strijers, R. L., Fetter, W. P., and Stam, C. J. Seizure detection in the neonatal eeg with synchronization likelihood. *Clinical neurophysiology 114*, 1 (2003), 50–55.

[9] Beckmann, C. F., DeLuca, M., Devlin, J. T., and Smith, S. M. Investigations into resting-state connectivity using independent component analysis. *Philosophical Transactions of the Royal Society B: Biological Sciences 360*, 1457 (2005), 1001–1013.

[10] Bell, A., and Sejnowski, T. An information–maximization approach to blind separation and blind deconvolution. *Neural Comput. 7*, 6 (Nov. 1995), 1129–1159.

[11] Belouchrani, A., Abed-Meraim, K., Cardoso, J.-F., and Moulines, E. A blind source separation technique using second-order statistics. *Signal Processing, IEEE Transactions on 45*, 2 (1997), 434–444.

[12] Bénar, C. G., Aghakhani, Y., Wang, Y., Izenberg, A., Al-Asmi, A., Dubeau, F., and Gotman, J. Quality of eeg in simultaneous eeg-fmri for epilepsy. *Clinical Neurophysiology 114*, 3 (2003), 569 – 580.

[13] Benbadis, S. R., O'Neill, E., Tatum, W. O., and Heriaud, L. Outcome of prolonged video-eeg monitoring at a typical referral epilepsy center. *Epilepsia 45*, 9 (2004), 1150–1153.

[14] Berg, A. T., Berkovic, S. F., Brodie, M. J., Buchhalter, J., Cross, J. H., Van Emde Boas, W., Engel, J., French, J., Glauser, T. A., Mathern, G. W., Mosh??, S. L., Nordli, D., Plouin, P., and Scheffer, I. E. Revised terminology and concepts for organization of seizures and epilepsies: Report of the ilae commission on classification and terminology, 2005?2009. *Epilepsia 51*, 4 (2010), 676–685.

[15] Berg, P., and Scherg, M. Dipole modelling of eye activity and its application to the removal of eye artefacts from the EEG and MEG. *Clinical Physics and Physiological Measurement 12* (1991), 49–54.

[16] Bishop, C. M. *Neural networks for pattern recognition*. Oxford university press, 1995.

[17] Blumberg, J., Rickert, J., Waldert, S., Schulze-Bonhage, A., Aertsen, A., and Mehring, C. Adaptive classification for brain computer interfaces. In *Engineering in Medicine and Biology Society, 2007. EMBS 2007. 29th Annual International Conference of the IEEE* (2007), IEEE, pp. 2536–2539.

[18] Blume, W., and et. al. Glossary of descriptive terminology for ictal semiology: Report of the ILAE task force on classification and terminology. *Epilepsia 42(9)* (2001), 1212–8.

[19] Bro, R., and Kiers, H. A. L. A new efficient method for determining the number of components in PARAFAC models. *Journal of Chemometrics 17*, 5 (2003), 274–286.

[20] Brodal, P. *The Central Nervous System.* Oxford University Press, USA, 2010.

[21] Buteneers, P. *Detection of epileptic seizures: the reservoir computing approach.* PhD thesis, Ghent University, 2012.

[22] Buxton, R., Wong, E., and Frank, L. Dynamics of blood flow and oxygenation changes during brain activation: The balloon model. *Magnetic Resonance in Medicine 39*, 6 (1998), 855–864.

[23] Calhoun, V., Adali, T., Pearlson, G., and Pekar, J. A method for making group inferences from functional mri data using independent component analysis. *Human Brain Mapping 14*, 3 (2001), 140–151.

[24] Calhoun, V., Pekar, J., McGinty, V., Adali, T., Watson, T., and Pearlson, G. Different activation dynamics in multiple neural systems during simulated driving. *Human Brain Mapping 16*, 3 (2002), 158–167.

[25] Candes, E., and Recht, B. Exact matrix completion via convex optimization. *Foundation of Computational Mathematics 9 (6)* (2009), 717–772.

[26] Castellanos, J., Gómez, S., and Guerra, V. The triangle method for finding the corner of the l-curve. *Applied Numerical Mathematics 43*, 4 (2002), 359 – 373.

[27] Castermans, T., Duvinage, M., Petieau, M., Hoellinger, T., Saedeleer, C., Seetharaman, K., Bengoetxea, A., Cheron, G., and Dutoit, T. Optimizing the performances of a p300-based brain computer interface in ambulatory conditions. *Emerging and Selected Topics in Circuits and Systems, IEEE Journal on 1*, 4 (Dec 2011), 566–577.

[28] Chapelle, O., Schölkopf, B., Zien, A., et al. *Semi-supervised learning*, vol. 2. MIT press Cambridge, 2006.

[29] Chaudhary, U., Duncan, J., and Lemieux, L. Mapping hemodynamic correlates of seizures using fmri: A review. *Human Brain Mapping 34(2)* (2013), 447–66.

[30] Chiang, J., and Ward, R. K. Energy-efficient data reduction techniques for wireless seizure detection systems. *Sensors 14*, 2 (2014), 2036–2051.

[31] Comon, P., and Jutten, C., Eds. *Handbook of Blind Source Separation, Independent Component Analysis and Applications.* Academic Press, 2010.

[32] Cooper, R., Winter, A., Crow, H., and Walter, W. Comparison of subcortical, cortical and scalp activity using chronically indwelling electrodes in man. *Electroencephalography and Clinical Neurophysiology 18* (1965), 217–228.

[33] Cordes, D., Haughton, V., Arfanakis, K., Carew, J., Turski, P., Moritz, C., Quigley, M., and Meyerand, M. Frequencies contributing to functional connectivity in the cerebral cortex in resting–state data. *American Journal of Neuroradiology 22*, 7 (2001), 1326–1333.

[34] Cuffin, B. N., Cohen, D., Yunokuchi, K., Maniewski, R., Purcell, C., Cosgrove, G. R., Ives, J., Kennedy, J., and Schomer, D. Tests of eeg localization accuracy using implanted sources in the human brain. *Annals of Neurology 29*, 2 (1991), 132–138.

[35] Curio, G. Ain't no rhythm fast enough: Eeg bands beyond beta. *Journal of clinical neurophysiology: official publication of the American Electroencephalographic Society 17*, 4 (2000), 339.

[36] Damoiseaux, J., Rombouts, S., Barkhof, F., Scheltens, P., Stam, C., Smith, S., and Beckmann, C. Consistent resting–state networks across healthy subjects. *Proceedings of the National Academy of Sciences 103*, 37 (2006), 13848–13853.

[37] De Boer, H. M., Mula, M., and Sander, J. W. The global burden and stigma of epilepsy. *Epilepsy Behav 12* (2008), 540 – 6.

[38] De Brabanter, K., Karsmakers, P., Ojeda, F., Alzate, C., De Brabanter, J., Pelckmans, K., De Moor, B., Vandewalle, J., and Suykens, J. A. K. Ls-svmlab toolbox user's guide version 1.8. Tech. rep., ESAT-SISTA, K.U.Leuven, 2011.

[39] De Clercq, W., Vanrumste, B., Papy, J.-M., Van Paesschen, W., and Van Huffel, S. Modeling common dynamics in multichannel signals with applications to artifact and background removal in eeg recordings. *Biomedical Engineering, IEEE Transactions on 52*, 12 (2005), 2006–2015.

[40] De Clercq, W., Vergult, A., Vanrumste, B., Van Paesschen, W., and Van Huffel, S. Canonical correlation analysis applied to remove muscle artifacts from the electroencephalogram. *IEEE Trans Biomed Eng 53*, 12 (2006), 2583 – 87.

[41] De Lathauwer, L. Decompositions of a higher-order tensor in block terms - Part I: Lemmas for partitioned matrices. *Siam J. Matrix Anal. Appl. 30*, 3 (2008), 1022–1033.

[42] De Lathauwer, L. Decompositions of a higher-order tensor in block terms - Part II: Definitions and Uniqueness. *Siam J. Matrix Anal. Appl. 30*, 3 (2008), 1033–1066.

[43] De Lathauwer, L. Blind separation of exponential polynomials and the decomposition of a tensor in rank-(L_r, L_r, 1) terms. *Siam J. Matrix Anal. Appl. 32*, 4 (2011), 1451–1474.

[44] De Lathauwer, L., and De Baynast, A. Blind deconvolution of ds-cdma signals by means of decomposition in rank- (1,l,l) terms. *Signal Processing, IEEE Transactions on 56*, 4 (2008), 1562–1571.

[45] De Lathauwer, L., De Moor, B., and Vandewalle, J. An introduction to independent component analysis. *Journal of chemometrics 14*, 3 (2000), 123–149.

[46] De Lathauwer, L., De Moor, B., and Vandewalle, J. A Multilinear Singular Value Decomposition. *SIAM J. Matrix Anal. Appl. 21*, 4 (2000), 1253–1278.

[47] De Lathauwer, L., and Nion, D. Decompositions of a higher-order tensor in block terms - Part III: Alternating Least Squares Algorithms. *Siam J. Matrix Anal. Appl. 30*, 3 (2008), 1067–1083.

[48] De Martino, F., Gentile, F., Esposito, F., Balsi, M., Di Salle, F., Goebel, R., and Formisano, E. Classification of fmri independent components using ic–fingerprints and support vector machine classifiers. *NeuroImage 34*, 1 (2007), 177 – 194.

[49] De Vos, M., De Lathauwer, L., and Van Huffel, S. Spatially constrained ica algorithm with an application in EEG processing. *Signal Processing 91*, 8 (2011), 1963–1972.

[50] De Vos, M., De Lathauwer, L., Vanrumste, B., Van Huffel, S., and Van Paesschen, W. Canonical decomposition of ictal scalp eeg and accurate source localisation: principles and simulation study. *Intell. Neuroscience 2007* (Apr. 2007), 11:1–11:8.

[51] De Vos, M., Deburchgraeve, W., Cherian, P. J., Matic, V., Swarte, R. M., Govaert, P., Visser, G. H., and Van Huffel, S. Automated artifact removal as preprocessing refines neonatal seizure detection. *Clinical Neurophysiology 122*, 12 (2011), 2345 – 2354.

[52] De Vos, M., Vergult, A., De Lathauwer, L., De Clercq, W., Van Huffel, S., Dupont, P., Palmini, A., and Van Paesschen, W. Canonical decomposition of ictal scalp EEG reliably detects the seizure onset zone. *NeuroImage 37* (2007), 844–854.

[53] Debener, S., Minow, F., Emkes, R., Gandras, K., and De Vos, M. How about taking a low-cost, small, and wireless eeg for a walk? *Psychophysiology 49*, 11 (2012), 1449–53.

[54] Debener, S., Ullsperger, M., Siegel, M., and Engel, A. Single–trial eeg–fmri reveals the dynamics of cognitive function. *Trends in Cognitive Sciences 10*, 12 (2006), 558 – 563.

[55] Deburchgraeve, W., Cherian, P., De Vos, M., Swarte, R., Blok, J., Visser, G., Govaert, P., and Van Huffel, S. Automated neonatal seizure detection mimicking a human observer reading eeg. *Clin Neurophysiol 119*, 11 (2008), 2447 – 2454.

[56] Delorme, A., Sejnowski, T., and Makeig, S. Enhanced detection of artifacts in eeg data using higher-order statistics and independent component analysis. *Neuroimage 34*, 4 (2007), 1443–1449.

[57] Demiris, G. Electronic home healthcare: concepts and challenges. *International Journal of Electronic Healthcare 1*, 1 (2004), 4–16.

[58] Domanov, I., and De Lathauwer, L. On the uniqueness of the canonical polyadic decomposition-part i: Basic results and uniqueness of one factor matrix. *SIAM Journal on Matrix Analysis and Applications 34*, 3 (2013), 855–875.

[59] Domanov, I., and De Lathauwer, L. On the uniqueness of the canonical polyadic decomposition-part ii: Overall uniqueness. *SIAM Journal on Matrix Analysis and Applications 34*, 3 (2013), 876–903.

[60] Donoho, D., and Tsaig, Y. Fast solution of ℓ_1 –norm minimization problems when the solution may be sparse. *Information Theory, IEEE Transactions on 54*, 11 (nov. 2008), 4789 –4812.

[61] Duann, J.-R., Jung, T.-P., Kuo, W.-J., Yeh, T.-C., Makeig, S., J Hsieh, e.-C., and Sejnowski, T. Single–trial variability in event–related bold signals. *NeuroImage 15*, 4 (2002), 823 – 835.

[62] Dupont, P., Van Paesschen, W., Palmini, A., Ambayi, R., Van Loon, J., Goffin, J., Weckhuysen, S., Sunaert, S., Thomas, B., Demaerel, P., Sciot, R., Becker, A. J., Vanbilloen, H., Mortelmans, L., and Van Laere, K. Ictal perfusion patterns associated with single mri–visible focal dysplastic lesions: Implications for the noninvasive delineation of the epileptogenic zone. *Epilepsia 47*, 9 (2006), 1550–1557.

[63] Engel, J. Surgery for seizures. *N Engl J Med 334*, 10 (1996), 647–53.

[64] FAHOUM, F., LOPES, R., PITTAU, F., DUBEAU, F., and GOTMAN, J. Widespread epileptic networks in focal epilepsies: Eeg-fmri study. *Epilepsia 53*, 9 (2012), 1618–1627.

[65] Farwell, L. A., and Donchin, E. Talking off the top of your head: toward a mental prosthesis utilizing event-related brain potentials. *Electroencephalography and clinical Neurophysiology 70*, 6 (1988), 510–523.

[66] Figueiredo, M. A. T. Adaptive sparseness for supervised learning. *Pattern Analysis and Machine Intelligence, IEEE Transactions on 25*, 9 (Sept 2003), 1150–1159.

[67] FISHER, R. A. The use of multiple measurements in taxonomic problems. *Annals of Eugenics 7*, 2 (1936), 179–188.

[68] Fisher, R. S., Boas, W. v. E., Blume, W., Elger, C., Genton, P., Lee, P., and Engel, J. Epileptic seizures and epilepsy: Definitions proposed by the international league against epilepsy (ilae) and the international bureau for epilepsy (ibe). *Epilepsia 46*, 4 (2005), 470–472.

[69] Fix, J. *Neuroanatomy.* Board review series. Lippincott Williams & Wilkins, 2008.

[70] Fraley, C., and Raftery, A. E. Model-based clustering, discriminant analysis, and density estimation. *Journal of the American Statistical Association 97*, 458 (2002), 611–631.

[71] Franaszczuk, P., and Blinowska, K. Linear model of brain electrical activity - eeg as a superposition of damped oscillatory modes. *Biological Cybernetics 53*, 1 (1985), 19–25.

[72] Friman, O., Borga, M., Lundberg, P., and Knutsson, H. Exploratory fmri analysis by autocorrelation maximization. *NeuroImage 16*, 2 (2002), 454–464.

[73] FRISTON, K., HOLMES, A., POLINE, J., GRASBY, P., WILLIAMS, S., FRACKOWIAK, R., AND TURNER, R. ANALYSIS OF FMRI TIME-SERIES REVISITED. *NEUROIMAGE 2*, 1 (MAR 1995), 45–53.

[74] GARDNER, A. B., KRIEGER, A. M., VACHTSEVANOS, G., AND LITT, B. One-class novelty detection for seizure analysis from intracranial eeg. *The Journal of Machine Learning Research 7* (2006), 1025–1044.

[75] GHAHRAMANI, Z. Unsupervised learning. In *Advanced Lectures on Machine Learning*, O. Bousquet, U. Luxburg, and G. R????tsch, Eds., vol. 3176 of *Lecture Notes in Computer Science*. Springer Berlin Heidelberg, 2004, pp. 72–112.

[76] GHOSH-DASTIDAR, S., ADELI, H., AND DADMEHR, N. Mixed-band wavelet-chaos-neural network methodology for epilepsy and epileptic seizure detection. *Biomedical Engineering, IEEE Transactions on 54*, 9 (2007), 1545–1551.

[77] GOLDBERGER, A. L., AMARAL, L. A. N., GLASS, L., HAUSDORFF, J. M., IVANOV, P. C., MARK, R. G., MIETUS, J. E., MOODY, G. B., PENG, C.-K., AND STANLEY, H. E. Physiobank, physiotoolkit, and physionet : Components of a new research resource for complex physiologic signals. *Circulation 101*, 23 (2000), 215–20.

[78] GOLUB, G., AND VAN LOAN, C. *Matrix Computations*. Matrix Computations. Johns Hopkins University Press, 2012.

[79] GOTMAN, J. Automatic recognition of epileptic seizures in the EEG. *Electroencephalography and Clinical Neurophysiology 54(5)* (1982), 530–40.

[80] GOTMAN, J., KOBAYASHI, E., BAGSHAW, A. P., BÉNAR, C.-G., AND DUBEAU, F. Combining eeg and fmri: A multimodal tool for epilepsy research. *Journal of Magnetic Resonance Imaging 23*, 6 (2006), 906–920.

[81] GRAMANN, K., GWIN, J. T., BIGDELY-SHAMLO, N., FERRIS, D. P., AND MAKEIG, S. Visual evoked responses during standing and walking. *Frontiers in human neuroscience 4* (2010), 202.

[82] GRANT, M., AND BOYD, S. CVX: Matlab software for disciplined convex programming, version 1.21. `http://cvxr.com/cvx`, Apr. 2011.

[83] GREENE, B., MARNANE, W., LIGHTBODY, G., REILLY, R., AND BOYLAN, G. Classifier models and architectures for eeg-based neonatal seizure detection. *Physiol Meas 29*, 10 (2008), 1157.

[84] Grouiller, F., Thornton, R. C., Groening, K., Spinelli, L., Duncan, J. S., Schaller, K., Siniatchkin, M., Lemieux, L., Seeck, M., Michel, C. M., and Vulliemoz, S. With or without spikes: localization of focal epileptic activity by simultaneous electroencephalography and functional magnetic resonance imaging. *Brain 134*, 10 (2011), 2867–2886.

[85] Grouiller, F., Vercueil, L., Krainik, A., Segebarth, C., Kahane, P., and David, O. A comparative study of different artefact removal algorithms for eeg signals acquired during functional mri. *NeuroImage 38*, 1 (2007), 124 – 137.

[86] Güler, I., and Übeyli, E. D. Adaptive neuro-fuzzy inference system for classification of eeg signals using wavelet coefficients. *Journal of neuroscience methods 148*, 2 (2005), 113–121.

[87] Gwin, J. T., Gramann, K., Makeig, S., and Ferris, D. P. Removal of movement artifact from high-density eeg recorded during walking and running. *Journal of neurophysiology 103*, 6 (2010), 3526–3534.

[88] Halder, S., Rea, M., Andreoni, R., Nijboer, F., Hammer, E., Kleih, S., Birbaumer, N., and Kübler, A. An auditory oddball brain–computer interface for binary choices. *Clinical Neurophysiology 121*, 4 (2010), 516–523.

[89] Hallez, H., De Vos, M., Vanrumste, B., P., V., Assecondi, S., Van Laere, K., Dupont, P., Van Paesschen, W., Van Huffel, S., and Lemahieu, I. Removing muscle and eye artifacts using blind source separation techniques in ictal eeg source imaging. *Clinical Neurophysiology 120*, 7 (2009), 1262 – 1272.

[90] Hayes-Roth, F. Rule-based systems. *Communications of the ACM 28*, 9 (1985), 921–932.

[91] He, X., Cai, D., and Niyogi, P. Tensor subspace analysis. In *Advances in Neural Information Processing Systems (NIPS)*, Y. Weiss, B. Schölkopf, and J. Platt, Eds. MIT Press, 2006, pp. 499–506.

[92] Hjorth, B. Eeg analysis based on time domain properties. *Electroencephalography and clinical neurophysiology 29*, 3 (1970), 306–310.

[93] Hopfengärtner, R., Kasper, B. S., Graf, W., Gollwitzer, S., Kreiselmeyer, G., Stefan, H., and Hamer, H. Automatic seizure detection in long-term scalp eeg using an adaptive thresholding technique: A validation study for clinical routine. *Clinical Neurophysiology* (2014).

[94] Hotelling, H. Relations between two sets of variates. *Biometrika 28*, 3/4 (1936), 321–377.

[95] http://askabiologist.asu.edu/whats-your-brain, january 2014.

[96] http://umm.edu/health/medical/reports/images/gray-and-white-matter-of-t january 2014.

[97] http://www.nlm.nih.gov/medlineplus/ency/imagepages/9549.htm, january 2014.

[98] http://biomedicalengineering.yolasite.com/neurons.php, january 2014.

[99] http://www.ica.luz.ve/~dfinol/NeuroCienciaCognitiva/What%20is%20Cogniti january 2014.

[100] http://www.bem.fi/book/13/13.htm, january 2014.

[101] Hunyadi, B., camps, D., Sorber, L., , Van Paesschen, W., De Vos, M., Van Huffel, S., and De Lathauwer, L. Block term decomposition for modelling epileptic seizures. Tech. rep., ESAT-Stadius, KU Leuven, 2014.

[102] Hunyadi, B., De Vos, M., Van Paesschen, W., and Van Huffel, S. A mimicking approach for human epileptic seizure detection. In *Proc. of the International Biosignal Processing Conference* (2010), pp. 1–4.

[103] Hunyadi, B., Mijović, B., Tousseyn, S., Dupont, P., Van Paesschen, W., Van Huffel, S., and De Vos, M. Ica component selection based on sparse activelet reconstruction for fmri analysis in refractory focal epilepsy. In *Pattern Recognition in NeuroImaging (PRNI), 2012 International Workshop on* (july 2012), pp. 1–4.

[104] Hunyadi, B., Signoretto, M., Debener, S., Van Huffel, S., and De Vos, M. Classification of structured eeg tensors using nuclear norm regularization: Improving p300 classification. In *Pattern Recognition in Neuroimaging (PRNI), 2013 International Workshop on* (2013), pp. 98–101.

[105] Hunyadi, B., Signoretto, M., Van Paesschen, W., Suykens, J. A. K., Van Huffel, S., and De Vos, M. Incorporating structural information from the multichannel eeg improves patient-specific seizure detection. *Clinical Neurophysiology 123*, 12 (2012), 2352 – 2361.

[106] Hunyadi, B., Tousseyn, S., Mijović, B., Dupont, P., Van Huffel, S., Van Paesschen, W., and De Vos, M. Ica extracts epileptic sources from fmri in eeg-negative patients: A retrospective validation study. *PLoS ONE 8*, 11 (11 2013), e78796.

[107] Hunyadi, B., Vos, M., Signoretto, M., Suykens, J., Paesschen, W., and Huffel, S. Automatic seizure detection incorporating structural information. In *Artificial Neural Networks and Machine Learning – ICANN 2011*, T. Honkela, W. Duch, M. Girolami, and S. Kaski, Eds., vol. 6791 of *Lecture Notes in Computer Science*. Springer Berlin Heidelberg, 2011, pp. 233–240.

[108] Hurley, N., and Rickard, S. Comparing measures of sparsity. In *Machine Learning for Signal Processing, 2008. MLSP 2008. IEEE Workshop on* (oct. 2008), pp. 55 –60.

[109] Hyvarinen, A. Fast and robust fixed-point algorithms for independent component analysis. *Neural Networks, IEEE Transactions on 10*, 3 (1999), 626–634.

[110] Jebara, T. *Discriminative, generative and imitative learning*. PhD thesis, Massachusetts Institute of Technology, 2001.

[111] Jirsch, J. D., Urrestarazu, E., LeVan, P., Olivier, A., Dubeau, F., and Gotman, J. High-frequency oscillations during human focal seizures. *Brain 129*, 6 (2006), 1593–1608.

[112] Jung, T.-P., Makeig, S., Humphries, C., Lee, T.-W., McKeown, M. J., Iragui, V., and Sejnowski, T. J. Removing electroencephalographic artifacts by blind source separation. *Psychophysiology 37*, 2 (2000), 163–178.

[113] Kannathal, N., Choo, M. L., Acharya, U. R., and Sadasivan, P. Entropies for detection of epilepsy in eeg. *Computer methods and programs in biomedicine 80*, 3 (2005), 187–194.

[114] Kelly, K., Shiau, D., Kern, R., Chien, J., Yang, M., Yandora, K., Valeriano, J., Halford, J., and Sackellares, J. Assessment of a scalp eeg-based automated seizure detection system. *Clinical Neurophysiology 121*, 11 (2010), 1832–1843.

[115] Khalidov, I., Fadili, J., Lazeyras, F., Van De Ville, D., and Unser, M. Activelets: Wavelets for sparse representation of hemodynamic responses. *Signal Processing 91*, 12 (2011), 2810 – 2821.

[116] Kiers, H. A. L., and der Kinderen, A. A fast method for choosing the numbers of components in tucker3 analysis. *British Journal of Mathematical and Statistical Psychology 56*, 1 (2003), 119–125.

[117] Kiviniemi, V., Kantola, J.-H., Jauhiainen, J., Hyvarinen, A., and Tervonen, O. Independent component analysis of nondeterministic fmri signal sources. *NeuroImage 19*, 2 (2003), 253 – 260.

[118] Kompany-Zareh, M., Akhlaghi, Y., and Bro, R. Tucker core consistency for validation of restricted tucker3 models. *Analytica Chimica Acta 723*, 0 (2012), 18 – 26.

[119] Koolen, N., Dereymaeker, A., Jansen, K., Vervisch, J., Matic, V., De Vos, M., Naulaers, G., and Van Huffel, S. Development of an interhemispheric symmetry measurement in the neonatal brain. In *ICPRAM* (2014).

[120] Kruskal, J. B. Three-way arrays: rank and uniqueness of trilinear decompositions, with application to arithmetic complexity and statistics. *Linear algebra and its applications 18*, 2 (1977), 95–138.

[121] Kuncheva, L. I. *Combining Pattern Classifiers: Methods and Algorithms*. Wiley. com, 2004.

[122] Kung, S. Y., Arun, K. S., and Bhaskar Rao, D. V. State-space and singular-value decomposition-based approximation methods for the harmonic retrieval problem. *Journal of the Optical Society of America 73*, 12 (Dec 1983), 1799–1811.

[123] Kurian, M., Spinelli, L., Delavelle, J., Chavez, V., Habre W., Meagher-Villemure, K., Roulet, E., Villeneuve, J., and Seeck, M. Multimodality imaging for focus localization in pediatric pharmacoresistant epilepsy. *Epileptic Disorder 9* (2007), 20–31.

[124] Kuzniecky, R. I., and Knowlton, R. C. Neuroimaging of epilepsy. *Seminars in neurology 22*, 3 (2002), 279–288.

[125] Labiner, D., Weinand, M., Brainerd, C., Ahern, G., Herring, A., and Melgar, M. Prognostic value of concordant seizure focus localizing data in the selection of temporal lobectomy candidates. *Neurological Reseach 24* (2002), 747–755.

[126] Lachenbruch, P. A., and Goldstein, M. Discriminant analysis. *Biometrics 35*, 1 (1979), pp. 69–85.

[127] Lee, H., Kim, Y.-D., Cichocki, A., and Choi, S. Nonnegative tensor factorization for continuous eeg classification. *International Journal of Neural Systems 17*, 04 (2007), 305–317. PMID: 17696294.

[128] Lee, S., Lee, S.-Y., Yun, C.-H., Lee, H.-Y., Lee, J.-S., and Lee, D.-S. Ictal spect in neocortical epilepsies: clinical usefulness and factors affecting the pattern of hyperperfusion. *Neuroradiology 48*, 9 (2006), 678–684.

[129] Leite, M., Leal, A., and Figueiredo, P. Transfer function between eeg and bold signals of epileptic activity. *Frontiers in Neurology 4*, 1 (2013), –.

[130] Lemm, S., Blankertz, B., Dickhaus, T., and Müller, K.-R. Introduction to machine learning for brain imaging. *NeuroImage 56*, 2 (2011), 387 – 399. Multivariate Decoding and Brain Reading.

[131] LeVan, P., Tyvaert, L., Moeller, F., and Gotman, J. Independent component analysis reveals dynamic ictal bold responses in eeg-fmri data from focal epilepsy patients. *NeuroImage 49*, 1 (2010), 366 – 378.

[132] Li, J., Zhang, L., and Zhao, Q. Pattern classification of visual evoked potentials based on parallel factor analysis. In *Advances in Cognitive Neurodynamics ICCN 2007*, R. Wang, E. Shen, and F. Gu, Eds. Springer Netherlands, 2008, pp. 571–575.

[133] Liu, A., Hahn, J., Heldt, G., and Coen, R. Detection of neonatal seizures through computerized eeg analysis. *Electroencephalography and clinical neurophysiology 82*, 1 (1992), 30–37.

[134] Liu, Y., De Vos, M., Gligorijevic, I., Matic, V., Li, Y., and Huffel, S. Multi-structural signal recovery for biomedical compressive sensing.

[135] Löfhede, J., Thordstein, M., Löfgren, N., Flisberg, A., Rosa-Zurera, M., Kjellmer, I., and Lindecrantz, K. Automatic classification of background eeg activity in healthy and sick neonates. *Journal of neural engineering 7*, 1 (2010), 016007.

[136] Logothetis, N. K., and Wandell, B. A. Interpreting the bold signal. *Annual Review of Physiology 66* (2004), 735–769.

[137] Lopes, R., Lina, J., Fahoum, F., and Gotman, J. Detection of epileptic activity in fmri without recording the eeg. *NeuroImage 60*, 3 (2012), 1867 – 1879.

[138] Lotte, F., Congedo, M., L?cuyer, A., Lamarche, F., and Arnaldi, B. A review of classification algorithms for eeg-based brain-computer interfaces. *Journal of Neural Engineering 4* (2007), 1–13.

[139] Lukas, L., Devos, A., Suykens, J. A. K., Vanhamme, L., Van Huffel, S., Tate, A., Majós, C., and Arús, C. The Use of LS-SVM in the Classification of Brain Tumors Based on Magnetic Resonance Spectroscopy Signals. In *Proceedings of the European Symposium on Artificial Neural Networks, (ESANN)* (Bruges, 2002).

[140] Marks, D. A., Katz, A., Booke, J., Spencer, D. D., and Spencer, S. S. Comparison and correlation of surface and sphenoidal electrodes with simultaneous intracranial recording: an interictal study. *Electroencephalography and Clinical Neurophysiology 82*, 1 (1992), 23–29.

[141] McKeown, M., Makeig, S., Brown, G., Jung, T., Kindermann, S., Kindermann, R., Bell, A., and Sejnowski, T. Analysis of fmri data by blind separation into independent spatial components. *Human Brain Mapping 6* (1998), 160–188.

[142] Meier, R., Dittrich, H., Schulze-Bonhage, A., and Aertsen, A. Detecting epileptic seizures in long-term human eeg: A new approach to automatic online and real-time detection and classification of polymorphic seizure patterns. *Journal of Clinical Neurophysiology 25*, 3 (2008), 119–131.

[143] Mijović, B., Vanderperren, K., Novitskiy, N., Vanrumste, B., Stiers, P., Van den Bergh, B., Lagae, L., Sunaert, S., Wagemans, J., Van Huffel, S., and De Vos, M. The "why" and "how" of jointica: Results from a visual detection task. *NeuroImage 60*, 2 (2012), 1171 – 1185.

[144] Minasyan, G. R., Chatten, J. B., Chatten, M. J., and Harner, R. N. Patient-specific early seizure detection from scalp electroencephalogram. *J of Clin Neurophysiol 27*, 3 (2010), 163–78.

[145] Mitchell, T. M. *Machine Learning,*. McGraw-Hill Science/Engineering/Math, 1997.

[146] Moeller, F., LeVan, P., and Gotman, J. Independent component analysis (ica) of generalized spike wave discharges in fmri: Comparison with general linear model-based eeg-fmri. *Human Brain Mapping 32*, 2 (2011), 209–217.

[147] Moore, G. E., et al. Cramming more components onto integrated circuits, 1965.

[148] Moosmann, M., Schönfelder, V. H., Specht, K., Scheeringa, R., Nordby, H., and Hugdahl, K. Realignment parameter–informed artefact correction for simultaneous eeg–fmri recordings. *NeuroImage 45*, 4 (2009), 1144 – 1150.

[149] Morgan, V., Li, Y., Abou-Khalil, B., and Gore, J. Development of 2dtca for the detection of irregular, transient bold activity. *Human Brain Mapping 29*, 1 (2008), 57–69.

[150] Morgan, V., Price, R., Arain, A., Modur, P., and Abou-Khalil, B. Resting functional mri with temporal clustering analysis for localization of epileptic activity without eeg. *NeuroImage 21*, 1 (2004), 473 – 481.

[151] Mørup, M., and Hansen, L. Automatic relevance determination for multi-way models. *Journal of Chemometrics 23*, 7-8 (2009), 352–363.

[152] Mørup, M., Hansen, L., Hermann, C., Parnas, J., and Arnfred, S. M. Parallel Factor Analysis as an exploratory tool for wavelet transformed event-related EEG. *NeuroImage 29*, 3 (2006), 938–947.

[153] Nam, H., Yim, T.-G., Han, S. K., Oh, J.-B., and Lee, S. K. Independent component analysis of ictal eeg in medial temporal lobe epilepsy. *Epilepsia 43*, 2 (2002), 160–164.

[154] Nandan, M., Talathi, S. S., Myers, S., Ditto, W. L., Khargonekar, P. P., and Carney, P. R. Support vector machines for seizure detection in an animal model of chronic epilepsy. *J of Neural Eng 7*, 3 (2010), 036001.

[155] Negnevitsky, M. *Artificial Intelligence: A Guide to Intelligent Systems*. Addison-Wesley, 2005.

[156] Newey, C. R., Wong, C., Irene Wang, Z., Chen, X., Wu, G., and Alexopoulos, A. V. Optimizing spect siscom analysis to localize seizure-onset zone by using varying z scores. *Epilepsia 54*, 5 (2013), 793–800.

[157] Niedermeyer, E., and da Silva, F. *Electroencephalography: Basic Principles, Clinical Applications, and Related Fields*. LWW Doody's all reviewed collection. Lippincott Williams & Wilkins, 2005.

[158] Nion, D., and Sidiropoulos, N. D. Adaptive algorithms to track the parafac decomposition of a third-order tensor. *Signal Processing, IEEE Transactions on 57*, 6 (2009), 2299–2310.

[159] Oostendorp, T., Delbeke, J., and Stegeman, D. F. The conductivity of the human skull: results of in vivo and in vitro measurements. *Biomedical Engineering, IEEE Transactions on 47*, 11 (2000), 1487–1492.

[160] Osorio, I., Frei, M. G., and Wilkinson, S. B. Real-time automated detection and quantitative analysis of seizures and short-term prediction of clinical onset. *Epilepsia 39*, 6 (1998), 615–627.

[161] Pan, S. J., and Quiang, Y. A survey on transfer learning. *Knowledge and Data Engineering, IEEE Transactions on 22*, 10 (Oct 2010), 1345–1359.

[162] Panayiotopoulos, C. P. *The Epilepsies: Seizures, Syndromes and Management*. Oxfordshire (UK): Bladon Medical Publishing, 2005.

[163] Pfurtscheller, G., and Neuper, C. Motor imagery and direct brain-computer communication. *Proceedings of the IEEE 89*, 7 (2001), 1123–1134.

[164] Phan, A., and Cichocki, A. Tensor decompositions for feature extraction and classification of high dimensional datasets. *Nonlinear theory and its applications, IEICE 1* (2010), 37–68.

[165] Pires, G., Nunes, U., and Castelo-Branco, M. Statistical spatial filtering for a p300-based bci: Tests in able-bodied, and patients with cerebral palsy and amyotrophic lateral sclerosis. *Journal of Neuroscience Methods 195*, 2 (2011), 270 – 281.

[166] Platt, J. C. Probabilistic outputs for support vector machines and comparisons to regularized likelihood methods. In *Advances in large margin classifiers* (1999), MIT Press, pp. 61–74.

[167] Polat, K., and Güneş, S. Classification of epileptiform eeg using a hybrid system based on decision tree classifier and fast fourier transform. *Applied Mathematics and Computation 187*, 2 (2007), 1017–1026.

[168] Polychronaki, G., Ktonas, P., Gatzonis, S., Siatouni, A., Asvestas, P., Tsekou, H., Sakas, D., and Nikita, K. Comparison of fractal dimension estimation algorithms for epileptic seizure onset detection. *J of Neural Eng 7*, 4 (2010), 046007.

[169] Qu, H., and Gotman, J. A patient-specific algorithm for the detection of seizure onset in long-term eeg monitoring: possible use as a warning device. *IEEE Trans Biomed Eng 44*, 2 (1997), 115 –122.

[170] Ramoser, H., Muller-Gerking, J., and Pfurtscheller, G. Optimal spatial filtering of single trial eeg during imagined hand movement. *Rehabilitation Engineering, IEEE Transactions on 8*, 4 (2000), 441–446.

[171] Recht, B., Fazel, M., and Parrilo, P. Guaranteed minimum-rank solutions of linear matrix equations via nuclear norm minimization. *SIAM Review 52 (3)* (2007), 471–501.

[172] Rissanen, J. A universal prior for integers and estimation by minimum description length. *Annals of Statistics 11* (1983), 416–431.

[173] Rodionov, R., De Martino, F., Laufs, H., Carmichael, D., Formisano, E., Walker, M., Duncan, J., and Lemieux, L. Independent component analysis of interictal fmri in focal epilepsy: Comparison with general linear model–based eeg–correlated fmri. *NeuroImage 38*, 3 (2007), 488 – 500.

[174] Romera-Paredes, B., Aung, H., Bianchi-Berthouze, N., and Pontil, M. Multilinear multitask learning. In *Proceedings of The 30th International Conference on Machine Learning* (2013), pp. 1444–1452.

[175] Rosenow, F., and L?ers, H. Presurgical evaluation of epilepsy. *Brain 124*, 9 (2001), 1683–1700.

[176] Saab, M., and Gotman, J. A system to detect the onset of epileptic seizures in scalp eeg. *Clin Neurophysiol 116*, 2 (2005), 427 – 442.

[177] Salek-Haddadi, A., Diehl, B., Hamandi, K., Merschhemke, M., Liston, A., Friston, K., Duncan, J., Fish, D., and Lemieux, L. Hemodynamic correlates of epileptiform discharges: An eeg–fmri study of 63 patients with focal epilepsy. *Brain Research 1088*, 1 (2006), 148 – 166.

[178] Salimi-Khorshidi, G., Douaud, G., Beckmann, C. F., Glasser, M. F., Griffanti, L., and Smith, S. M. Automatic denoising of functional mri data: Combining independent component analysis and hierarchical fusion of classifiers. *NeuroImage* (2014).

[179] Salu, Y., Cohen, L., Rose, D., Sxato, S., Kufta, C., and Hallett, M. An improved method for localizing electric brain dipoles. *Biomedical Engineering, IEEE Transactions on 37*, 7 (1990), 699–705.

[180] Samek, W., Meinecke, F. C., and Müller, K.-R. Transferring subspaces between subjects in brain-computer interfacing. *IEEE Transactions on Biomedical Engineering 60*, 8 (2013), 2289–2298.

[181] Schalk, G., McFarland, D. J., Hinterberger, T., Birbaumer, N., and Wolpaw, J. R. Bci2000: a general-purpose brain-computer interface (bci) system. *Biomedical Engineering, IEEE Transactions on 51*, 6 (2004), 1034–1043.

[182] Schiff, S. J., Colella, D., Jacyna, G. M., Hughes, E., Creekmore, J. W., Marshall, A., Bozek-Kuzmicki, M., Benke, G., Gaillard, W. D., Conry, J., and Weinstein, S. R. Brain chirps: spectrographic signatures of epileptic seizures. *Clinical Neurophysiology 111*, 6 (2000), 953 – 958.

[183] Schlögl, A., Vidaurre, C., and Müller, K.-R. Adaptive methods in bci research-an introductory tutorial. In *Brain-Computer Interfaces*. Springer, 2010, pp. 331–355.

[184] Sheorajpanday, R. V., Nagels, G., Weeren, A. J., van Putten, M. J., and Deyn, P. P. D. Reproducibility and clinical relevance of quantitative EEG parameters in cerebral ischemia: A basic approach. *Clinical Neurophysiology 120*, 5 (2009), 845 – 855.

[185] Shlens, J. A tutorial on principal component analysis. *Systems Neurobiology Laboratory, University of California at San Diego* (2005).

[186] Shoeb, A., and Guttag, J. Application of machine learning to epileptic seizure detection. In *Proceedings of the 27th International Conference on Machine Learning (ICML)* (Haifa, Israel, June 2010), J. Fürnkranz and T. Joachims, Eds., Omnipress, pp. 975–982.

[187] Signoretto, M. *Kernels and Tensors for Structured Data Modelling*. PhD thesis, Katholieke Universiteit Leuven, 2011.

[188] Signoretto, M., De Lathauwer, L., and Suykens, J. A. K. A kernel-based framework to tensorial data analysis. *Neural Networks 24*, 8 (2011), 861 – 874.

[189] Signoretto, M., Tran Dinh, Q., De Lathauwer, L., and Suykens, J. Learning with tensors : a framework based on convex optimization and spectral regularization. *Machine Learning accepted* (2013).

[190] Smyser, C. D., Inder, T. E., Shimony, J. S., Hill, J. E., Degnan, A. J., Snyder, A. Z., and Neil, J. J. Longitudinal analysis of neural network development in preterm infants. *Cerebral cortex 20*, 12 (2010), 2852–2862.

[191] So, E. Integration of eeg, mri, and spect in localizing the seizure focus for epilepsy surgery. *Epilepsia 43* (2000), 219–227.

[192] Sorber, L., Van Barel, M., and De Lathauwer, L. Tensorlab v1.0, Available online, URL: http://esat.kuleuven.be/sista/tensorlab/. Tech. rep., February 2013.

[193] Spencer, S., and Huh, L. Outcomes of epilepsy surgery in adults and children. *The Lancet Neurology 7*, 6 (2008), 525 – 537.

[194] Spencer, S. S. The relative contributions of mri, spect, and pet imaging in epilepsy. *Epilepsia 35* (1994), S72–S89.

[195] Spencer, S. S., Williamson, P. D., Bridgers, S. L., Mattson, R. H., Cicchetti, D. V., and Spencer, D. D. Reliability and accuracy of localization by scalp ictal eeg. *Neurology 35*, 11 (1985), 1567–1567.

[196] Stankovic, J., Cao, Q., Doan, T., Fang, L., He, Z., Kiran, R., Lin, S., Son, S., Stoleru, R., and Wood, A. Wireless sensor networks for in-home healthcare: Potential and challenges. In *High confidence medical device software and systems (HCMDSS) workshop* (2005), pp. 2–3.

[197] Stern, J., and Engel, J. *An Atlas of EEG Patterns*. Lippincott Williams & Wilkins, 2005.

[198] Subasi, A. Eeg signal classification using wavelet feature extraction and a mixture of expert model. *Expert Systems with Applications 32*, 4 (2007), 1084–1093.

[199] Subasi, A., and Gursoy, M. I. Eeg signal classification using pca, ica, lda and support vector machines. *Expert Systems with Applications 37*, 12 (2010), 8659 – 8666.

[200] Suykens, J. A. K., Van Gestel, T., De Brabanter, J., De Moor, B., and Vandewalle, J. *Least Squares Support Vector Machines*. World Scientific, Singapore, 2002.

[201] Suykens, J. A. K., and Vandewalle, J. Least squares support vector machine classifiers. *Neural Process Lett 9*, 3 (1999), 293–300.

[202] Tao, D., Li, X., Wu, X., Hu, W., and Maybank, S. J. Supervised tensor learning. *Knowl Inf Syst 13* (2007), 1–42.

[203] Tao, J. X., Ray, A., Hawes-Ebersole, S., and Ebersole, J. S. Intracranial eeg substrates of scalp eeg interictal spikes. *Epilepsia 46*, 5 (2005), 669–676.

[204] Temko, A., Thomas, E., Marnane, W., Lightbody, G., and Boylan, G. Eeg-based neonatal seizure detection with support vector machines. *Clin Neurophysiol 122*, 3 (2011), 464–73.

[205] Thomas, E., Temko, A., Lightbody, G., Marnane, W., and Boylan, G. B. A comparison of generative and discriminative approaches in automated neonatal seizure detection. In *Intelligent Signal Processing, 2009. WISP 2009. IEEE International Symposium on* (2009), pp. 181–186.

[206] Thornton, R., Rodionov, R., Laufs, H., Vulliemoz, S., Vaudano, A., Carmichael, D., Cannadathu, S., Guye, M., McEvoy, A., Lhatoo, S., Bartolomei, F., Chauvel, P., Diehl, B., De Martino, F., Elwes, R., Walker, M., Duncan, J., and Lemieux, L. Imaging haemodynamic changes related to seizures: Comparison of eeg–based general linear model, independent component analysis of fmri and intracranial eeg. *NeuroImage 53*, 1 (2010), 196 – 205.

[207] Tibshirani, R., Walther, G., and Hastie, T. Estimating the number of clusters in a data set via the gap statistic. *Journal of the Royal Statistical Society: Series B (Statistical Methodology) 63*, 2 (2001), 411–423.

[208] Timmerman, M. E., and Kiers, H. A. L. Three-mode principal components analysis: Choosing the numbers of components and sensitivity to local optima. *British Journal of Mathematical and Statistical Psychology 53*, 1 (2000), 1–16.

[209] Tito, M., Cabrerizo, M., Ayala, M., Jayakar, P., and Adjouadi, M. Seizure detection: An assessment of time- and frequency-based features in a unified two-dimensional decisional space using nonlinear decision functions. *Journal of Clinical Neurophysiology 26*, 6 (2009), 381–391.

[210] Tomioka, R., and Aihara, K. Classifying matrices with a spectral regularization. In *In proceeding of: Machine Learning, Proceedings of the Twenty-Fourth International Conference (ICML 2007)* (2007), pp. 895–902.

[211] Tomioka, R., Suzuki, T., Sugiyama, M., and Kashima, H. A fast augmented lagrangian algorithm for learning low-rank matrices. *International conference on Machine Learning (ICML)* (2010), 1–8.

[212] Tousseyn, S., Dupont, P., Goffin, K., Sunaert, S., and Van Paesschen, W. Diagnostic performance of a new semi-automatic template-based analysis method for interictal eeg-fmri. *in preparation*.

[213] Tousseyn, S., Dupont, P., Goffin, K., Sunaert, S., and Van Paesschen, W. Sensitivity and specificity of interictal eeg-fmri for detecting the ictal onset zone at different statistical thresholds. *submitted*.

[214] Traub, R., Jefferys, J., and Whittington, M. *Fast Oscillations in Cortical Circuits*. A Bradford book. BRADFORD BOOK, 1999.

[215] Tzallas, A. T., Tsipouras, M. G., Tsalikakis, D. G., Karvounis, E. C., Astrakas, L., Konitsiotis, S., and Tzaphlidou, M. Automated epileptic seizure detection methods: a review study. *Epilepsy-histological, electroencephalographic and psychological aspects, edited by D. Stevanovic* (2012), 75–98.

[216] Urrestarazu, E., Iriarte, J., Alegre, M., Valencia, M., Viteri, C., and Artieda, J. Independent component analysis removing artifacts in ictal recordings. *Epilepsia 45*, 9 (2004), 1071–1078.

[217] van de Ven, V., Formisano, E., Prvulovic, D., Roeder, C., and Linden, D. Functional connectivity as revealed by spatial independent component analysis of fMRI measurements during rest. *Human Brain Mapping 22*, 3 (2004), 165–178.

[218] Van Paesschen, W. Ictal spect. *Epilepsia 45*, s4 (2004), 35–40.

[219] Van Paesschen, W., Dupont, P., Sunaert, S., Goffin, K., and Van Laere, K. The use of spect and pet in routine clinical practice in epilepsy. *Current Opinion in Neurology 20*, 2 (2007), 194–202.

[220] van Putten, M. J. Nearest neighbor phase synchronization as a measure to detect seizure activity from scalp eeg recordings. *Journal of clinical neurophysiology 20*, 5 (2003), 320–325.

[221] van Putten, M. J., Peters, J. M., Mulder, S. M., A.M., d. J., Bruijninckx, C. M., and Tavy, D. L. A brain symmetry index (BSI) for online EEG monitoring in carotid endarterectomy. *Clinical Neurophysiology 115*, 5 (2004), 1189 – 1194.

[222] Vanderperren, K., De Vos, M., Ramautar, J., Novitskiy, N., Mennes, M., Assecondi, S., Vanrumste, B., Stiers, P., Van den Bergh, B., Wagemans, J., Lagae, L., Sunaert, S., and Van Huffel, S. Removal of bcg artifacts from eeg recordings inside the mr scanner: A comparison of methodological and validation–related aspects. *NeuroImage 50*, 3 (2010), 920 – 934.

[223] Vanderperren, K., Mijović, B., Novitskiy, N., Vanrumste, B., Stiers, P., Van den Bergh, B., Lagae, L., Sunaert, S.,

Wagemans, J., Van Huffel, S., and De Vos, M. Single trial erp reading based on parallel factor analysis. *Psychophysiology 50(1)* (2013), 97–110.

[224] Vanhatalo, S., and Kaila, K. Development of neonatal eeg activity: from phenomenology to physiology. In *Seminars in Fetal and Neonatal Medicine* (2006), vol. 11, Elsevier, pp. 471–478.

[225] Vapnik, V. *The Nature of Statistical Learning Theory*. Information Science and Statistics. Springer, 2000.

[226] Varsavsky, A., Mareels, I., and Cook, M. *Epileptic Seizures and the EEG: Measurement, Model, Detection and Prediction*. CRC Press, 2011.

[227] Vergult, A., De Clercq, W., Palmini, A., Vanrumste, B., Dupont, P., Van Huffel, S., and Van Paesschen, W. Improving the interpretation of ictal scalp eeg: Bss - cca algorithm for muscle artifact removal. *Epilepsia 48*, 5 (2007), 950–958.

[228] Westwood, J. *Medicine Meets Virtual Reality 02/10: Digital Upgrades, Applying Moore's Law to Health*. Studies in health technology and informatics. IOS Press, 2002.

[229] Wolpaw, J. R., Birbaumer, N., Heetderks, W. J., McFarland, D. J., Peckham, P. H., Schalk, G., Donchin, E., Quatrano, L. A., Robinson, C. J., Vaughan, T. M., et al. Brain-computer interface technology: a review of the first international meeting. *IEEE transactions on rehabilitation engineering 8*, 2 (2000), 164–173.

[230] Wu, S., Chaudhry, B., Wang, J., Maglione, M., Mojica, W., Roth, E., Morton, S. C., and Shekelle, P. G. Systematic review: impact of health information technology on quality, efficiency, and costs of medical care. *Annals of internal medicine 144*, 10 (2006), 742–752.

[231] Wyllie, E., Cascino, G., and Gidal, B. *Wyllie's Treatment of Epilepsy: Principles and Practice*. Wyllie, Treatment of Epilepsy. Lippincott Williams & Wilkins, 2010.

[232] Xavier de Souza, S., Suykens, J. A. K., Vandewalle, J., and Bollé, D. Coupled simulated annealing. *IEEE T Syst Man Cyb 40*, 2 (2010), 320–335.

[233] Zandi, A. S., Javidan, M., Dumont, G. A., and Tafreshi, R. Automated real-time epileptic seizure detection in scalp eeg recordings using an algorithm based on wavelet packet transform. *IEEE Trans Biomed Eng 57*, 7 (2010), 1639 –51.

[234] Zijlmans, M., Huiskamp, G., Hersevoort, M., Seppenwoolde, J.-H., van Huffelen, A. C., and Leijten, F. S. S. Eeg–fmri in the preoperative work–up for epilepsy surgery. *Brain 130*, 9 (2007), 2343–2353.

Curriculum

Borbála Hunyadi was born in Budapest, Hungary on February 10, 1986.

She received a M.Sc. degree in computer and electrical engineering from the Pázmány Péter Catholic University, Hungary in July 2009. During her studies she spent two semesters at KU Leuven with the Erasmus Programme. The research project she conducted within the Biomed research group during this period became part of her master thesis, entitled “Electrophysiological signal processing in the study of neural oscillations".

In October 2009 she joined STADIUS, Department of Electical Engineering (ESAT), KU Leuven as a PhD student under the supervision of Prof. dr. ir. Sabine Van Huffel, Prof. dr. Wim Van Paesschen and Prof. dr. ir. Maarten de Vos. Since October 2013 she worked on the IWT TBM EEG-fMRI project in close collaboration with the Laboratory for Epilepsy Research, KU Leuven. Her current research interests include developing signal processing and machine learning solutions for the analysis of EEG and fMRI signals.

She has been engaged in science communication, contributing to the development of several demonstrations and pre-university outreach workshops. Besides, she has been an active member of the IEEE Student Branch Leuven and chaired the Women in Engineering Affinity Group.

Publication list

Papers in international journals

1. Hunyadi, B., Tousseyn, S., Mijovic, B., Dupont, P., Van Huffel, S., Van Paesschen, W., De Vos, M. (2013). ICA extracts epileptic sources from fMRI in EEG-negative patients : a retrospective validation study. PLoS One (accepted).

2. Hunyadi, B., Signoretto, M., Van Huffel, S., Suykens, J., De Vos, M. (2012). Incorporating structural information from the mulitchannel EEG improves patient-specific seizure detection. Clinical Neurophysiology, 123 (12), 2352-2361.

Papers submitted to international journals

1. Hunyadi B., Camps D., Sorber L., Van Paesschen W., De Vos M., Van Huffel S., De Lathauwer L. Block term decomposition for modelling epileptic seizures. EURASIP Journal on Advances in Signal Processing, submitted 19 December 2013

2. Caicedo A., Varon C., Hunyadi B., Papademetriou M., Tachtsidis I., and Van Huffel S. Signal Decomposition Based on Wavelet Regression and Oblique Subspace Projections: Theoretical Framework, Algorithms and Applications in Biomedical Signal Processing. IEEE Transactions on Biomedical Engineering, submitted 23 April 2014

Papers in proceedings of international conferences

1. De Meester, J., Batselier, K., Koolen, N., Hunyadi, B., Decuyper, J., Vanden Bosch, E., Vandewalle, J., Dehaene, W. (2013). The mathematics

in your ears. The role of math in integrated STEM via the modeling of hearing aids. Proc. of the 41th SEFI Conference. SEFI. Leuven, Belgium, Sep. 2013 (pp. 1-8).

2. De Vos, M., Zink, R., Hunyadi, B., Mijovic, B., Van Huffel, S., Debener, S. (2013). The quest for single trial correlations in multimodal EEG-fMRI data. Proc. of the 35th Annual International Conference of the IEEE Engineering in Medicine and Biology Society. IEEE EMBC 2013. Osaka, Japan, Jul. 2013 (pp. 6027-6030).

3. Geth, F., Verveckken, J., Leemput, N., Van Roy, J., Beerten, J., Tielens, P., De Smedt, V., Iacovella, S., Hunyadi, B., Koolen, N., De Clercq, H., Gielen, G., Puers, B., Van Huffel, S., Belmans, R., Deconinck, G., Dehaene, W., Driesen, J. (2013). Development of an Open-Source Smart Energy House for K-12 Education. Proc. IEEE Power and Energy Society Annual Meeting. IEEE PES General Meeting 2013. Vancouver, Canada, 21-25 July 2013 (pp. 1-5).

4. Verveckken, J., Geth, F., Hunyadi, B., Beerten, J., Leemput, N., Van Roy, J., Tielens, P., De Smedt, V., Iacovella, S., Koolen, N., De Clercq, H., Driesen, J., Gielen, G., Puers, B., Vandewalle, J., Van Huffel, S., Belmans, R., Deconinck, G., Dehaene, W. (2013). Developing Engineering-oriented Educational Workshops Within a Student Branch. Proc. IEEE EUROCON 2013. Zagreb, Croatia, 1-4 July 2013 (pp. 933-939).

5. Mijovic, B., Machilsen, B., Hunyadi, B., De Vos, M., Wagemans, J., Van Huffel, S. (2013). Comparison of correlation analysis and JointICA for simultaneous EEG-fMRI recordings on contour integration taks. Proc. of the 35th Annual International Conference of the IEEE Engineering in Medicine and Biology Society. IEEE EMBS 2013. Osaka, Japan, Jul.2013 (pp. 6019-6022).

6. Hunyadi, B., Signoretto, M., Debener, S., Van Huffel, S., De Vos, M. (2013). Classification of structured EEG tensors using nuclear norm regularization : improving P300 classification. Proc. of the international workshop on pattern recognition in neuroimaging. PRNI 2013. Philadelphia, US, Jun. 2013 (pp. 1-4).

7. Hunyadi, B., Mijovic, B., Tousseyn, S., Dupont, P., Van Paesschen, W., Van Huffel, S., De Vos, M. (2012). ICA component selection based on sparse activelet reconstruction for fMRI analysis in refractory focal epilepsy. Proc. of the Pattern Recognition in Neuroimage conference. PRNI 2012. London, UK, Jul. 2012 (pp. 21-24).

8. Hunyadi, B., De Vos, M., Signoretto, M., Suykens, J., Van Paesschen, W., Van Huffel, S. (2011). Automatic seizure detection incorporating structural information. Proc.of the 21st International Conference on Artificial Neural Networks (LNCS 6791): Vol. 6791. ICANN 2011. Espoo, Finalnd, Jun. 2011 (pp. 233-240).

9. Hunyadi, B., De Vos, M., Van Paesschen, W., Van Huffel, S. (2010). A mimicking approach for human epileptic seizure detection. Proc. of the International Biosignal Processing Conference. International Biosignal Processing Conference. Berlin, Germany, Jul. 2010 (pp. 1-4).

10. Vanderperren, K., Hunyadi, B., De Vos, M., Mennes, M., Wouters, H., Vanrumste, B., Stiers, P., Lagae, L., Van Huffel, S. (2008). Reduction of alpha distortion in event related potentials. Proc. of the 4th European Medical and Biomedical Engineering congress (eMBEC). 4th European Medical and Biomedical Engineering congress (eMBEC). Antwerp, Belgium, Nov. 2008 (pp. 1298-1301).

Abstracts in proceedings of international conferences

1. Hunyadi, B., Tousseyn, S., De Vos, M., Van Huffel, S., Van Paesschen, W. (2012). Localizing the ictal onset zone with data-driven FMRI analysis. Proc. of the American Epilepsy Society Meeting 2012. AES 2012. San Diego, USA, Dec. 2012.

2. Hunyadi, B., De Vos, M., Signoretto, M., Suykens, J., Van Huffel, S., Van Paesschen, W. (2011). Patient-specific seizure detection with limited training period. Proc. of the American Epilepsy Society Meeting 2011. AES 2011. Baltimore, ML, Dec. 2011.

3. Hunyadi, B., De Vos, M., Van Huffel, S., Van Paesschen, W. (2010). Automatic seizure detection algorithm based on the human visual interpretation process of scalp EEG. Proc. of the American Epilepsy Society Meeting 2010. AES 2010. San Antonio, Texas, Dec. 2010.

FACULTY OF ENGINEERING SCIENCE
DEPARTMENT OF ELECTRICAL ENGINEERING
STADIUS CENTER FOR DYNAMICAL SYSTEMS, SIGNAL PROCESSING AND DATA ANALYTICS
Kasteelpark Arenberg 10 box 2446
B-3001 Heverlee
borbala.hunyadi@esat.kuleuven.be